ASSESSMENT OF SEISMIC BEHAVIOUR OF LARGE CONCRETE DAMS BY MEANS OF GEOMATICS TECHNIQUES AND FINITE ELEMENT MODELING

Dissertation
submitted to and approved by the

Department of Architecture, Civil Engineering and Environmental Sciences
University of Braunschweig – Institute of Technology

and the

Department of Civil and Environmental Engineering
University of Florence

in candidacy for the degree of a
Doktor-Ingenieurin (Dr.-Ing.) /
Dottore di Ricerca in Civil and Environmental Engineering

by
Giulia Buffi
born 22/10/1989
from Rome, Italy

Submitted on	20 February, 2018
Oral examination on	07/05/2018
Professorial advisors	Prof. Laura De Lorenzis Prof. Piergiorgio Manciola

2018

Abstract

Department of Civil and Environmental Engineering
Doctor of Philosophy
Assessment of Seismic Behaviour of Large Concrete Dams by means of Geomatics Techniques and Finite Element Modelling

By Giulia BUFFI

The safety and efficient maintenance of dams are primary aspects in the management of such strategic works. The need to combine, ever more effectively, the security with the containment of maintenance costs directly linked to the service life of the structure, requires innovative approaches beside traditional methods. In this respect, the limited accessibility of large dams does not facilitate the use of traditional survey techniques, although a reliable terrestrial survey is still necessary, the use of Unmanned Aerial Vehicles (UAV) is well suited for this purpose. The aim of the present study is to provide a reconstruction procedure of a high detail FE model of a dam starting from an integrated UAV survey useful for a predictive and proactive maintenance of the dam system. In particular, the "Structure from Motion" (SfM) technique can be used for the reconstruction of 3D objects from 2D images. Therefore, after an integration of the UAV dense point cloud with pre-existing data sets such as design geometry, Digital Elevation Model (DEM) of the area and bathymetry of the lake, a three-dimensional solid reconstruction of the whole dam system is possible. The high detail level of the UAV survey makes possible the geometric reconstruction of important elements of the structure such as spillway, vertical joints and *pulvino* foundation joint and of ancillary works such as stilling basin and weight blocks. In order to study the influence of joint modelling on the dynamic behaviour of the structure, three models have been analyzed: monolithic structure, surface-to-surface joint structure and solid element joint structure. All simulations take into account the structure-foundation interaction by means of a rock mass solid and the fluid-structure interaction by means of acoustic elements. Modal analyses are therefore performed in order to obtain the dynamic properties of the models and to identify the representation which fits better with the real dynamic records (e.g. vibrodyne test, ambient vibrations). Subsequently, linear elastic dynamic analyses are performed to calibrate the damping coefficients of rock mass and structure. Finally, non-linearity is introduced in the joint elements performing non-linear dynamic damage analyses under severe earthquakes and, varying the water level, the damage distribution is investigated. The inclusion of vertical construction joints into finite element models of dams allows us to verify the behaviour of such real discontinuities under MCE – Maximum Credible Earthquake – events and therefore to verify the seismic vulnerability assessment of the whole structure.

Acknowledgement

The present PhD research has been funded by Romagna Acque – Società delle Fonti S.p.A. which is greatly acknowledged. I wish to acknowledge Prof. Dr. Eng. Piergiorgio Manciola and Dr. Eng. Andrea Gambi (CEO Romagna Acque S.p.A.) for the trust they have placed in me. I thanks my other Italian tutors, Prof. Dr. Eng. Marco Mezzi and Prof. Dr. Eng. Vittorio Gusella, who supported me in the DICA – Department of Civil and Environmental Engineering – of the University of Perugia (Italy). A special thanks to Prof. Dr. Eng. Claudio Tamagnini (DICA – University of Perugia). I express my gratitude to Dr. Eng. Nicola Cavalagli (DICA – University of Perugia) and to Dr. Eng. Fabrizio Comodini (DICA – University of Perugia). I wish to thank my German tutors, Prof. Dr. Eng. Laura De Lorenzis (Head of the Institute of Applied Mechanics) and Prof. Dr. Eng. Wolfgang Niemeier (Emeritus Professor in Institute for Geodesy and Photogrammetry) of the Technische Universität Braunschweig, Germany.

I acknowledge Dr. Tonino Bernabè (President of Romagna Acque S.p.A.), Dr. Eng. Franco Farina (Engineer of Romagna Acque S.p.A.) and Dr. Eng. Giuseppe Montanari (Engineer of Romagna Acque S.p.A.). A special thank to Dr. Fabrizio Cortezzi (Technical Manager of Ridracoli dam) and to all the technicians of the Ridracoli dam. I remember Massimo, Gianni and Tonina.

I would to thank all the friends and the people who I met throughout my doctoral journey, Elena, Celine, Robert, Luisa, Marco, Tommaso, and all my colleagues with which I shared houses, worries, difficulties and basically happiness, in particular Silvia, Laura and Sara. PhD is a journey, keep calm and enjoy.

As always, my family supported me at the most difficult moments and it rejoiced with me in those happier, for this all my gratitude goes to my parents.

The project has been also supported the by the Italian Ministry of Education, University and Research under PRIN grant No. 20154EHYW9 “Combined numerical and experimental methodology for fluid structure interaction in free surface flows under impulsive loading” and by the MIUR-DAAD Joint Mobility Program “Variational approach to fatigue phenomena with phase-field models: modelling, numerics and experiments”.

“Because an arch dam is curved, the difficulty would seem to be not to make it hold up, but to knock it down.”

A. Coyne (1956)

Contents

List of Symbols

N_p	number of points recorded in each scan
N_{gm}	number of markers used to geo-reference the scans
σ	standard deviation
ΔE	value of the differences along the east component
ΔN	value of the differences along the north component
ΔA	value of the differences along the altitude component
Δy_{1-2}	gap between the analyzed circumferences extracted by the UAV dense point cloud and the project geometry close to the main section 1-2
C_e	curvature centre of the upstream facing
C_1	curvature center of the innermost arch of the downstream facing
C_2	curvature center of the intermediate arch of the downstream facing
C_3	curvature center that describes the perimeter pulvino foundation
Δd_{Ce}	gap between the construction points C_e extracted by the UAV dense point cloud and the project geometry close to the main section
m	mass
c	dashpot parameter
k	spring parameter
$F(t)$	external force
t	time
$x(t)$	displacement
$\dot{x}(t)$	velocity
$\ddot{x}(t)$	acceleration
ξ	damping ratio
ω	natural circle frequency
f	natural frequency
T	period
$u(t)$	impressed displacement at the base of the L-cart
$y(t)$	absolute displacement of the mass
$\ddot{y}(t)$	absolute acceleration of the mass
q_j	lagrangian coordinate
Q_h	generalized force
$[M]$	mass matrix
$[C]$	damping matrix
$[K]$	stiffness matrix
u_j	constant
$g(t)$	general function of the time
λ	ratio between the second derivative of $g(t)$ and $g(t)$

$[X]$	matrix of eigenvectors
$[\Lambda]$	matrix of eigenvalues
φ	normal coordinate
$[I]$	identity matrix
$[A]$	diagonal matrix with $2\xi_i\omega_i$ diagonal terms
α	Rayleigh damping coefficient that takes into account mass proportional damping
β	Rayleigh damping coefficient that takes into account stiffness proportional damping
f_s	internal resisting force
$p(t)$	applied forces
τ	generic time
θ	parameter which relates acceleration with displacement and velocity
ι	parameter which relates acceleration with displacement and velocity
k_T	tangent stiffness
$R^{(j)}$	residual force
ε_R	residual force tolerance
ε_x	additional displacement tolerance
ε_w	incremental work tolerance
$\hat{f}_s$	resisting force
σ_R	stress normal to the radial direction
σ_θ	stress normal to the circumferential direction
R_e	extrados radius
R_i	intrados radius
R	current radius
ν	Poisson’s coefficient
s	generic thickness
s_s	top thickness
s_b	base thickness
p	generic pressure
p_b	base pressure
r	constant value of the medium fiber
E	Young’s modulus
p_a	hydrostatic load acting on the arches
p_m	hydrostatic load acting on the cantilevers
H	height
σ_a	stress on the unitary arch
σ_m	stress acting on the cantilever of unitary thickness
$\left[N_i^e\right]$	matrix of shape functions
$\left\{a\right\}^e$	vector of nodal displacment
S	linear operator
ε	strain
σ	stress
$\left[D\right]$	elasticity matrix
σ_0	initial residual stress

ε_0	initial residual strain
$\{\bar{a}\}$	virtual displacement
$\{\bar{\varepsilon}\}$	virtual strain
$\{f^B\}$	forces per unit volume
$\{f^S\}$	forces per unit surface area
$\{F^I\}$	concentrated loads
$[K]^e$	finite element stiffness matrix
γ_w	unit weight of the water
g	gravity acceleration
ρ_w	water density
$\boldsymbol{F}$	vector of the body force
$\boldsymbol{u}^f$	vector of the fluid displacement
$\dot{\boldsymbol{u}}^f$	vector of the fluid velocity
$\ddot{\boldsymbol{u}}^f$	vector of the fluid acceleration
ρ_f	fluid densty
μ_f	fluid viscosity
Φ	velocity potential
c_f	speed of sound in the fluid
K_f	bulk modulus
$\ddot{r}_{gy}$	seismic acceleration
$T(x)$	boundary traction
$\boldsymbol{u}^s$	vector of the solid displacement
$\ddot{\boldsymbol{u}}^s$	vector of the solid acceleration
ψ	reflection coefficient
a_{rms}	effective acceleration
a_i	generic i-th acceleration
I_H	Spectrum Intensity of Housner
$[Z]$	matrix of the constants Z_{ij}
G	shear modulus
μ, λ	Lamè’s constants
E_{oed}	oedometric constrained modulus
V_p	velocity of the longitudinal waves
V_s	velocity of the transverse waves
ρ	bulk density
$\mathbf{E}$	elastic stiffness tensor
$\boldsymbol{\sigma}$	Cauchy stress tensor
$\overline{\boldsymbol{\sigma}}$	effective stress tensor
$\boldsymbol{\varepsilon}^{\mathbf{e}}$	elastic strain tensor
$\boldsymbol{\varepsilon}^{\mathbf{p}}$	plastic strain tensor
$\mathbf{D}$	rank four tensor
$\boldsymbol{E}_0$	initial elastic-stiffness tensor

$\boldsymbol{I}$	four rank identity tensor
$\overline{F}$	scalar function of invariants of stress tensor
c_o	cohesion
o, ϖ	dimensionless constants
I_1	first invariant of stress tensor
J_2	second invariant of deviatoric stress tensor
σ_{max}	algebraic maximum principal stress
Φ	plastic potential flow
$\dot{\lambda}$	non-negative plastic multiplier
κ	internal variable set
W	function related to plastic dissipation
$\lVert s \rVert$	norm of the deviatoric stress
α_p	dilatancy
$\dot{\tilde{\varepsilon}}_t^{\,p}$, $\dot{\tilde{\varepsilon}}_c^{\,p}$	equivalent plastic strain rates
$\tilde{\varepsilon}_t^{\,p}$, $\tilde{\varepsilon}_c^{\,p}$	equivalent plastic strains
ϑ	temperature
f_i	predefined variables
d_t , d_c	uniaxial damage variables
d	function of the two uniaxial damage variables
w_t , w_c	material properties that control the stiffness recovery
$\hat{\dot{\varepsilon}}_{\max}^{pl}$, $\hat{\dot{\varepsilon}}_{\min}^{pl}$	max. and the min. eigenvalues of the plastic strain rate tensor $\dot{\varepsilon}^{pl}$
$\hat{\bar{\sigma}}_i$	principal stresses
$\tilde{\varepsilon}_t^{ck}$	cracking strain
ε_t, ε_c	total strain
ε_{t0}^{el}, ε_{c0}^{el}	elastic strain of the undamaged material
u_t^{pl}	plastic displacement
u_t^{ck}	cracking displacement
l_0	specimen lenght
σ_t, σ_c	generic stress value of the descending branch
σ_{cu}	peak value of the compressive stress diagram
E_s	static elastic modulus
E_d	dynamic elastic modulus
E'	drained Young's modulus
E_u	undrained Young's modulus
G'	drained shear modulus
G_u	undrained shear modulus
B	bulk modulus
f_{cd}	design compressive stress
ε_{cu}	maximum compressive strain
f_c	generic compressive stress
f_{ctd}	tensile design strength

f_{ct}	generic tensile stress
β_d	dilatation angle
m	eccentricity
f_y	ratio of biaxial compressive yield stress to uniaxial compressive yield stress
K_I	ratio of the second stress invariant on the tensile meridian to that on the compressive meridian for the yield function
μ_P	viscosity parameter
M_L	local magnitude
M_W	moment magnitude
V_R	reference period
T_R	return period

List of Abbreviations

UAV	Unmanned Aerial Vehicle
FEM	Finite Element Method
MCE	Maximum Credible Earthquake
SfM	Structure from Motion
DEM	Digital Elevation Model
SLC	Collapse Limit State
CER	Emiliano-Romagnolo canal
GCP	Ground Control Point
CP	Check Point
SLS	Serviceability Limit States
OLS	Operational Limit State
SLD	Damage Limit State
ULS	Ultimate Limit States
SLV	Life-Safety Limit State
ICOLD	International Committee on Large Dams
ITCOLD	Italian Committee on Large Dams
CAE	Computer-Aided Engineering
FEA	Finite Element Analysis
CDP	Concrete Damage Plasticity
PGA	Peak Ground Acceleration
PSD	Power Spectral Density

List of figures

List of Tables

Small Glossary for dams[i]

Base thickness. Also referred to as base width. The maximum thickness or width of the dam measured horizontally between upstream and downstream faces and normal to the axis of the dam, but excluding projections for outlets or other appurtenant structures.

Construction joint. The interface between two successive placements or pours of concrete where bond, and not permanent separation, is intended.

Crest gate (spillway gate). A gate on the crest of a spillway to control the discharge or reservoir water level.

Crest length. The measured length of the dam along the crest or top of dam.

Dam. An artificial barrier that has the ability to impound water, wastewater, or any liquid-borne material, for the purpose of storage or control of water.

Depletion sluice gate. A gate located at lowest level in the body of the dam to deplete the reservoir in the event of distress. It may be either wheel mounted type or sliding type.

Gallery. A passageway in the body of a dam used for inspection, foundation grouting, and/or drainage.

Height, structural. The vertical distance between the lowest point of the excavated foundation to the top of the dam.

Maximum flood control level. The highest elevation of the flood control storage.

Minimum operating level. The lowest level to which the reservoir is drawn down under normal operating conditions. The lower limit of active storage.

Normal reservoir level. For a reservoir with a fixed overflow sill the lowest crest level of that sill.

Slide gate (sluice gate). A gate that can be opened or closed by sliding in supporting guides.

Stilling basin. A basin constructed to dissipate the energy of rapidly flowing water, e.g., from a spillway or outlet, and to protect the riverbed from erosion.

Top thickness (top width). The thickness or width of a dam at the level of the top of dam (excluding corbels or parapets). In general, the term thickness is used for gravity and arch dams, and width is used for other dams.

---

[i] (Federal Guidelines for Dam Safety, 2004); (Module 4 - Hydraulic Structures for Flow Diversion and Storage)

1. Introduction and motivations

1.1 Problem statement

The safety and efficient maintenance of dams are primary aspects in the management of such strategic works [1]. Indeed, the failure of a dam can have tragic consequences, as testified by numerous dam break cases that occurred in the past [2,3,4,5]. The need to, ever more effectively, combine safety with the containment of maintenance costs directly linked to the service life of the structure requires innovative approaches beside traditional methods. Dams are built for several purposes, such as water supply, flood control, irrigation, navigation, and hydropower generation. Dams are often the basis of multipurpose projects [6,7]. In Italy there are 541 large dams, with an average life of over 50 years, which may extend to 70 years if the analysis is limited to the Alps [8]. Managers of restraining structures must ensure dam maintenance through frequent and continual activities, as well as fulfilling regulatory activities on the basis of information provided by institutional bodies [9].

The reduced accessibility of dams, both for uptake needs and for their strategic nature, does not facilitate direct visual inspection and a large amount of time is required for an inspection by traditional methods. Although a reliable terrestrial survey is still necessary, the use of UAVs – Unmanned Aerial Vehicles – is well suited for this purpose [10,11,12,13]. The use of UAVs is spreading to the safe inspection of sections of infrastructure that would otherwise not be directly accessible, except with expensive and dangerous procedures such as climbers. The state of conservation of the materials can be monitored in order to guarantee a proactive maintenance of the structure [14]. Moreover, in most cases, the project geometry of structures is missing important structural elements (i.e. construction joints) and/or of ancillary works (i.e. spillways, a stilling basin, weight blocks). Therefore, the high accuracy of UAV surveys makes possible the three-dimensional geometry modelling of such details in cases of structures with access inspection difficulties due to vertical surfaces or mountain areas such as dams.

It is commonly accepted that the FEM – Finite Element Method – modelling of dams is paramount in the safety evaluation of this type of structure [15,16,17]. Seismic analyses under real and design ground motions have to be performed in order to investigate the effective behaviour of the dam system [17]. Some structural details, such as the aforementioned construction joints, have to be included in FEM representations in order to verify not only the global behaviour of the structure but also that of local elements under severe design earthquakes such as the MCE – Maximum Credible Earthquake – event. Ensuring the functionality of construction joints in relation to the required limit state is strictly related to the seismic assessment vulnerability of the whole structure.

1.2 Objectives

For structures such as segmented arch dams built on valleys with complex topography, the detailed definition of the structure geometry – including the joints between the different blocks – and of the foundation rock mass is of primary importance in the FE modelling of such systems.

The present thesis aims to provide a guide that covers the entire process from the UAV surveying to the dense point cloud validation, to the three-dimensional FEM modelling of masonry dams applied to a concrete arch gravity dam located in central Italy: the Ridracoli dam. The focus is on the vertical construction joints modelling, the following aspects are investigated: the influence of vertical joint modelling on the dynamic properties of the model and their verification under severe earthquakes such as seismic vulnerability assessment of the whole structure.

The main objectives of the present thesis can be summarized as follows:

- validation of the UAV technique into dam surveying by means of traditional topographic methods such as Total Station, GPS Station and Laser Scanner;
- three-dimensional solid modelling of a whole dam system starting from a UAV survey, indeed, the SfM – Structure from Motion – technique allows for the reconstruction of 3D objects from 2D images. Pre-existing data sets such as design geometry, DEM – Digital Elevation Model – of the area and bathymetry of the lake are employed for the integration of the UAV dense point cloud. The high level of detail of the UAV survey allows for the geometric reconstruction of important elements of the structure such as the spillway, vertical and *pulvino* foundation joints and of the ancillary works such as stilling basin and weight blocks;

Figure 1.1. (a) Geographical collocation of the Ridracoli Dam (red point) scale 1:200Km; (b) The lake created by the presence of the dam, scale 1:500 m [19].

- proposal of an operative procedure for the calibration of Rayleigh damping parameters of the FEM models of rock mass and of dam body based on real seismic records;
- the influence of vertical construction joint modelling on the dynamic behaviour (i.e. natural frequencies, mode shapes) of the structure is investigated, three models are analyzed: monolithic, surface-to-structure and solid element joint representations;
- the calibrated FEM model with solid elements such as joints is employed for a nonlinear damage dynamic analysis under the SLC – Collapse Limit State – seismic event selected as the MCE event of the site. The tensile damage evolution throughout the joint elements is investigated for three different water levels. All simulations take into account the structure-foundation interaction by means of a suitable extension of rock mass and the fluid-structure interaction by means of acoustic elements.

The thesis is organized as follows: the first part describes the system of integrated survey, composed of UAV, Total Station, GPS Station and Laser Scanner, employed on the Ridracoli dam; indeed, the second chapter illustrates the new validation procedures by points, lines and surfaces of the UAV dense point cloud. The second part of the thesis focuses on the finite element

Figure 1.2. The Ridracoli dam.

modelling of arch-gravity dams and on the related static and dynamic analyses. Indeed, the third chapter gives a general overview of the state of the art of arch-gravity dams and of finite element modelling procedures. The fourth chapter goes on to describe the innovative solid modelling procedure from the integrated dense point cloud to the FEM model, the focus is on the vertical joint modelling procedures, monolithic, surface-to-structure and solid element joint representations. In the fifth chapter are presented: linear elastic static analyses, linear elastic dynamic analyses to calibrate the Rayleigh damping parameters and elasto-plastic damage time-history analyses. Finally, results and main conclusions are illustrated in the sixth chapter.

1.3 Case of study

The Ridracoli dam, managed by Romagna Acque Società delle Fonti S.p.A., is located in the village of Santa Sofia in the province of Forlì-Cesena, Emilia Romagna, Italy, Fig. 1.1a. The dam is placed along the Bidente river, regulating its flow during the year, Fig. 1.1b. The Ridracoli dam is the key work of the Romagna aqueduct, which includes other important water intake structures such as the recent Standiana water purifier close to Ravenna, which treats the water of the Po river diverted by the CER – Emiliano-Romagnolo canal –, the NIP purifier, which treats the water diverted from the Lamone and Reno rivers and several local sources of supply (springs and aquifers). In the Rimini area, where several water well fields are located, the Conca dam is placed. It is mostly useful during the summer period. There are more than 600km of water mains in Romagna’s water distribution system [18]. The primary use of the Ridracoli reservoir is to supply drinking water of 48 municipalities in the provinces of Forlì-Cesena, Ravenna and Rimini and, since 1989, of Republic of San Marino, providing alone 50% of the entire water needs of the system. The secondary function of the reservoir is the production of hydroelectricity for the surrounding area. The Ridracoli dam is a simple concrete arch gravity dam, 103.5m high, with a crest 432m long, Fig. 1.2. The reservoir surface area is 1.035km^2, it has a capacity of 33Mlm^3 and the total surface area of the drainage basin is 87.510km^2. The construction of the Ridracoli dam started in 1975 and it was completed in 1982. After the testing phase, in 1988 the reservoir became operational.

1.4 Chapter bibliography

[1] Wilson H. Tang and Ben Chie Yen, "Dam Safety Inspection Scheduling" *Journal of Hydraulic Engineering*, vol. 117, no. 2, pp. 214-229, Feb. 1991.

[2] Y. Zech and S. Soares-Frazão, "Dam-break flow experiments and real-case data. A database from the European IMPACT research" *Journal of Hydraulic Research*, vol. 45, no. sup1, pp. 5-7, Dec. 2007.

[3] David C. Froehlich, "Embankment Dam Breach Parameters and Their Uncertainties" *Journal of Hydraulic Engineering*, vol. 134, no. 12, pp. 1708-1721, Dec. 2008.

[4] Chiara Biscarini, Silvia Di Francesco, Elena Ridolfi, and Piergiorgio Manciola, "On the Simulation of Floods in a Narrow Bending Valley: The Malpasset Dam Break Case Study" *Water*, vol. 8, no. 11, p. 545, Nov. 2016.

[5] Byunghyun Kim and Brett F. Sanders, "Dam-Break Flood Model Uncertainty Assessment: Case Study of Extreme Flooding with Multiple Dam Failures in Gangneung, South Korea" *Journal of Hydraulic Engineering*, vol. 142, no. 5, p. 05016002, May 2016.

[6] Cecilia Tortajada, "Dams: An Essential Component of Development" *Journal of Hydrologic Engineering*, vol. 20, no. 1, p. A4014005, Jan. 2015.

[7] ICOLD CIGB > Role of Dams. [Online]. http://www.icold-cigb.org/GB/dams/role_of_dams.asp

[8] Fornari Francesco Marcello Aldo, "Riabilitation of dams in Italy" *Final ITCOLD report*, 2012.

[9] P Manciola and S Casadei, "Criteria for the evaluation of the rate of water use in a river basin", Proceedings of a Boulder Symposium, n° 231, 1995.

[10] I. Colomina and P. Molina, "Unmanned aerial systems for photogrammetry and remote sensing: A review" *ISPRS Journal of Photogrammetry and*

Remote Sensing, vol. 92, pp. 79-97, June 2014.

[11] A. Ellenberg, L. Branco, A. Krick, I. Bartoli, and A. Kontsos, "Use of Unmanned Aerial Vehicle for Quantitative Infrastructure Evaluation" *Journal of Infrastructure Systems*, vol. 21, no. 3, p. 04014054, Sep. 2015.

[12] Anand Vetrivel, Markus Gerke, Norman Kerle, and George Vosselman, "Identification of damage in buildings based on gaps in 3D point clouds from very high resolution oblique airborne images" *ISPRS Journal of Photogrammetry and Remote Sensing*, vol. 105, pp. 61-78, July 2015.

[13] A. Ellenberg, A. Kontsos, I. Bartoli, and A. Pradhan, "Masonry Crack Detection Application of an Unmanned Aerial Vehicle" in *Computing in Civil and Building Engineering (2014)*, Reston, VA, 2014, pp. 1788-1795.

[14] Riccardo Salvini, Giovanni Mastrorocco, Marcello Seddaiu, Damiano Rossi, and Claudio Vanneschi, "The use of an unmanned aerial vehicle for fracture mapping within a marble quarry (Carrara, Italy): photogrammetry and discrete fracture network modelling" *Geomatics, Natural Hazards and Risk*, vol. 8, no. 1, pp. 34-52, Jan. 2017.

[15] ICOLD, "Buletin 30 - Finite elements methods in analysis and design of dams", 1978.

[16] ICOLD, "Bulletin 52 - Earthquake analysis for dams", 1986.

[17] ICOLD, "Bulletin 155 - Guidelines for use of numerical models in dam engineering", 2013.

[18] Consorzio Acque per le Province di Forlì e Cesena, *L'acquedotto della Romagna [Aqueduct of Romagna]*, 1991.

[19] Istituto Nazionale di Geofisica e Vulcanologia. [Online]. http://www.ingv.it/en/

2. High fidelity reconstruction by unmanned aerial vehicle: system of integrated survey and validation

2.1 State of the art and case of study

UAV techniques are employed in surveys and metrical reconstruction in different fields, such as vegetation analysis [1], coastal areas [2], agriculture enhancement [3] and the inspection of the natural environment [4], historical buildings [5] [6] [7] [8], bridges and viaducts [9] [10], large scale structures (e.g. retaining walls [11]); civil buildings, chimneys and torches.

From the huge UAV photographic set, it is possible to obtain qualitative information, with the aim of recognizing the condition of the materials, as well as quantitative information. The "Structure from Motion" technique allows for the reconstruction of three-dimensional objects from two-dimensional images [13] [14] [15] [16] in order to create a 3D model of the acquired structure [17] [18]. Nevertheless, an extensive topographical survey, by Total Station, GPS and Laser Scanner [19], is still necessary to geo-reference and validate the UAV dense point cloud.

Not ever in the aforementioned works, a study on the accuracy and precision of the survey was done, comparing the UAV technique with the traditional ones such as Total Station, GPS Station and Laser Scanner. Moreover the use of UAV equipment on dams is rare and at an early stage, e.g. Naumann et al., 2013 [12]. One of the aims of the thesis is to provide an operative procedure for the three-dimensional geometric reconstruction by UAV of a concrete arch gravity dam.

Indeed, the present study is a technological comparison between traditional topographic instruments and unconventional photogrammetry conducted by UAV. The topographic instruments used include Total Station (TS30 Leica-Geosystems), GPS Satellite Station (1230 Leica Leica-Geosystems) and Laser Scanner (Z+F 5010 ZoellerFroelich). The drone used is a four propeller HIGHONE 4HSEPRO, with an autonomy of 18-30 minutes and a Gimbal system with SONY Alpha 7R, 36.4 Mpix Full frame camera. Video images were acquired with a LUMIX GH4 Full Frame camera (FullHD video 1920x1080 29fps). Flight operations were performed in manual mode and image-shooting operations were followed by a second flight operator who was able to assess the entity of overlapping frames. The integrated survey system makes it possible to validate and geo-reference the model. In this way topographic instruments act as a support for the drone and validate the survey. To verify the acquisitions made by the drone, a laser scanner survey was performed. The resulting scans were compared with drone analysis, in analogy to the work performed by Andrews et al. (2013) [20] for a historic building. Most surveys of existing structures employ only laser scanner analysis, as performed on a historical tower by Achille et al. (2015) [5]. Punctual, linear and surface analyses are then performed, assuming the traditional topographic data as reference, to evaluate the accuracy of the UAV survey. Moreover, in order to integrate the UAV information, some additional data sets have to be employed such as design project of the structure, a DEM of the surrounding area and the bathymetry of the lake.

2.2 Marker placement

To geo-reference the images shot during the UAV survey, in addition to natural points, it is necessary to place a proper number of markers on the dam and the surrounding areas, Fig. 2.1. Natural points, to be considered as reference points, have to be fixed points, well visible and representative of the structure geometry such as curvature changes or vertices. Have been employed 62 natural points. It was not possible to consider only natural points because of the structure is mostly vertical and monochrome. A total of 226 markers of 40X40cm in size were stably applied with the aid of non-invasive fastening and simple removal techniques. The placement followed criteria of uniformity in distribution and visibility. Markers were placed on points identified as significant for the following finite element modelling. The markers were placed on the dam crest, on the parapet walls on either side of the roadway on the crest, on the adjacent portions of soil, on the step of the foundation base, on the stilling basin, and on the upstream facing dam. Markers were placed at the hydrostatic level at the time of operations using a boat. The marker application operations employed three two-man teams for three days. In literature there are no indications regarding a method which optimizes the distribution of markers in the case of a vertical structure survey; there are only some applications on extended horizontal surfaces [20] [21] [22] or related to traditional topographic techniques such as Laser Scanner [23]. A further development of this work focuses on the investigation of optimal marker placement in terms of numbers and configurations, Ridolfi et al., 2017 [24].

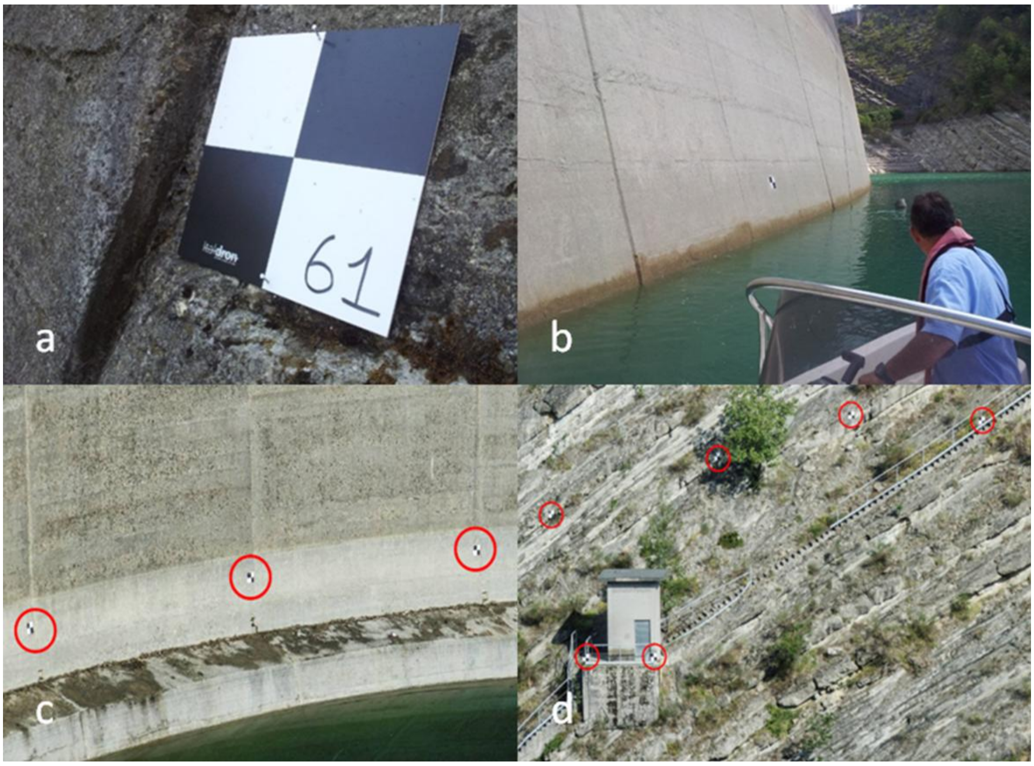

Figure 2.1. (a) Marker applied near a joint; (b) Marker application on the upstream face; (c) Marker application on the downstream face near the foundation base; (d) Marker application on an area located on the left side.

2.3 The flight and survey restitution by UAV – photogrammetric modelling

UAV flight operations were concentrated in a single day and aimed to cover with photographic frames the downstream facing dam, the upstream facing dam up to the hydrostatic level, the crest, the stilling basin, the right and left sides, the picnic area, the guardhouse and part of the surrounding land. 19 flights lasting 15 min/flight were performed in one working day, providing a total of 4600 frames at 36 megapixel resolution. The shooting operations were performed remotely by a second flight attendant, who evaluated the entity of overlapping frames. The distance of the UAV from the dam surfaces was around 15-25m. In some areas, in fact, such as the downstream face, a flight at close range would be dangerous because of the warm ascending air flows due to the temperature difference between the bottom and the top of the structure. Moreover these air updrafts and the complexity of the structure geometry did not allow an autopilot survey and manual flights have been performed. The post-processing of the acquired data was the most time-consuming procedure. The high resolution frames at 7360x4912 pixels have been divided in subareas, downstream and upstream faces, crowing of the dam, left (warden house and recreation area) and right sides, stilling basin and galleries in order to share the computational cost of the creation of the whole dense point cloud model. The build of every partitioned model employed about 5 days, including the frames loading and the GCPs – Ground Control Points – picking, using medium-high performance hardware (Intel® Core™ i7 processor, 32 GB RAM, Nvidia® GeForce GTX graphics). The procedure took 45 working days plus the time required for assembly, overlap and refine the dense point cloud parts that employed other 15 working days. The 3D model was realized through the SfM – Structure from Motion – technique [13]. This technique allows for the reconstruction of the geometry of objects through the automatic collimation of points from a series of images. The reconstruction of the Dense Point Cloud was made using the SfM processing Cloud Compare® software for subsequent stages. Firstly, the 36 megapixel images were analyzed and geo-referenced using marker coordinates. Secondly, the frames were aligned and a cloud of low-density points was created; following this, another point cloud with a higher density was produced. On this high-density model a three-dimensional textured mesh was applied, Fig. 2.2.

2.4 Conventional GPS and Total Station surveying

Two topographical networks were defined by Total Station. A primary network was identified, made up of 4 locations named BS, SS, DS and BD, Fig.

Figure 2.2. Texturized 3D mesh of the road way on the dam crest.

2.3. The four points coincide with the pillars currently used to periodically monitor the dam. A secondary network was also created consisting of materialized points with nails driven into the ground, and this was connected to the primary network through topographic measurements. The primary and secondary networks detected a total of 417 points of the structure and the surrounding land, including markers and natural points. To obtain temporally homogeneous data, the topographic acquisition from Total Station and the frames acquired with the UAV technique were carried out simultaneously. The four vertices of the primary network were marked with GPS instrumentation and the obtained coordinates were converted into the Gauss – Boaga cartographic system and z-coordinates to properly geo-reference the entire model. For the transformation, the cartographic grid 107606.gk2 (Verto 3K), provided by the Military Geographical Institute (IGM) with reference to the vertices 107606 Santa Sofia (Poggio la Guardia), located a few hundred meters from the top of the dam, was employed. The coordinates of the measured points have a standard deviation lower than 1.0 cm in the 3 components East, North and Height, and 0.7 cm on average. The coordinates have a small dispersion around their mean values, Tab. 2.1. It is interesting to note that the standard deviation values confirm the suitability of these 417 points for use in the geo-referencing of UAV frames and in the validation of the same model.

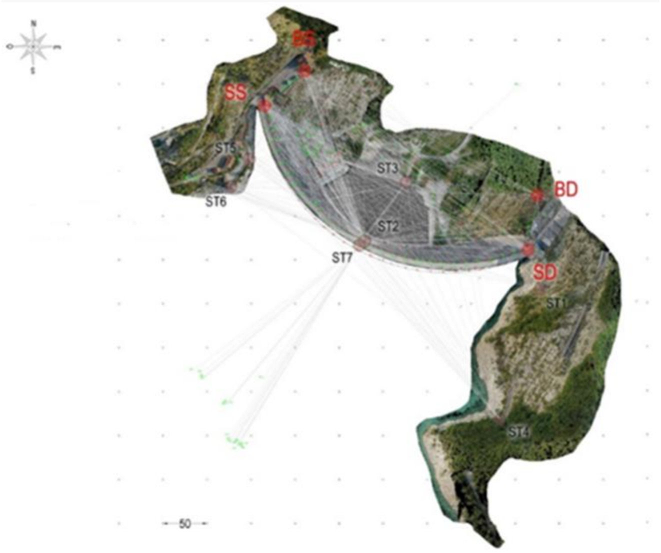

Figure 2.3. Topographic Networks: a first network is composed of the 4 vertices (i.e. SS, BS, SD and BD) and a second network is composed of 11other bases by which a total 417 points made of markers and natural points were acquired by the Total Station.

Table 2.1. Standard Deviation of the 417 point coordinates detected by Total Station. The low σ values show the limited dispersion of the acquired coordinates along the three components.

	Standard Deviations		
Total Station	**East (m)**	**North (m)**	**Altitude (m)**
Maximum Values	+0.010	+0.010	+0.008
Medium Values	+0.006	+0.007	+0.004

2.5 Laser Scanner surveying

To verify the acquisitions made by the drone, a laser scanner survey was performed. The dam model obtained by the laser scanner survey involved nine acquisition workstations in order to acquire most of the surface area of the structure. Fig. 2.4 shows the basis of the acquisition and each corresponding analyzed area. The survey operations employed a two-man team for three days. The selection of the aforementioned markers was used to geo-reference the scans. The decision to use part of the same markers of the photogrammetric model was made to ensure the perfect match between the two image data sets. To record each individual scan, 53 markers were employed, whose topographic coordinates, acquired by Total Station, are characterized by an average standard deviation of less than 1 cm, Tab. 2.1. Tab. 2.2 shows the results of recording scans. The residuals between the marker coordinates acquired by Total Station and Laser Scanner have average values in all cases less than 1 cm, and the correspondent standard deviations do not exceed the value of 5 mm. It is interesting to note that these values are lower than both the accuracies and the standard deviations of the topographic coordinates acquired by Total Station. Therefore the scans are suitable to be taken as reference scans. Furthermore, Table 2.2 shows that the maximum and minimum differences are less than 15 mm in the three components of E, N and H. As a result it is possible to attribute an overall accuracy to the laser scanner model of approximately 15 mm in the three components E, N and H.

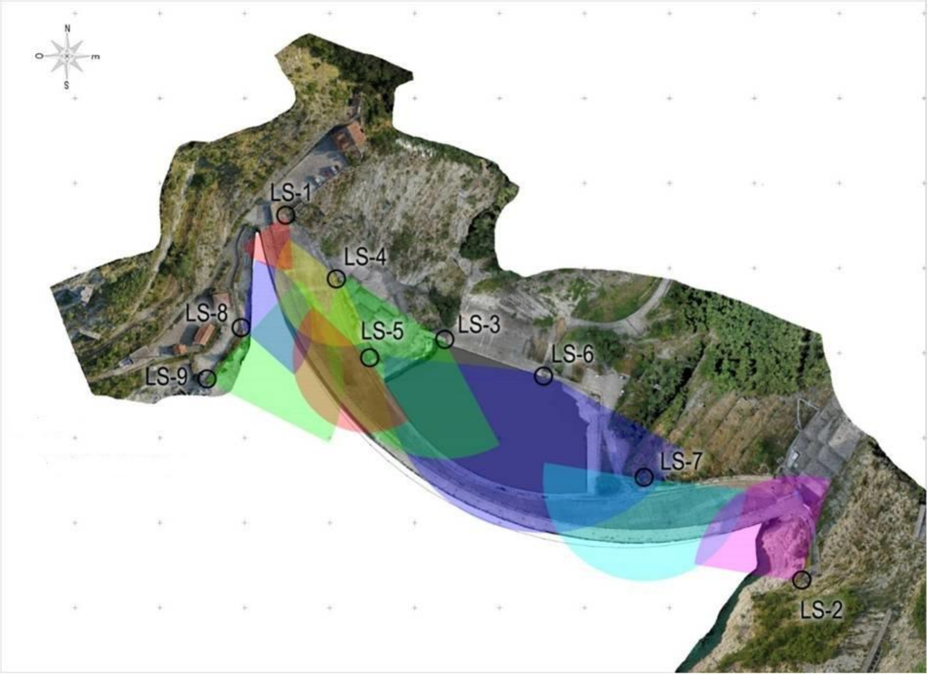

Figure 2.4. Laser Scanner acquisition points and corresponding analysed areas.

Table 2.2. Laser scanner scans information and comparison with Total Station data: number of points recorded in each scan (N_p), number of markers used to geo-reference the scans (N_{gm}), differences between target coordinates acquired by Total Station and Laser Scanner in terms of average value, standard deviation (σ), maximum and minimum value of the differences along the three components (i.e. east (E), north (N) and altitude (A)).

			Differences							
Laser Scanning	**N_p (Ml)**	**N_{gm}**	**Average value (cm)**	**σ (cm)**	**ΔE max (cm)**	**ΔN max (cm)**	**ΔA max (cm)**	**ΔE min (cm)**	**ΔN min (cm)**	**ΔA min (cm)**
LS-1	16	4	+0.5	+0.2	+0.2	+0.2	+0.5	-0.3	-0.5	-0.3
LS-2	192	7	+0.9	+0.3	+0.4	+1.1	+0.7	-0.8	-0.5	-0.8
LS-3	268	23	+0.8	+0.4	+1.1	+1.3	+1.0	-0.8	-1.0	-1.4
LS-4	340	7	+0.9	+0.4	+1.1	+1.0	+1.3	-1.4	-0.8	-0.4
LS-5	392	6	+0.9	+0.4	+0.6	+1.2	+0.5	-0.8	-0.6	-0.9
LS-6	256	25	+0.8	+0.4	+1.2	+1.4	+1.0	-1.0	-1.0	-1.1
LS-7	320	5	+0.7	+0.5	+1.4	+0.6	+0.2	-0.5	-0.6	-0.3
LS-8	208	7	+0.5	+0.2	+0.6	+0.6	+0.3	-0.5	-0.6	-0.4
LS-9	124	4	+0.9	+0.2	+0.8	+0.7	+0.7	0.4	-0.2	-0.7

2.6 Data validation

The validation of the data acquired by the unmanned aerial vehicle was conducted in several phases, and takes as reference the coordinates of markers and natural points acquired by total station and scans acquired by laser scanner. These measures are more precise than those of the UAV survey. Therefore the Total Station and Laser Scanner data sets are suitable for the verification of the UAV data surveying. The analysis concerned the evaluation of spatial density, the correspondence of specific points, and linear and surfaces comparisons. In the following subsection the dense point cloud validation is presented, and an evaluation for density, points, lines, and surfaces is performed.

2.6.1 Dense point cloud spatial density validation

The first analysis of the Dense Point Cloud obtained from the acquisition made by UAV is an evaluation of the spatial distribution of the UAV cloud points. We split the dense point cloud into thirteen portions to manage the huge amount of data: 1. Downstream face, 2. Picnic Area, 3. Left side, 4. Crest, 5. Guard house, 6. Upstream face 1st Level, 7. Galleries, 8. Right side, 9. Downstream right face, 10. Pulvino (saddle foundation), 12. Stilling basin and 13. Upstream face 2nd Level. The level of goodness of the acquired measures, in terms of density, depends on the dimension of the elements that have to be reproduced in the FEM model. The vertical joint elements are the smaller entities that have to be modeled and they are 10cm thick. Therefore, the UAV dense point cloud should have a point density able to capture these elements.

The spatial density of points is almost uniform, as can be appreciated from Fig. 2.5, and estimated at a grid 1cm x 1cm in size. Each block, in which the point cloud has been divided, is used for the construction of the point density map. The minimum density is one point every 9 cm^2 (grid 3cm x 3cm in size), with a mean value of a one point every 1 cm^2 (grid 1 cm x 1 cm in size). Figs. 2.6 and 2.7 present the density point maps of some blocks. The lower density is obtained in the areas covered by vegetation, while structural concrete elements are characterized by the highest concentration of points. Tab. 2.3 illustrates in detail the number of points and the information related to the density of each analyzed block. The Dense Point Cloud has subsequently been purified, in a semi-automatic way, from the main outliers. The UAV Dense Point Cloud is the highest resolution information and it has to be used as a reference and as a starting point for all subsequent processing. The mesh generation from the Dense

Point Cloud determines a drastic under sampling of the points with a consequent loss of information. Thus the metric use of the mesh is to be avoided and all the operations of extraction of the vertical sections, of the level curves and of the solid structure reconstruction were achieved starting from the base data of Dense Point Cloud.

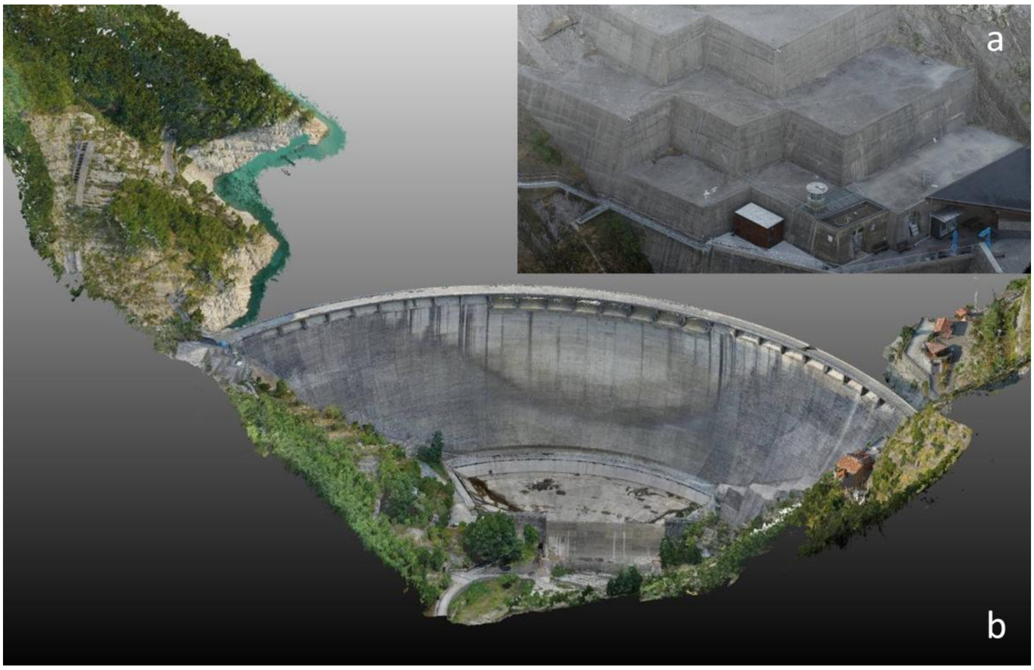

Figure 2.5. a) Dense Point Cloud of the concrete blocks on the right side obtained from UAV – Unmanned Aerial Vehicle – acquisition; b) Dense point cloud of the whole dam system obtained from UAV – Unmanned Aerial Vehicle – acquisition.

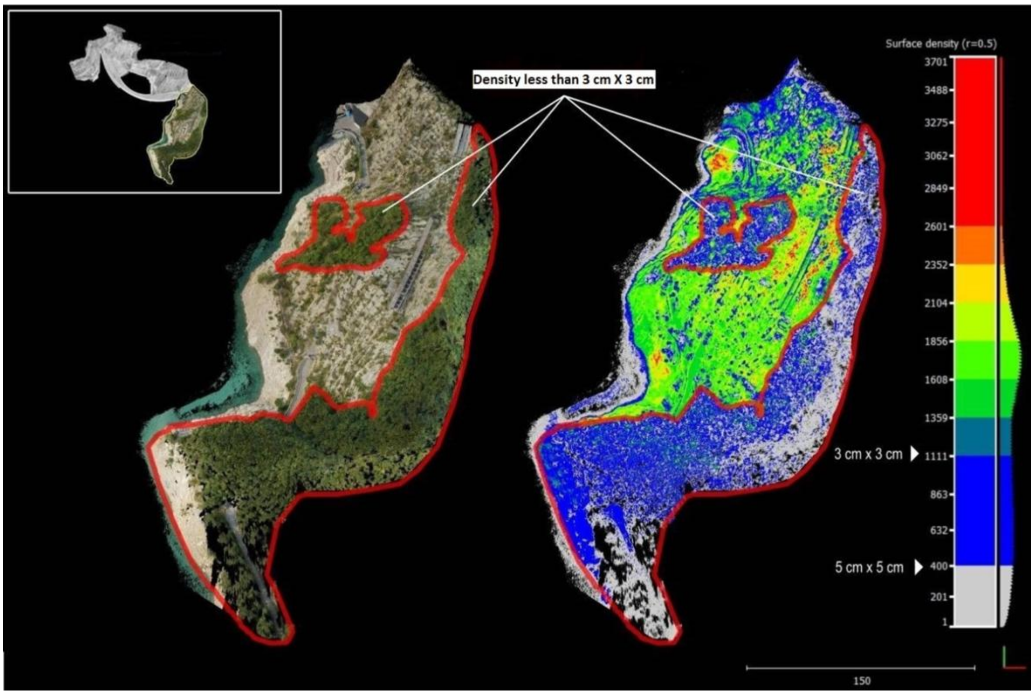

Figure 2.6. Points density analysis of Block 7, this is an area covered by vegetation and here the points density is lower than in other parts such as the structural parts. The points density is lower than a grid 3X3 cm in size.

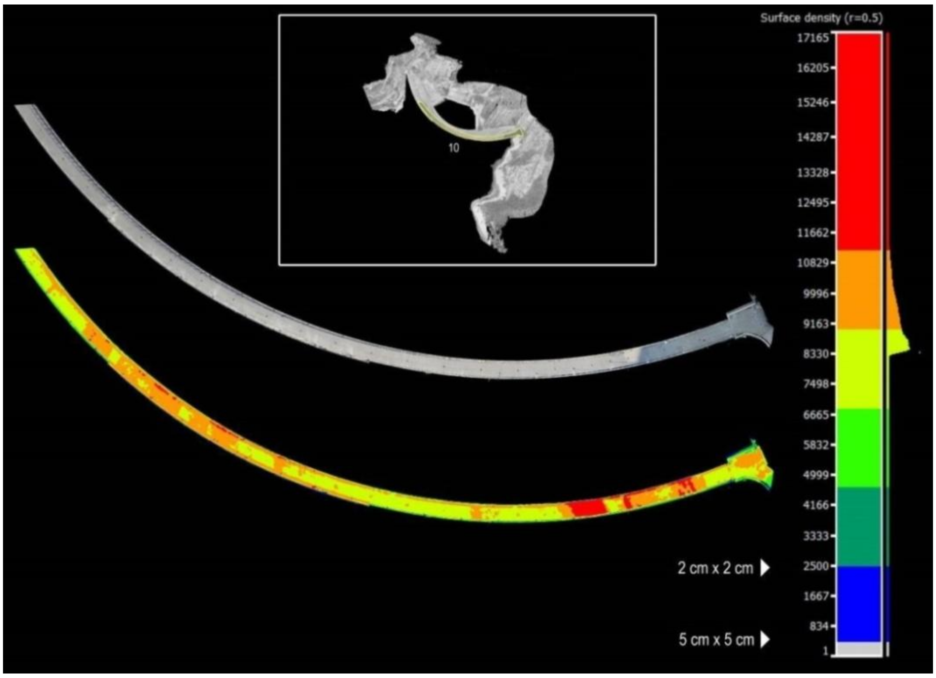

Figure 2.7. Points density analysis of Block 10. In this case the points density is around a grid 1X1 cm in size. Structural parts have a higher points density than those covered by vegetation.

Table 2.3. Density of the different Dense Point Cloud blocks in points/m^2 and in grid dimensions.

Block	**Medium Density (points/m^2)**	**Grid Dimension (cm X cm)**
1	12904	1 X 1
2	4030	2 X 2
3	2155	2 X 2
4	28662	1 X 1
5	1357	3 X 3
6	27511	1 X 1
7	1244	3 X 3
8	5745	1 X 1
9	6793	1 X 1
10	8827	1 X 1
11	2993	2 X 2
12	7243	1 X 1
13	6736	1 X 1
Average	**8938**	**1 X 1**

2.6.2 UAV dense point cloud validation by Total Station surveying points

The control of points consists in comparing the coordinates of significant points (markers and natural points) acquired by total station and those corresponding to the points of the dense point cloud generated by photogrammetry. A total of 218 points are analyzed, of which 146 GCP, 10 CP – Check Point – and 62 natural points, in accordance with the distribution shown in Fig. 2.8. The analysis of the residues, Tab. 2.4, shows that all points have a low mean value and a low standard deviation, thus the entire model has the same level of accuracy. The substantial uniformity of the generated global model is demonstrated by the homogeneity of the average values and standard deviations of the different types of points analyzed with respect to the 3 components East (E), North (N) and Altitude (A).

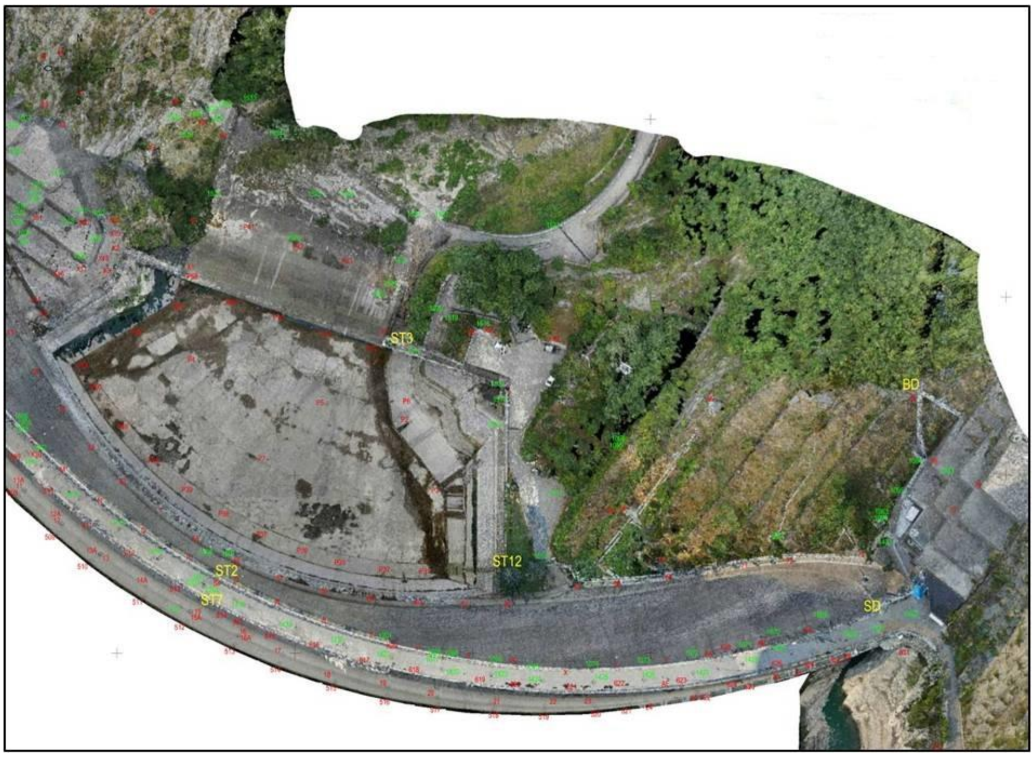

Figure 2.8. Planimetry of the acquired points (markers in red, natural points in green and laser scanner acquisition bases in yellow).

Table 2.4. Coordinate residuals of the analysed points, markers (GCP – Ground Control Points and CP – Control Points) and natural points in terms of average vales, standard deviations and minimum and maximum values.

	Markers						**Natural Points (62)**		
	GCP (146)			**CP (10)**					
	ΔE (cm)	**ΔN (cm)**	**ΔA (cm)**	**ΔE (cm)**	**ΔN (cm)**	**ΔA (cm)**	**ΔE (cm)**	**ΔN (cm)**	**ΔA (cm)**
Average	+1.0	0.0	0.0	-1.0	+1.0	0.0	0.0	0.0	0.0
Standard Deviation	+2.0	+2.0	2.0	+2.0	+2.0	+1.0	+3.0	+3.0	+2.0
MIN	-9.0	-6.0	-6.0	-4.0	-1.0	-1.0	-6.0	-10.0	-8.0
MAX	+8.0	+5.0	+5.0	+2.0	+5.0	+1.0	+6.0	+7.0	+6.0

2.6.3 UAV dense point cloud validation by Laser Scanner lines

The verification for lines consists in the comparison between the horizontal sections (contour lines) extracted from the point cloud measured by laser scanner and those obtained by UAV. In this comparison the laser scanner point cloud is taken as “Reference” while Dense Point Cloud from UAV as “Compared”. Nine contour lines are taken into account with a distance of 10 meters (A_{min}=478 m a.s.l. e A_{max}=558 m a.s.l.), Fig. 2.9. The thickness of the slices of points extracted is equal to 3cm, the set value as a function of the average points density, corresponding to 1 point every 9 cm^2 (a grid 3cm x 3cm in size), Fig. 2.10a. The accuracy of the contour lines is in accordance with those assigned to the laser scanner survey and previously quantified at about 1.5 cm. In almost all cases the measured points are in a 1.5 cm slice of the polyline automatically generated from the laser scanner points, Fig. 2.10 a. This characteristic is found on the whole extension of the extracted contour lines, and therefore they are suitable to act as a “Reference” for the validation of the corresponding curves extracted from the Dense Point Cloud by UAV. Nine horizontal sections are then extracted from the UAV Dense Point Cloud at the same height of those extracted by laser scanner survey. A visual analysis shows how the UAV survey data are characterized by a greater dispersion, especially near fast bend changes, Fig. 2.10 b. The joints of the structure are not easily detectable by extracting horizontal sections, but they can be characterized by the analysis of the RGB information of the Dense Point Cloud, as shown in Fig. 2.11. The quantitative analysis focuses on the evaluation of the distance between the points that compose the UAV level curves and the polylines extracted from the laser scanner survey employed as “Reference”. The results are summarized in Tab. 2.5. The average distance is of the same order of magnitude as that which characterizes the accuracy of the polylines in the laser scanner survey, which acts as “Reference”. A wider gap is only reached at the at the spillway level where the geometry of the structure is very complex.

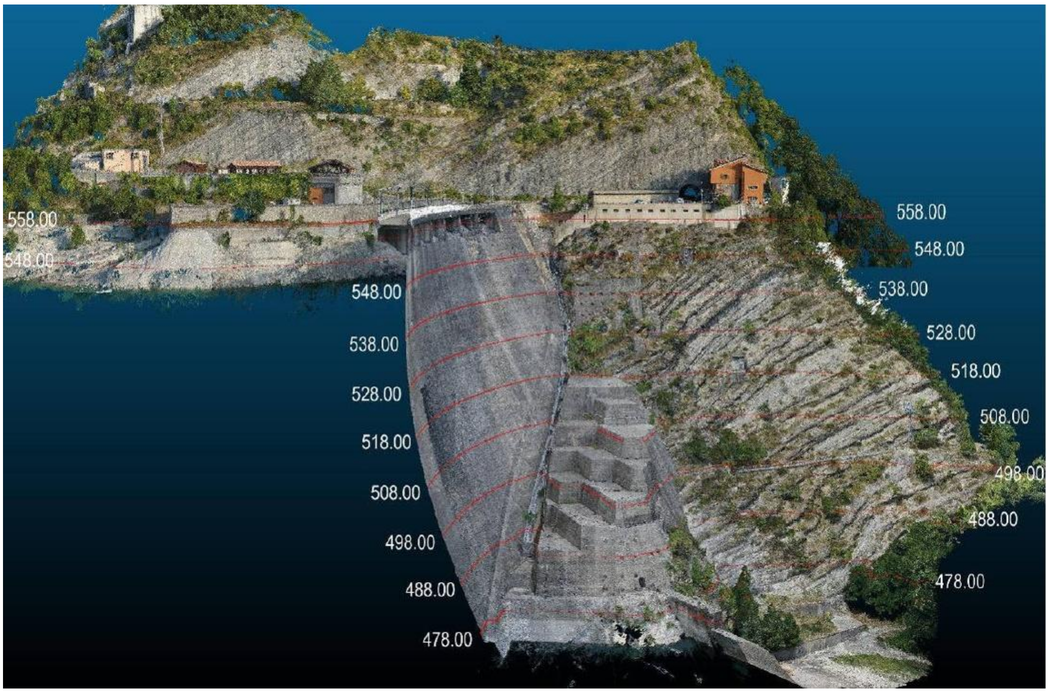

Figure 2.9. Analyzed Horizontal Section on the UAV dense point cloud.

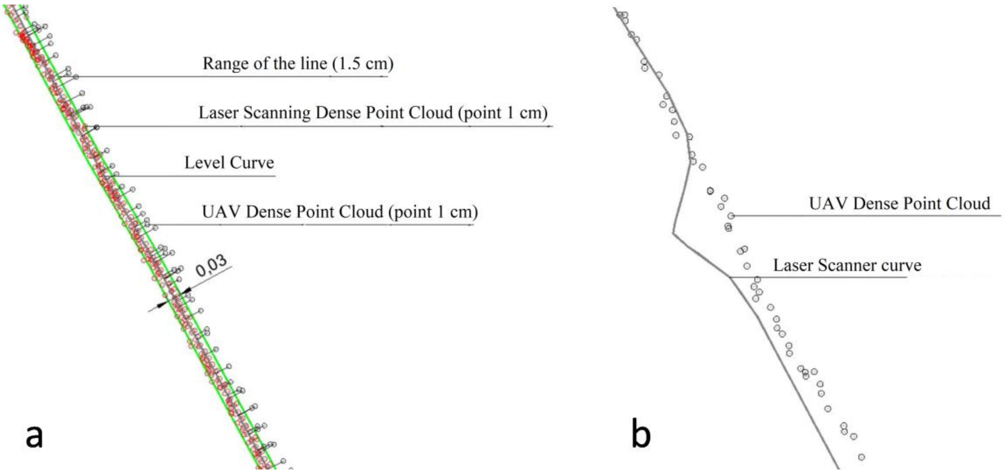

Figure 2.10. a) Overlap Dense Point Cloud by Laser Scanner (red points) and by UAV (black points). The level curve that interpolates the laser scanner points and the 3 centimeter laser scanner gap are also reported; b) Comparison between Laser Scanner and UAV level curves, near rapid curvature changes the UAV technique cannot recognize the variation.

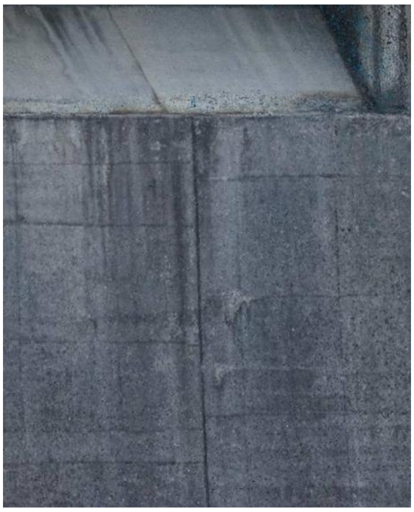

Figure 2.11. UAV Dense Point Cloud. A small variation such as joints can be recognized by the RGB information associated with the points.

Table 2.5. Comparison between UAV points slices and Laser Scanner curves at the same level, the medium distance between the UAV points and the laser scanner curves is of the same order of magnitude as the standard deviation of the TLS curves.

Curves	**Altitude Curves (m a.s.l.)**	**N° points**	**Medium Distance TLS – UAV curves (cm)**	**Standard Deviation TLS curves (cm)**
1	558	6680	+4.0	+3.5
2	548	10816	+2.0	+1.7
3	538	16091	+2.0	+1.4
4	528	11313	+1.0	+10
5	518	12026	+1.0	+1.0
6	508	12181	+1.0	+1.0
7	498	15306	+1.0	+1.3
8	488	7513	+2.0	+1.7
9	478	3680	+3.0	+2.0

2.6.4 UAV dense point cloud validation by Laser Scanner surveying surfaces

The third control phase covers the comparison between laser scanner surfaces and the UAV Dense Point Cloud. The analysis concerned different representative portions, vertical development zones, spillways, fast curvature changes like joints, connection of pulvino foundation-dam body and weight blocks, Fig. 2.12. CloudCompare® has been the work environment for the management and the evaluation of the validity of the Point Clouds. At first the interest portions are extracted from the Laser Scanner point cloud. From these, interpolating triangular meshes are built. The average variances and the standard deviations between the two entities are evaluated employing the points as "Reference" entities and the mesh as "Compared" through the Distance computation. This operation evaluates the substantial absence of variances assigning therefore to the mesh surfaces an accuracy equal to that of Laser Scanner points of 1.5 cm, Tab. 2.6 (A and B Columns). The mesh surfaces by Laser Scanner is then employed as, this time, "Reference" for the "Compared" Dense Point Cloud by UAV. The real comparison in fact is the evaluation of the distances between the mesh surfaces by Laser Scanner and the Dense Point Cloud by UAV. Below the analysis of different specimens taken into account are reported.

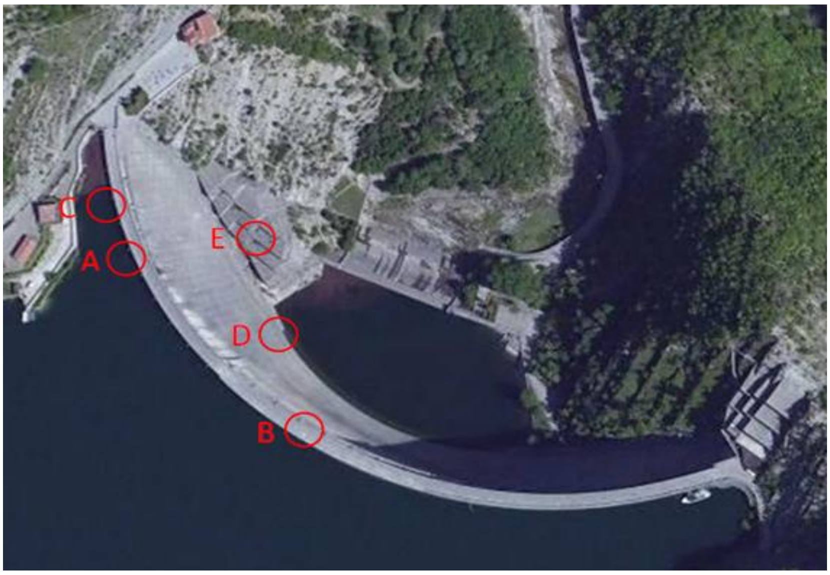

Figure 2.12. Analyzed specimens.

Table 2.6. Laser Scanner (points and mesh) and UAV (points) comparison.

Specimen	**Surface (m^2)**	**n° points Laser Scanner**	**n° points by UAV**	**Gap Laser Scanner Point Cloud – Laser Scanner mesh**		**Gap UAV Point Cloud – Laser Scanner mesh**	
				(A)	(B)	(C)	(D)
				Mean (m)	Stand. Dev. (m)	Mean (m)	Stand. Dev (m)
A	1186.2	3 906 276	2 569 690	0.0000	+0.0001	+0.0016	+0.0032
B	402.3	196 006	1 240 047	0.0000	+0.0001	-0.0322	+0.1171
C	9.5	70 048	65 306	0.0000	+0.0001	-0.0021	+0.0048
D	23.3	46 874	122 421	0.0000	+0.0001	-0.0116	+0.0162
E	263.8	2 260 559	611 289	0.0000	+0.0001	-0.0004	+0.0069

- Specimen A

The A specimen presents a particularly extended surface (1186.2 m^2) on the upstream face, Fig. 2.12, and with a prevalent vertical development, the average gap by the reference laser scanner mesh is 0.0016 m and the standard deviation is 0.0032m, Tab. 2.6 and Fig. 2.13.

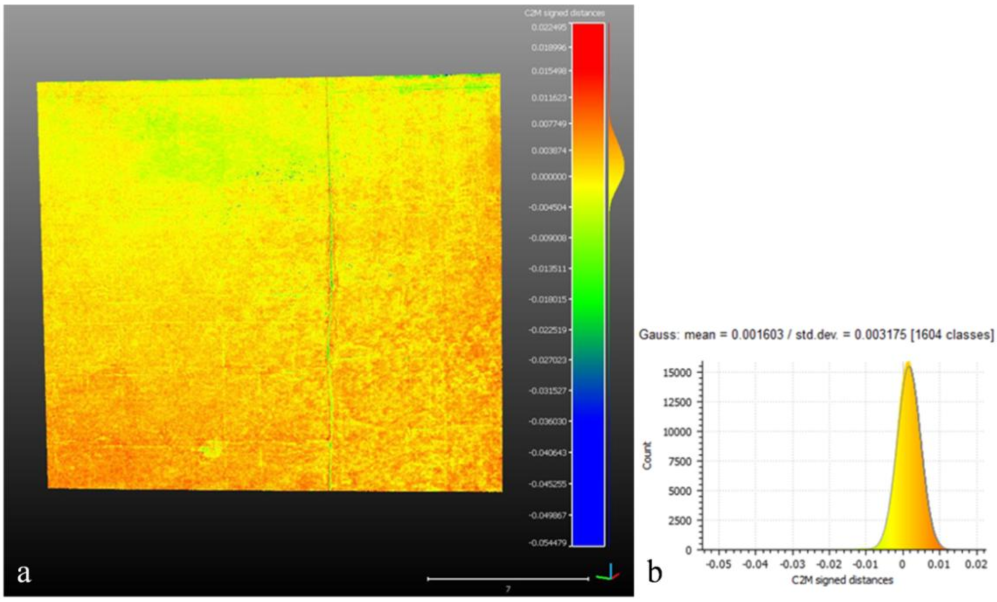

Figure 2.13. Specimen A. a) Difference map: Laser Scanner mesh – UAV Dense Point Cloud; b) Statistical Parameter.

- Specimen B

The B specimen presents a portion of the spillways light, Fig. 2.12. In this zone the deviation between Dense Point Cloud and the Laser Scanner mesh is slightly more evident, Fig. 2.14. The average gap is -0.0322m and the standard deviation is 0.1171m, Tab. 2.6. The points by UAV appear more disperse respect to that measured by Laser Scanner. The complex geometry analyzed determinates some grey zones that reduce the Laser Scanner acquire capability. Therefore the less of reference information compromises in part the comparison, in fact, in this case, the UAV information is more complete. Moreover the temperature and humidity conditions of the analyzed element could have conditioned the UAV acquisition. In view of all these factors the accuracy is slightly lower respect to the other considered portions although it is always inside the accuracy required range of the survey of this type of structures.

- Specimen C

The C specimen analyses a joint zone between adjacent ashlars of the structure on the upstream face, Fig. 2.14. The average gap and the standard deviation are respectively -0.0021m and 0.0048m, Tab. 2.6 and Fig. 2.15. This portion explains as the UAV survey has a lower accuracy in the acquiring elements with small dimensions and characterized by curvature change in

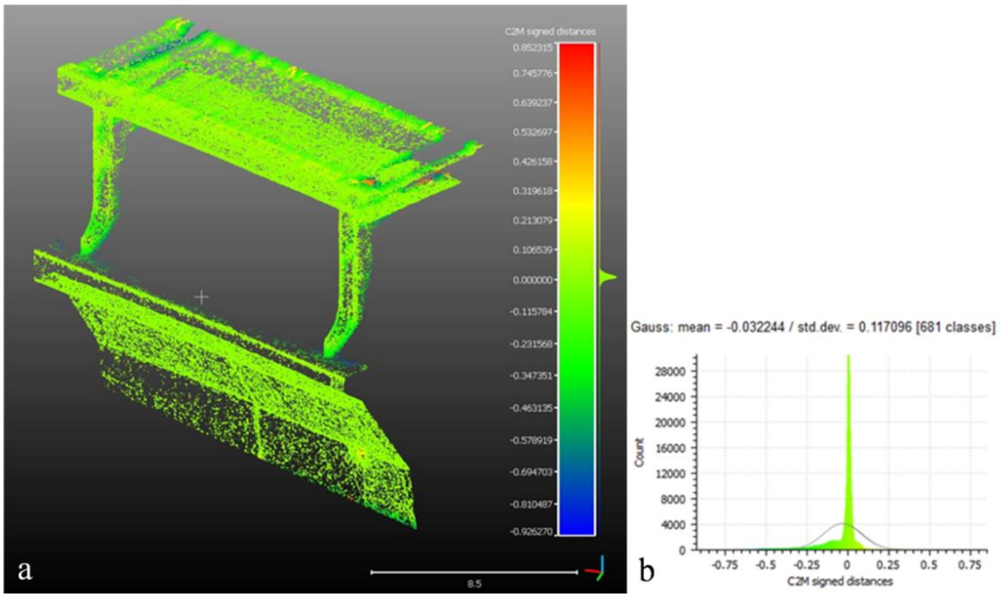

Figure 2.14. Specimen B. a) Difference map: Laser Scanner mesh – UAV Dense Point Cloud; b) Statistical Parameter.

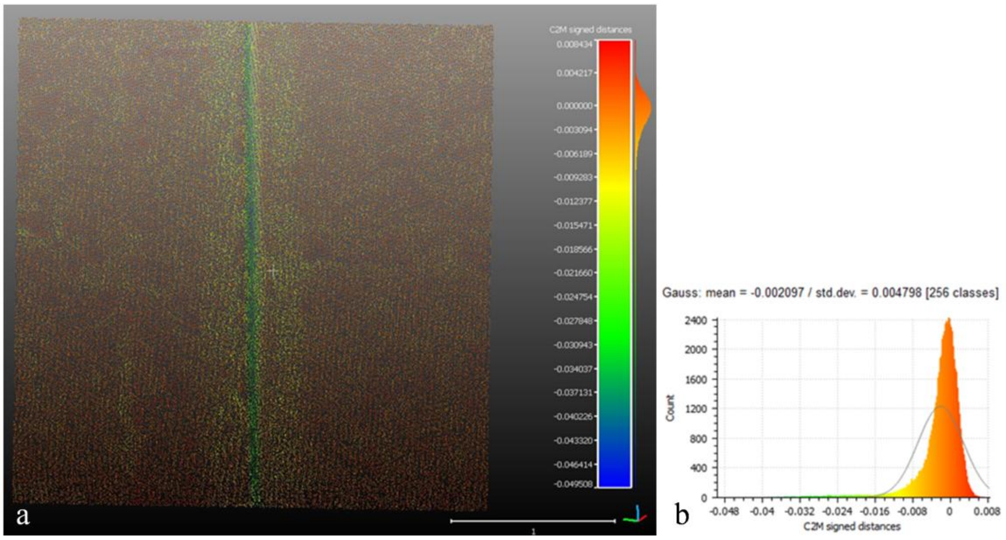

Figure 2.15. Specimen C. a) Difference map: Laser Scanner mesh – UAV Dense Point Cloud; b) Statistical Parameter.

reduced spaces. However these trends are available by the detail RGB information related to the points that, in this way, allows in every case the visual individuation of characteristic and structural important elements. The problem is related to the average density of the Dense Point Cloud, 1 point every 9cm^2, that does not allow the individuation of elements that have a variations lower than the dimension of the “grid” provided by UAV. The joints shape is in every case visible by the curvatures map, having an extension of 10 cm, other than perfectly identifiable by the RGB information of the points.

- Specimen D

The D specimen presents the analysis of the construction joint between pulvino foundation and dam body, Fig. 2.12. The average gap -0.0116m and the standard deviation 0.0162m are in line with the expected values although locally, near small asperity, they differ slightly, Fig. 2.16. Also in this case some gray zones (pulvino foundation horizontal surfaces) reduce the acquire capability of Laser Scanner.

- Specimen E

Finally the E specimen presents the analysis of a piece of the weight blocks in the left side, Fig. 2.12. The values of the average gap and standard deviation, respectively -0.004m and 0.0069m, in line with the expected values, attest that the UAV acquisition is performing also in the survey of ancillary works, Fig.

2.17. They are often portions missing of graphic drawings and therefore need of a geometry reconstruction close to reality.

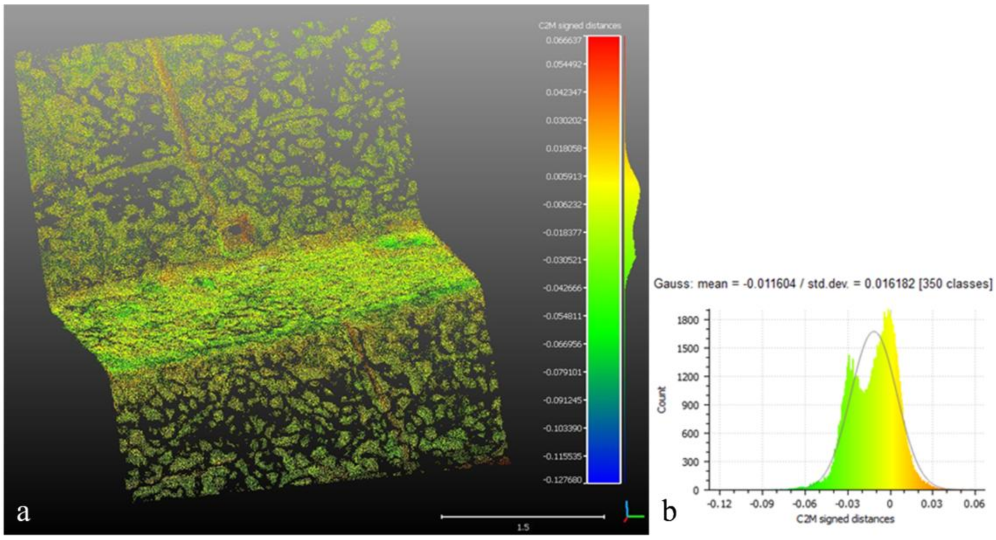

Figure 2.16. Specimen D. a) Difference map: Laser Scanner mesh – UAV Dense Point Cloud; b) Statistical Parameter.

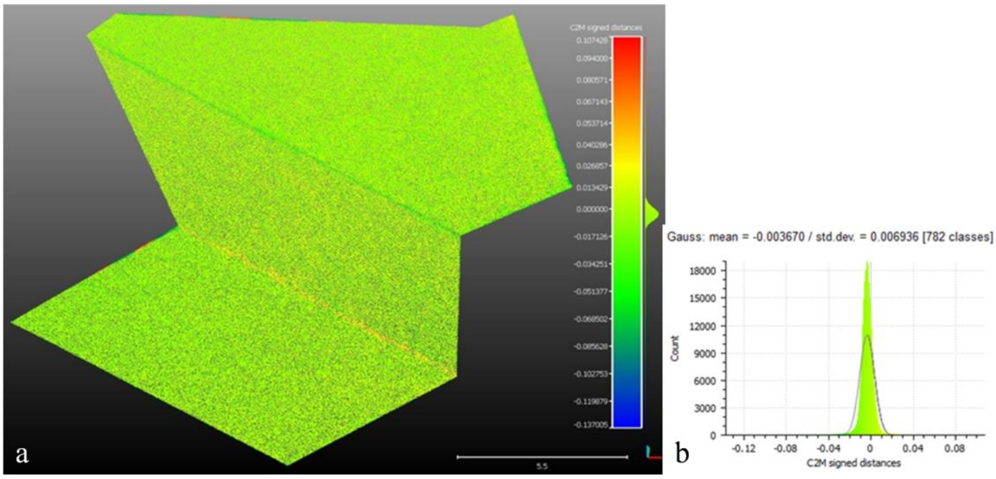

Figure 2.17. Specimen E. a) Difference map: Laser Scanner mesh – UAV Dense Point Cloud; b) Statistical Parameter.

2.6.5 UAV dense point cloud validation by technical drawings

The design geometry of the structure, understood as dam body and foundation, is available in the company archive in paper format, Fig. 2.18 a. It is the executive geometry because of, where the tracking is not close to the reality, have been included appendices and corrections, which are taken into account also in the data digitalization. By a manual procedure, the geometry is organized in Excel® worksheets, one for every altitude meter, therefore a total of 103 level/worksheets. In the standard worksheet for each arch are included: the altitude in meter above sea level, the z-coordinate, the coordinates of the curvature center of the upstream facing C_e, the coordinates of the curvature center of the innermost arch of the downstream facing C_1, the coordinates of the curvature center of the intermediate arch of the downstream facing C_2 (when it differs from C_1), the coordinates of the curvature center that describes the perimeter pulvino foundation C_3, the coordinates of the internal points *i* and of the external points *e* for each block for the median, the intermediate-medians and for the joints (in this case also an internal point is reported in order to model also the internal behaviour of the joint surface) and the coordinates of the points that describe the lateral foundation surface in contact with the rock abutments, Fig. 2.18 b and c.

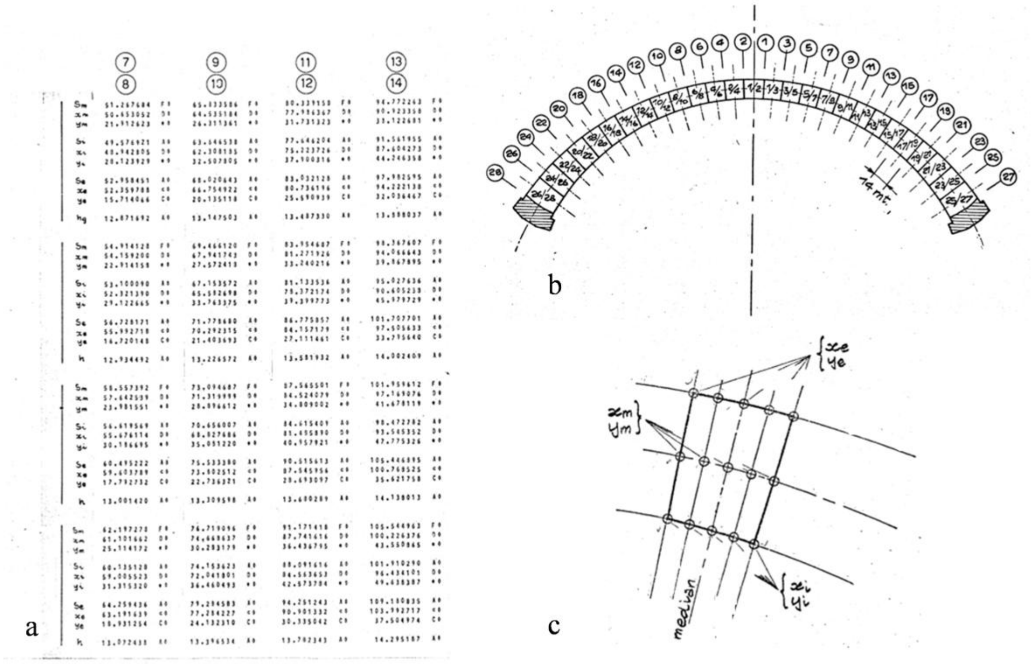

Figure 2.18. a) a paper of the design geometry of the dam; b) a scheme of the ashlars subdivision of the dam; c) characteristic points of the standard block.

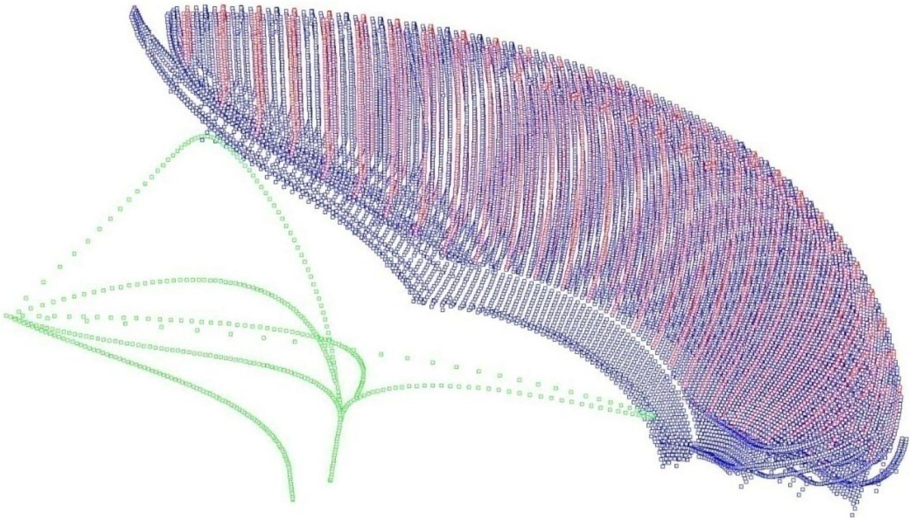

Figure 2.19. The design geometry of the structure in the Rhionceros® software, in red the points that describe the vertical joints, in blue the rest part of the points that describe the ashlars and the *pulvino* foundation and in green the curvature centers.

The coordinates of the points are in a reference system related to the tracking of the dam: it has the origin at the crown dam, 561m a.s.l., z-axis positive in the downward direction, x-axis along the right-left side direction, positive towards the left abutment, and y-axis along the upstream-downstream direction, positive toward the downstream direction. The structure is symmetric with respect the main section, where it is located also the origin, therefore with respect the y-axis with the exception of the points that describe the lateral foundation surface that differs between the right and left abutments. The .xlsx format worksheets have been saved in .txt format in order to be imported in the Rhinoceros® software, a pre-processing three-dimensional work environment, where the arches have been organized in subsequent order. Fig. 2.19 shows a visualization of the whole structure design geometry in the Rhino® space, in red the joints behaviour, in blue the rest of the point of the structure and in green the curvature centers, being a double curvature structure they moves along curves in the three-dimensional space.

In order to compare the design geometry with that extracted from the UAV dense point cloud and, as explained in §4.2, to employ the fist to integrate the second one, they must have the same coordinate system. Therefore, it is necessary a rigid 3D roto-traslation of the design geometry on the reference system of the UAV geometry, the Gauss-Boaga cartographic system. In the UAV dense point cloud, in the Gauss-Boaga reference system, the coordinates of the local origin, that corresponds to the one of the design geometry, is identified.

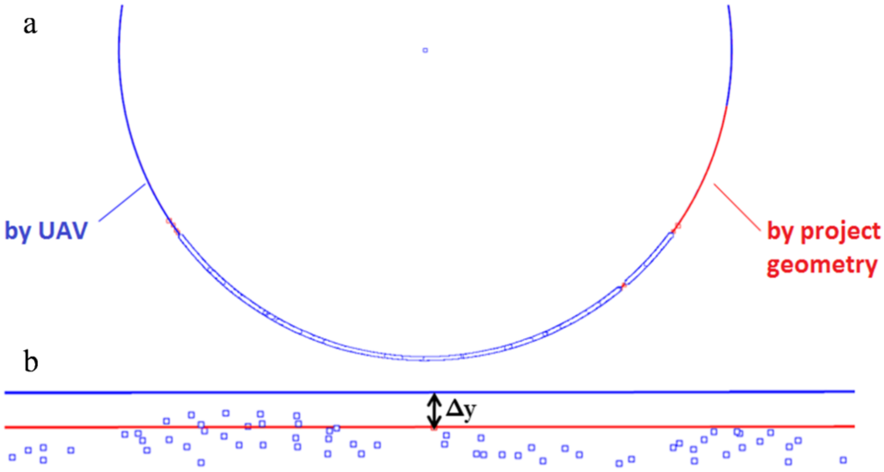

Figure 2.20. a) comparison of a circumference obtained by the interpolation of the UAV points, in blue, and, in red at the same level, the circumference derived from the project geometry; b) a zoom of the gap, Δy, between the two circumferences.

Starting from the curvature centers of downstream facing (central circumference C_{i1}) and of upstream facing (C_e) extracted from the UAV dense point cloud at the same level of the dam crowing (561m a.s.l.), the direction of the upstream-downstream y-axis is identified. From the curvature center C_e, along the y direction, a segment, with extension equal to the y-coordinate of the same point in the design geometry, is drawn. Therefore, being known the coordinates of the local origin and of the curvature center C_e at the level of the dam crowing in the UAV dense point cloud in the Gauss-Boaga reference system, a roto-tranlation of the design geometry on the aforementioned two points, known also in the same design geometry, is possible.

Adopted the same cartographic reference system, the design geometry and the UAV survey are the object of a double comparison in order to verify the conformity, although obvious, of the tracking geometry to the real one and, at the same time, to have a further validation of the accuracy on the UAV survey.

A first local comparison evaluates the gaps between the circumferences extracted from the design geometry and from the UAV point slices at the same altitude, Fig. 2.10. 14 arches close to the main section 1-2, that describe a part of the upstream facing, are taken into account. Indeed, the upstream facing is characterized by a unique arch and this is it the object of integration by the design geometry, as it will be further explained in the next chapter. Therefore the examination of this area is the most appropriate. Tab. 2.7 shows the gaps between the circumferences derived by the two representations, the medium gap is of 0.02m.

The second comparison, with a more global aim, deal with the reconstruction of the behaviours in the three-dimensional space of the construction points of the arches (centers) that describe the upstream facing. Fig. 2.21 shows in red the construction points, and the interpolation line, extracted by the project geometry and in blue those extracted by the interpolating circumferences of the points slices provided by the UAV survey. It can be noted an average gap between the two lines, reminding that they are theoretical not tracked construction points, of 0.14m. All the results, for each analyzed arch, are reported into the Tab. 2.8. The larger gap, between UAV and geometry points, of the latter comparison respect to the first one, is due to the fact that, in this case, theoretical points are compared; they do not describe a physical part of the structure but some centers of the circumferences of the upstream facing, therefore their reconstruction, starting from the UAV dense point cloud, is more complicated than a real detail of the structure.

Table 2.7. Gaps Δy between the 14 analyzed circumferences, one for each arch from 535 to 548m a.s.l., extracted by the UAV dense point cloud and the project geometry close to the main section 1-2 near the upstream facing. The average gap is around 0.02m.

m a.s.l.	**$\Delta y_{1\text{-}2}$ (m)**
548	+0.01
547	+0.05
546	+0.04
545	+0.06
544	+0.02
543	+0.00
542	+0.02
541	+0.02
540	+0.01
539	+0.00
538	+0.03
537	+0.01
536	+0.00
535	+0.02

Table 2.8. Gaps Δd between the construction points C_e (centers) for 14 arches from 535m a.s.l. to 548m a.s.l., extracted by the UAV dense point cloud and the project geometry close to the main section 1-2 near the upstream facing. The average gap is around 0.14m.

m a.s.l.	Δd_{Ce} (m)
548	+0.40
547	+0.41
546	+0.26
545	+0.22
544	+0.07
543	+0.11
542	+0.06
541	+0.04
540	+0.07
539	+0.13
538	+0.07
537	+0.06
536	+0.10
535	+0.02

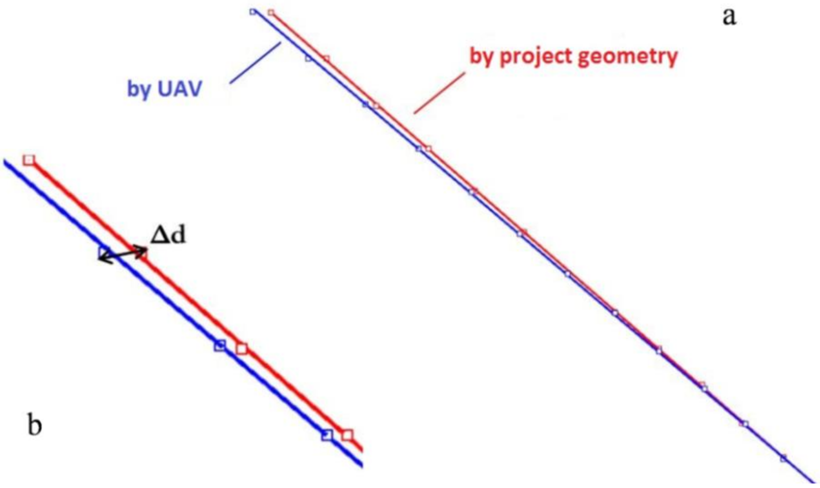

Figure 2.21. a) in red, the construction points, and the interpolation line, extracted by the project geometry and, in blue, those extracted by the interpolating circumferences of the point-slices provided by the UAV survey, the behaviour in the three-dimensional space is the same; b) a zoom of the gap, Δd, between the two interpolating lines.

2.7 Results

This section summarizes the results of the density, punctual, liner and surface analyses carried out on the UAV dense point cloud adopting the traditional topographic tools as reference and the comparison with the design project.

The evaluation of the spatial density on different specimens shows that the density of structure points is never less a point every 9cm^2 (a grid of 3X3cm in size). Higher densities, around a point every 1cm^2, are reached on the concrete structure on areas such as the upstream and downstream faces, the crowing and close to the saddle foundation, that are the focus of the survey procedure. Lower density values are reached near areas of vegetation, mostly on the left side, but they are not of interest for the inspection or the geometry reconstruction of the dam. The point density, evaluated by this analysis, is enough to reproduce, in the FEM model, the vertical joints elements, the smaller entities of interest. This type of analysis also shows the high uniformity of the UAV data. Therefore, thanks also to the RGB information associated to the points, it allows a detailed inspection of the concrete surface. An higher point density would be not necessary for modelling aspects because of the smaller entities of the structure are already identified by the current dense point cloud.

The validation by point consists in the evaluation of the distance between two sets of data: the reference markers acquired by Total Station (i.e. check points) and the same generated by the UAV dense point cloud. The gap of a few centimeters and the global uniformity of the UAV model are ensured by the average values and homogeneity of the standard deviations of the analyzed points along the three components. The validation by lines evaluates the distance between nine curves extracted respectively by the Laser Scanner model and by the UAV dense point cloud at the same level. The average value of the gap is 2cm, the maximum distance is evaluated near the higher level curves (558 m a.s.l.), where the geometry of the structure is very complex due to the presence of the lights of the spillways. Moreover in this area there is the combination of air updrafts, due to the temperature difference between the bottom and the top of the structure, and the air flowing from the spillways lights. Therefore the UAV was unable to fly, for safety reasons, close to the structure.

Finally, the validation by surfaces evaluates the distance between the mesh built on the laser scanner scans and the UAV dense point cloud. Also in this case, different specimens are taken into account. A uniform surface such as that of the downstream facing dam shows a mean value of the gap of 2.1cm. Other parts of the structure, such as those characterized by rapid curvature change in a small space such as joints and spillways lights, show higher distances. To reduce the gaps, some markers could be placed close to the curvature changes fixing the model exactly in its most critical points. However small variations in the geometry are in any case detectable by the RGB information associated with the UAV dense point cloud.

A further comparison analysis of the UAV dense point cloud has been performed adopting as reference the design project of the dam structure, available into the archive of the owners. The accordance between the design geometry and that extracted by the UAV survey confirms the dual validity of both representations. Indeed, the UAV survey confirms, although obvious, the accordance of the executive project of the dam to the reality and, at the same time, the accuracy of this new survey technique is validated into the inspection of large and vertical structures such as dams. As §4.2 will explain, the accordance between the two representations allows to employ the design project to integrate the missing part of the UAV survey such us the portion of the upstream facing under the water level or the foundation into the abutments where the drone was not able to shot frames.

As well as validate the innovative UAV technology, the present Chapter gives the opportunity to compare the latter with the traditional survey technique of large structures, the Laser Scanner. Although the surface areas acquired by the Laser Scanner is smaller than that acquired by the UAV technique, in general, the number of markers employed for the recording of the Laser Scanner scans, 53, is lower than that required for the UAV survey, 156. Therefore, the Laser Scanner technique requires a setup time lower than that required by the UAV technology. However, the recording time of the Laser Scanner scans, three days, mostly due to the change of the acquisition points, is greater than that required for the UAV flights, one day (19 flights lasting 15 min/flight). The post-processing time for the dense point clouds construction is comparable between the two technologies. However, it should be noted that the Laser Scanner cannot acquire, or it would be too complicate, some parts of the structure due to gray areas and/or to inaccessibility of some positions of the acquiring points. Therefore, the spillway profile, the dam crowing, the stilling basin and the upstream facing of the dam are not acquired by the Laser Scanner, instead they are perfectly reproduced by the UAV survey. The drone is able to fly very close to such details and, in some cases, it is the only technical solution which can be employed on this type of high structures.

2.8 Chapter bibliography

[1] Venturi S., Di Francesco S., Materazzi F., and Manciola P., "Unmanned aerial vehicles and Geographical Information System integrated analysis of vegetation in Trasimeno Lake, Italy," *Lakes & Reservoirs: Research & Management*, vol. 21, no. 1, pp. 5-19, Mar. 2016.

[2] Gonçalves J.A. and Henriques R., "UAV photogrammetry for topographic monitoring of coastal areas," *ISPRS Journal of Photogrammetry and Remote Sensing*, vol. 104, pp. 101-111, June 2015.

[3] Ouédraogo M. M., Degré A., Debouche C., and Lisein J., "The evaluation of unmanned aerial system-based photogrammetry and terrestrial laser scanning to generate DEMs of agricultural watersheds," *Geomorphology*, vol. 214, pp. 339-355, 2014.

[4] Mancini F. et al., "Using Unmanned Aerial Vehicles (UAV) for High-Resolution Reconstruction of Topography: The Structure from Motion Approach on Coastal Environments," *Remote Sensing*, vol. 5, no. 12, pp. 6880-6898, Dec. 2013.

[5] Achille C. et al., "UAV-Based Photogrammetry and Integrated Technologies for Architectural Applications—Methodological Strategies for the After-Quake Survey of Vertical Structures in Mantua (Italy)," *Sensors*, vol. 15, no. 7, pp. 15520-15539, June 2015.

[6] Hallermann N., Morgenthal G., and Rodehorst V., "Vision-based monitoring of heritage monuments: Unmanned Aerial Systems (UAS) for detailed inspection and high-accuracy survey of structures," in *WIT Transactions on The Built Environment*, vol. 153, 2015, pp. 621-632.

[7] Dominici D., Alicandro M., and Massimi V., "UAV photogrammetry in the post-earthquake scenario: case studies in L'Aquila," *Geomatics, Natural Hazards and Risk*, vol. 8, no. 1, pp. 87-103, Jan. 2017.

[8] Hallermann N., Morgenthal G., and Rodehorst V., "Unmanned Aerial Systems (UAS) – Survey and monitoring based on high - quality airborne photos", International Association for Bridge and Structural Engineering (IABSE) Conference, Geneva, 2015.

[9] Hallermann N. and Morgenthal G., "From Aerial Photography to 3-Dimensional Inspection of Bridges", IABSE CONFERENCE GUANGZHOU 2016.

[10] Gillins M. N., Gillins D. T., and Parrish C., "Cost-Effective Bridge Safety

Inspections Using Unmanned Aircraft Systems (UAS)," in *Geotechnical and Structural Engineering Congress 2016*, Reston, VA, 2016, pp. 1931-1940.

[11] Hallermann N., Morgenthal G., and Rodehorst V., "Vision-based deformation monitoring of large scale structures using Unmanned Aerial Systems," *IABSE Symposium Report*, vol. 102, no. 8, pp. 2852-2859, Sep. 2014.

[12] Naumann M., Geist M., Bill R., Niemeyer F., and Grenzdörffer G., "Accuracy comparison of digital surface models created by unmanned aerial systems imagery and terrestrial scanner", *SPRS - International Archives of the Photogrammetry, Remote Sensing and Spatial Information Sciences,* Volume XL-1/W2, pp. 4-6, Rostock, Germany, 2013.

[13] Ullman S., "The Interpretation of Structure from Motion," *Proceedings of the Royal Society of London B: Biological Sciences*, vol. 203, no. 1153, 1979.

[14] Irschara A., Zach C., Frahm J.-M., and Bischof H., "From structure-from-motion point clouds to fast location recognition," in *2009 IEEE Conference on Computer Vision and Pattern Recognition*, pp. 2599-2606, 2009.

[15] Turner D., Lucieer A., and Watson C., "An Automated Technique for Generating Georectified Mosaics from Ultra-High Resolution Unmanned Aerial Vehicle (UAV) Imagery, Based on Structure from Motion (SfM) Point Clouds," *Remote Sensing*, vol. 4, no. 12, pp. 1392-1410, May 2012.

[16] Teza G., Pesci A., and Ninfo A., "Morphological Analysis for Architectural Applications: Comparison between Laser Scanning and Structure-from-Motion Photogrammetry," *Journal of Surveying Engineering*, vol. 142, no. 3, p. 04016004, Aug. 2016.

[17] Püschel H., Sauerbier M., and Eisenbeiss H., "A 3D model of castle landenberg (CH) from combined photogrammetric processing of terrestrial and UAV-based images", *ISPRS - International Archives of the Photogrammetry, Remote Sensing and Spatial Information Sciences*, pp 96–98, Beijing, China, 2008.

[18] Bolognesi M., Furini A., Russo V., Pellegrinelli A., and Russo P., "Testing the low-cost RPAS potential in 3D cultural heritage recontruction" *ISPRS - International Archives of the Photogrammetry, Remote Sensing and Spatial Information Sciences*, vol. XL-5/W4, pp. 229-235, Feb. 2015.

[19] Bolognesi M., Furini A., Russo V., Pellegrinelli A., and Russo P., "Accuracy of cultural heritage 3D models by RPAS and terrestrial photogrammetry," *ISPRS - International Archives of the Photogrammetry, Remote Sensing and Spatial Information Sciences*, vol. XL-5, pp. 113-119, June 2014.

[20] Barry P. and Coakley R., "Field accuracy test of RPAS photogrammetry", *ISPRS - International Archives of the Photogrammetry, Remote Sensing and Spatial Information Sciences*, 2013, pp. 27-31.

[21] Tahar K. N., "An evaluation on different number of ground control points in unmanned aerial vehicle photogrammetric block" *ISPRS - International Archives of the Photogrammetry, Remote Sensing and Spatial Information Sciences*, vol. XL-2/W2, pp. 93-98, Aug. 2013.

[22] Skarlatos D., Procopiou E., Stavrou G., and Gregoriou M., "Accuracy assessment of minimum control points for UAV photography and georeferencing,", Proceedings of SPIE, vol. 8795, p. 879514, 2013.

[23] Wujanz D. et al., "Survey configuration for terrestrial laser scanning ", Allgemeine Vermessungsnachrichten (AVN), 6(2016), 2016, 158–169.

[24] Ridolfi E., Buffi G., Venturi S., and Manciola P., "Accuracy Analysis of a Dam Model from Drone Surveys," *Sensors*, vol. 17, no. 8, p. 1777, Aug. 2017.

3. State of the art: arch-gravity dams and finite element modelling procedures

A brief introduction to the theory and approaches of the numerical analysis of arch-gravity dams is here provided. The aim is to give the reader a general overview and the state-of-the-art of this multidisciplinary issue.

3.1 Review of structural dynamics for seismic analyses

This section aims to provide an introduction to the basic theoretical concepts of dynamic analysis. It aims be useful for understanding and solving structural dynamic problems. A more extensive review on this subject can be found in specific works such as Chopra, 2012 [1].

3.1.1 Single-Degree-of-Freedom systems

The simplest dynamic system is the mass-spring system, Fig. 3.1, having a single degree of freedom. It consists of a mass *m*, that can translate along only one direction with its origin in the rest position of the same system, and a spring *k* that produces a linear elastic restoring force.

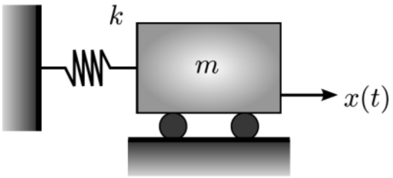

Figure 3.1. Scheme of the mass-spring system [2].

Taking into account a linear viscous device *c*, that produces a non-conservative force proportional to the velocity, and an external force *F(t)*, the equation of motion for the dynamic system illustrated in Fig. 3.2 can be written as,

$$m\ddot{x}(t)+c\dot{x}(t)+kx(t)=F(t), \tag{1}$$

It is a second-order linear differential equation with constant coefficients.

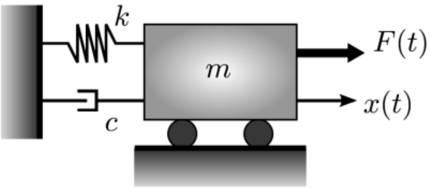

Figure 3.2. Scheme of the damped mass-spring system under external force [2].

Dividing all the terms by *m*, Eq.1 can be written as,

$$\ddot{x}(t)+2\zeta\omega_1\dot{x}(t)+\omega_1^2x(t)=\frac{F(t)}{m}, \tag{2}$$

where ω_1 is the natural circle frequency (generally called natural frequency as the subsequent *f*) of the system defined as,

$$\omega_1=\sqrt{\frac{k}{m}}, \tag{3}$$

and ζ is the damping factor defined as,

$$\zeta=\frac{c}{2m\omega_1}. \tag{4}$$

Other quantities of interest are the period *T* defined as the time required for one complete oscillation,

$$T_1=\frac{2\pi}{\omega_1}=2\pi\sqrt{\frac{m}{k}}, \tag{5}$$

and the natural frequency *f* defined as the number of complete oscillations that the system executes in the time unit,

$$f_1=\frac{1}{T_1}=\frac{\omega_1}{2\pi}=\frac{1}{2\pi}\sqrt{\frac{k}{m}}. \tag{6}$$

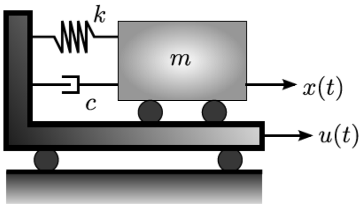

Figure 3.3. Scheme of the damped mass-spring system with impressed displacement [2].

3.1.2 Response to ground acceleration

Sometimes the external perturbation that acts on a system is not a force but a displacement applied at the base of the same system. The elastic restoring force provided by the spring *k* is proportional to the relative displacement $x(t)$ between the mass and the base (L-cart), Fig. 3.3. The viscous force provided by the damper is proportional to the relative velocity $\dot{x}(t)$ between the mass and the base (L-cart). Defined $u(t)$ as the impressed displacement at the base (L-cart), the absolute displacement of the mass *m* referred to the inertial system can be written as,

$$y(t) = x(t) + u(t)\,. \tag{7}$$

The equation of motion can be written as,

$$m\ddot{y}(t) + c\dot{x}(t) + kx(t) = 0\,, \tag{8}$$

and, adopting Eq. (7), Eq. (8) can be rewritten as,

$$m\ddot{x}(t) + c\dot{x}(t) + kx(t) = -m\ddot{u}(t)\,. \tag{9}$$

Dividing all terms of Eq. (9) by *m* and assuming the ground acceleration $-\ddot{u}(t) = \frac{F(t)}{m}$, Eq. (2) can be obtained again and the system can be treated as undergoing an external force.

3.1.3 Solution procedures

In this section, solution procedures of the second-order differential equation of an SDOF system subjected to an external force are taken into account [1,3].

- Classical solution, which is employed for free vibration and for vibrations that can be described analytically, such as harmonic or pulse forces. The solution is the sum of a complementary function, in which two constants of integration are included that can be derived from initial conditions, and a particular integral. The closed shape solution cannot be possible for an arbitrary external force that varies over time or for non-linear conditions.

- Duhamel's Integral (time-domain method), which is employed for forces that vary arbitrarily over time, such as the ground motion of earthquakes. If the forces are defined analytically, permitting an analytical evaluation of the integral, it is an alternative to the classical solution; otherwise numerical methods are required for its evaluation. This procedure, using the superposition principle of effects, can be applied only to a linear system. The perturbation can be treated as a series of infinitesimally short impulses, Fig. 4.3, and the solution, being valid the superposition principle of effects, can be written as,

$$x(t) = \int_0^t h(t-\tau)F(\tau)d\tau \,. \tag{10}$$

If the initial conditions are different from the natural ones (displacement and velocity are equal to zero), the free vibration solution has to be added to the previous one (10).

- Frequency-Domain solution, which can be applied only to a linear system. Laplace and Fourier transforms can be employed, the methods are similar. The solution is achieved substituting the main variable with another one by means of Fourier transform. The simpler equation obtained can be therefore solved and finally the real variable can be calculated by means of the inverse Fourier transform.

- Numerical methods of integration. The previous three solutions are restricted to linear systems and they cannot describe the inelastic behaviour of a structure.

Numerical procedures achieve the dynamic response of a system to any type of external forces that vary arbitrarily over time.

3.1.4 Multi-Degree-of-Freedom systems and modal analysis

The motion of a discrete linear elastic system can be described by a finite number of *n* lagrangian coordinates q_h, that, together with the time *t*, explain the original coordinates of the *i*-mass. The equation of motion for a MDOF system can be written, similarly to Eq. (1), as,

$$\sum_{j=1}^{n}\left(m_{hj}\,\ddot{q}_j + c_{hj}\,\dot{q}_j + k_{hj}\,q_j\right) = Q_h\,, \tag{11}$$

where Q_h is the *h*-generalized force. (11) can be written in matrix form as,

$$[M]\{\ddot{q}\}+[C]\{\dot{q}\}+[K]\{q\}=\{F\}. \tag{12}$$

Taking into account free vibration without damping, (11) becomes,

$$\sum_{j=1}^{n}\left(m_{hj}\,\ddot{q}_j + k_{hj}\,q_j\right) = 0\,, \tag{13}$$

and, looking for a solution that divides the time and the space contributions, the subsequent expression can be adopted,

$$q_j = u_j g(t)\,, \qquad \ddot{q}_j = u_j\,\ddot{g}(t) \tag{14}$$

where u_j are constant and *g(t)* is a function only of the time. Substituting (14) into (13),

$$\sum_{j=1}^{n}\left(m_{hj}u_j\,\ddot{g}(t) + k_{hj}u_j g(t)\right) = 0\,, \tag{15}$$

$$\ddot{g}(t)\sum_{j=1}^{n}\left(m_{hj}u_j\right) + g(t)\sum_{j=1}^{n}\left(k_{hj}u_j\right) = 0\,, \tag{16}$$

$$-\frac{\ddot{g}(t)}{g(t)} = \frac{\sum_{j=1}^{n}\left(m_{hj}u_j\right)}{\sum_{j=1}^{n}\left(k_{hj}u_j\right)} = \lambda\,, \tag{17}$$

therefore from the latter $\ddot{g}(t) = -\lambda g(t)$ and adopting it into (15) the subsequent equation can be obtained,

$$g(t)\sum_{j=1}^{n}\left(k_{hj} - \lambda m_{hj}\right)u_j = 0\,. \tag{18}$$

g(t) cannot be equal to zero therefore,

$$\sum_{j=1}^{n}\left(k_{hj} - \lambda m_{hj}\right)u_j = 0\,, \tag{19}$$

which in matrix form is,

$$\left([K] - \lambda[M]\right)\{u\} = \{0\}\,. \tag{20}$$

(19)/(20) is a linear homogeneous system of equations in u_j variables. To obtain solutions that are not banal, the determinant of the coefficients matrix has to be zero,

$$det\left([K] - \lambda[M]\right) = \{0\}\,. \tag{21}$$

(21) provides an *n*-degree algebraic equation in λ variable, called *characteristic equation*, of which *n* solutions are called *eigenvalues*. Substituting the generic λ value, λ_k, (19) or (20), the *k*-no banal solution $u_{k,j}$ can be obtained defined as *eigenvector*. These are also called *normal modes* of vibration.

The matrix that orders the *n* eigenvectors is called the *modal matrix* [X] and, similarly, the matrix that orders the *n* eigenvalues is called the *matrix of eigenvalues* [Λ]. Introducing a new set of coordinates $\{\varphi\}$, defined as *normal coordinates*, a linear transformation of the lagrangian coordinates can be performed by means of the modal matrix,

$$\{q\} = [X]\{\varphi\}\,. \tag{22}$$

By means of the coordinates transformation, (12) can be written as,

$$[M][X]\left\{\ddot{\varphi}\right\} + [C][X]\left\{\dot{\varphi}\right\} + [K][X]\{\varphi\} = \{F(t)\}\,. \tag{23}$$

Pre-multiplying each term by means of $[X]^T$, introducing $[A]=[X]^T[C][X]$, remembering that $[X]^T[M][X]=[I]$, where $[I]$ is the *identity matrix,* and that $[X]^T[K][X]=[\Lambda]$, (23) becomes,

$$\left\{\ddot{\varphi}\right\}+[A]\left\{\dot{\varphi}\right\}+[\Lambda]\{\varphi\}=[X]^T\{F(t)\}. \tag{24}$$

Having introduced damping and an external force, the system can be still decoupled if $[A]$ is diagonal. Writing $[A]$ as,

$$[A]=\begin{bmatrix} 2\zeta_1\omega_1 & 0 & 0 \\ 0 & \ddots & 0 \\ 0 & 0 & 2\zeta_n\omega_n \end{bmatrix}, \tag{25}$$

the diagonal condition can be ensured if,

- $[C]=\alpha[M]$, the damping matrix is proportional to the mass matrix and the damping ζ_k is inversely proportional to the natural circle frequency ω_k,

$$2\zeta_k\omega_k=\alpha\,, \qquad \zeta_k=\frac{\alpha}{2\omega_k}; \tag{26}$$

- $[C]=\beta[K]$, the damping matrix is proportional to the stiffness matrix and the damping ζ_k is directly proportional to the natural circle frequency ω_k.

$$2\zeta_k\omega_k=\beta\omega_k^2, \qquad \zeta_k=\frac{\beta\omega_k}{2}; \tag{27}$$

- $[C]=\alpha[M]+\beta[K]$, the damping matrix is a linear combination of the mass matrix and the stiffness matrix,

$$2\zeta_k\omega_k=\alpha+\beta\omega_k^2, \quad \zeta_k=\frac{\alpha}{2\omega_k}+\frac{\beta\omega_k}{2}. \tag{29}$$

In this case the damping formulation is called *Rayleigh damping formulation*. α is the Rayleigh damping coefficient that takes into account mass proportional damping (effective on lower frequencies) and β is the Rayleigh damping coefficient that takes into account stiffness proportional damping (effective on higher frequencies).

The determination of coefficients α and β can be performed imposing the same damping ratio for two modes $\zeta_i = \zeta_j = \overline{\zeta}$ and applying (29) twice,

$$\begin{cases} \zeta_i = \dfrac{\alpha}{2\omega_i} + \dfrac{\beta\omega_i}{2} \\ \zeta_j = \dfrac{\alpha}{2\omega_j} + \dfrac{\beta\omega_j}{2} \end{cases}, \tag{30}$$

$$\begin{cases} \alpha = \dfrac{2\omega_i\omega_j}{\omega_i + \omega_j}\overline{\zeta} \\ \beta = \dfrac{2}{\omega_i + \omega_j}\overline{\zeta} \end{cases}. \tag{31}$$

The two modes *i* and *j* have to be chosen to minimize the error of the damping on the all modes. Usually, the important modes, which should be taken into account, are the first, to which the majority of the significant mass of the system is associated.

3.1.5 Numerical methods of integration

As already underlined, the first three solution procedures of second-order differential equations presented in §3.1.3 cannot be employed in the resolution of structures with inelastic behaviour. Intense shaking due, for example, to earthquake motions could cause the inelastic behaviour of the structure. In this case and when, although the system response is still linear, the excitation is too complicated to be defined analytically, the numerical time-stepping methods are the most practical solution procedures [1].

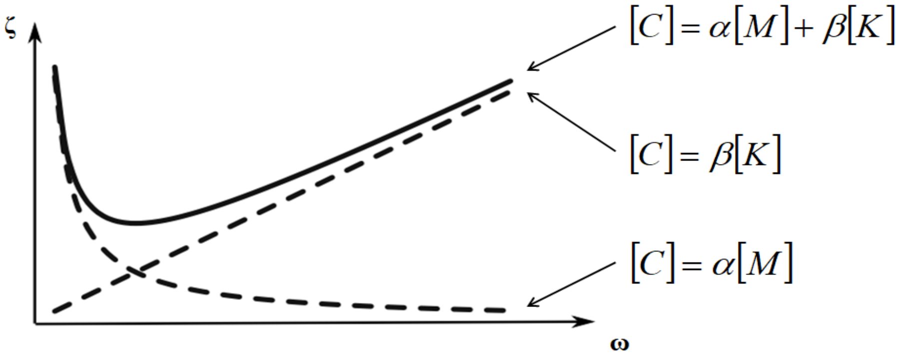

Figure 3.4. Damping ζ as a function of the natural circle frequency ω, for the three different definition of the damping matrix [C].

For an inelastic system Eq. (9) can be rewritten, including the internal resisting force f_s that is opposed to the displacement, as,

$$m\ddot{x}(t)+c\dot{x}(t)+f_s(x)=p(t) \quad or \quad -m\ddot{u}(t), \tag{32}$$

taking into account the initial conditions $x_0 = x(0)$ and $\dot{x}_0 = \dot{x}(0)$. Moreover, the applied forces $p(t)$ are defined as a set of discrete values $p_i=p(t_i)$, with $i=0,\dots,N$. The time interval $\Delta t=t_{i+1}-t_i$ is constant and the response of the system, in terms of displacement x_i, velocity $\dot{x}_i$ and acceleration $\ddot{x}_i$, at time i is known. All the subsequent procedures will allow us to determine the response of the system, in terms of displacement x_{i+1}, velocity $\dot{x}_{i+1}$ and acceleration $\ddot{x}_{i+1}$, at time $i+1$. The main three time-stepping procedures are:

- Methods based on interpolation of excitation. This formulation is valid only for a linear system and the response for MDOF can be achieved by superposition of modal responses. The procedure is based on the interpolation of excitation over each time interval, between time i and $i+1$; therefore the applied force at the generic time $t_i \leq \tau \leq t_{i+1}$ can be written as,

$$p(\tau)=p_i+\frac{\Delta p_i}{\Delta t}\tau \,. \tag{33}$$

Eq. (32) can be written as,

$$m\ddot{x}(t)+c\dot{x}(t)+f_s(x)=p_i+\frac{\Delta p_i}{\Delta t}\tau\,, \tag{34}$$

and it can be solved by the solution superposition of free vibration, response o step force p_i and response to ramp force $(\Delta p_i/\Delta t_i)\tau$. The limitation on the dimension of Δt is only related to its capacity to approximate the excitation in such a way as to not miss the peaks. This would mean missing the response peaks.

- Methods based on finite difference of expression of velocity and acceleration. These are backward, forward and central difference methods. These formulations are valid for solving both linear and nonlinear equations of motion. The central difference method is based on the approximation of the time derivates of displacement and their expressions, taking into account a constant time step $\Delta t_i = \Delta t$, are,

$$\dot{x}_i=\frac{x_{i+1}-x_{i-1}}{2\Delta t}\,,\qquad \ddot{x}_i=\frac{x_{i+1}-2x_i+x_{i-1}}{(\Delta t)^2}\,, \tag{35}$$

substituting the ratio of the increment of the function *x(t)* to its limit. Substituting Eqs. (35) into Eq. (32), the solution at time *i+1* can be achieved from the equilibrium condition at time *i* without using the equilibrium condition at time *i+1*. These types of methods are called *explicit*. An adequate value of Δt should be chosen to describe the acceleration ground motion, if it is not short enough the results can be meaningless. Typically, it is Δt=0.01s to Δt=0.02s.

- Methods based on assumed variation of acceleration. These procedures can solve linear and nonlinear equations of motion. The previous formulations, although they provide the response at the later time knowing only the situation at the earlier time, do not take into account the variation of resting force during the interval as accurately as these procedures [4]. A family of time stepping methods was developed by Newmark. It is based on the following equations in terms of acceleration at time *i+1*,

$$\dot{x}_{i+1}=\dot{x}_i+\left[(1-\theta)\Delta t\right]\ddot{x}_i+(\theta\Delta t)\ddot{x}_{i+1}\,, \tag{36}$$

$$x_{i+1}=x_i+(\Delta t)\dot{x}_i+\left[(0.5-\iota)(\Delta t)^2\right]\ddot{x}_i+\left[\iota(\Delta t)^2\right]\ddot{x}_{i+1}\,. \tag{37}$$

The two parameters θ and ι take into account how much of the acceleration at time *i+1* enters into the displacement and velocity relation at the time *i+1*. θ is assumed equal to ½, otherwise not real damping conditions would arise. ι parameter can be chosen $1/6 \leq \iota \leq 1/4$, which satisfies accuracy and convergence aspects. The time interval Δt should be taken as 1/5÷1/6 of the shorter natural period of vibration; in this way the rate of convergence will be adequate for all practical purposes [4].

3.1.6 Newmark's method

As previously mentioned, Newmark's method can be employed for solving both linear and nonlinear equations of motion. In the first case, Eqs. (36) and (37) can be modified in order to be solved without iteration.

In the case of non-linear systems, Eq. (32) includes the internal resisting force $(f_s)_{i+1}$ which is an implicit nonlinear function of the unknown response x_{i+1}, an iteration procedure is therefore required. Different iteration procedures are available. *i) Newton-Rapson* method. This is the most rapidly convergent process, due to its quadratic convergence, but it requires the computation and the inversion at each iteration of the Jacobian matrix or, in structural terms, of the stiffness matrix; *ii) modified Newton-Rapson* method. The stiffness matrix is calculated and inverted just once; therefore each iteration is faster but the convergence is linear and more iterations are required; *iii) quasi-Newton* or *incremental-secant* method. The stiffness matrix is calculated and inverted just at the first iteration, then, for the subsequent iterations the secant stiffness matrices are adopted rather than the tangential stiffness matrices. Finally the convergence velocity is intermediate between those of the two previous methods. To have a general idea of these iteration procedures, the Newton-Rapson standard method is reported below.

- Newton-Rapson iteration method

Taking into account a static analysis of an SDOF system, Eq. (32), neglecting the inertia and damping terms, becomes,

$$f_s(x) = p(t)\,. \tag{38}$$

The aim is to obtain, supposing that after j iterations the response $x^{(j)}$ is estimated, the response $x^{(j+1)}$. Then, the resisting force $f_s^{(j+1)}$ is expanded in the Taylor series. Supposing that $x^{(j)}$ is close to the solution, the increment

$$\Delta x^{(j)} = x^{(j+1)} + x^{(j)} \tag{39}$$

is small, and the second and higher order terms of the series can be neglected,

$$f_s^{(j+1)} = f_s^{(j)} + \left.\frac{\partial f_s}{\partial x}\right|_{x^{(j)}} \left(x^{(j+1)} - x^{(j)}\right) + \cdots \, . \tag{40}$$

Defining $k_T^{(j)} = \left.\frac{\partial f_s}{\partial x}\right|_{x^{(j)}}$ as the tangent stiffness at $x^{(j)}$, Eq. (40) can be rewritten as,

$$f_s^{(j+1)} \approx f_s^{(j)} + k_T^{(j)} \Delta x^{(j)} = p \, , \tag{41}$$

$$k_T^{(j)} \Delta x^{(j)} = p - f_s^{(j)} = R^{(j)} \, . \tag{42}$$

The solution of Eq. (42) gives $\Delta x^{(j)}$ and, by means of Eq. (39), a new estimate of the solution $x^{(j+1)}$ can be obtained. Looking at Fig. 3.5 a and b, not being an exact procedure, the resisting force $f_s^{(j)}$ is not equal to the external force p and the residual force $R^{(j)}$, defined by Eq. (42), allows for the evaluation of an additional displacement. This new estimate of the solution is used to find a new value of the residual force $R^{(j+1)}$ to which corresponds an additional displacement $\Delta x^{(j+1)}$ that can be employed to find a new value of the displacement,

$$x^{(j+2)} = x^{(j+1)} + \Delta x^{(j+1)} \, . \tag{43}$$

The process is continued until the convergence is achieved.

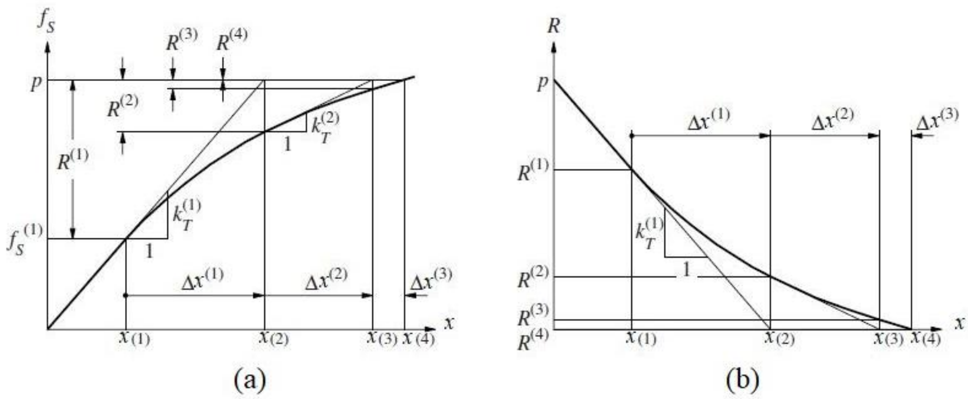

Figure 3.5. Newton-Rapson iteration: a) applied p and resisting f_s force, b) residual force.

The convergence criteria verify after each iteration whether some measures of the error in the solution are less than the specified fixed level in order to stop, if it happens, or to continue the procedure, if this does not happen. The measures in which the variation gap can be analyzed are different [1]. *Residual force* has to be less than a tolerance, $\left|R^{(j)}\right| \le \varepsilon_R$; *additional displacement* has to be less than a tolerance, $\left|\Delta x^{(j)}\right| \le \varepsilon_x$; *incremental work* done by the residual force through the additional displacement has to be less than a tolerance, $\frac{1}{2}\left|\Delta x^{(j)} R^{(j)}\right| \le \varepsilon_w$.

Once the Newton-Rapson iteration has been clarified, Newmark's method extends the procedure to dynamic equations, including in the resisting force $\hat{f}_s$ the inertia and damping terms,

$$\hat{f}_s(x) = m\ddot{x}(t) + c\dot{x}(t) + f_s(x)\,, \tag{44}$$

$$\hat{f}_s(x) = p(t)\,. \tag{45}$$

Eq. (45) has the same form as the static Eq. (38), therefore applying the previous procedure,

$$\hat{k}_T^{(j)} \Delta x^{(j)} = p - \hat{f}_s^{(j)} = \hat{R}^{(j)}\,, \tag{46}$$

the dynamic solution equation is similar to the static one. However there is an important difference, the inertia and the damping terms are included in both the tangent stiffness $\hat{k}_T$ and the residual force $\hat{R}$. Once the response x_{i+1} is achieved, the procedure can continue as for linear systems, as previously described, adapting the Eqs. (36) and (37).

3.2 Analytical solution of arch-gravity dam structures

Arch-gravity dams are structures that combine the arch and gravity effects. They are characterized by not-thin rings and therefore Mariotte's formula cannot be employed on them, even to a first approximation. This structural typology is adopted when the side offers good, but not exceptional, mechanical characteristics of the abutments. In this case, hydrostatic trust and, in general, all loads are partly absorbed by the abutments and partly by the rock foundation [5].

3.2.1 Conceptual design

The preliminary design of arch-gravity structures is based on Lamé's *thick cylinders* theory.

$$\sigma_R = -\frac{p_e R_e^2}{R_e^2 - R_i^2}\left(1 - \left(\frac{R_i}{R}\right)^2\right), \tag{47}$$

$$\sigma_\theta = -\frac{p_e R_e^2}{R_e^2 - R_i^2}\left(1 + \left(\frac{R_i}{R}\right)^2\right), \tag{48}$$

where,
R_e is the extrados radius (the larger one),
R_i is the intrados radius (the smaller one),
R is the current radius,
σ_R is the stress in the body dam on a unitary arch normal to the radial direction,
σ_θ, is the stress in the body dam on a unitary arch normal to the circumferential direction.

Due to the complexity of the problem, also the longitudinal stresses σ_L are significant; therefore Eqs. (47) and (48) can only be used for a preliminary evaluation.

The conceptual design of this type of structure can be achieved also by means of the load distribution between arches and cantilevers [6]. The analysis is appropriate for thin plates with reduced ratio between thickness and radius. This hypothesis could not be verified for the bottom part of the body dam, but it is nonetheless accepted. Assuming therefore the structure as a solid of revolution, closed, hollow and with variable thickness, Fig. 3.6 a, the differential equation for a generic slice, Fig. 3.6 b, of the tank is,

$$\frac{E}{12\left(1-\nu^2\right)}\frac{\partial^2}{\partial y^2}\left(s^3\frac{\partial^2 u}{\partial y^2}\right)+\frac{Es}{r^2}u=\gamma\left(y-y_s\right). \tag{49}$$

The solution of the problem is based on the integration of this fourth order equation in the radial displacement variable *u*, token positive in the direction of the vertical of the centers, of the master surface as a function of the deep *y*, Fig. 3.7. *r* is the constant value of the medium fibre, *s* is the generally variable thickness and ν is Poisson’s coefficient. The boundary conditions to integrate Eq. (49) for the crowning of the dam and for the base are,

$$\begin{cases} M=0 \quad T=0, & y=y_s \\ u=0 \quad \varphi=\dfrac{\partial u}{\partial y}=0, & y=y_b \end{cases}. \tag{50}$$

Assuming,

$$\lambda=\frac{y}{y_b}, \tag{51}$$

$$\vartheta=\frac{y_b^2}{s_b r}, \tag{52}$$

$$\lambda_s=\frac{y_s}{y_b}, \tag{53}$$

$$s=s_b\lambda^n, \tag{54}$$

$$s=cy^n, \tag{55}$$

$$\frac{p}{\gamma H}=\frac{p}{p_b}=\frac{\left(\lambda-\lambda_s\right)}{\left(1-\lambda_s\right)}, \tag{56}$$

$$\eta=\frac{Es_b}{\gamma H r^2}u, \tag{57}$$

Eq. (49) can be written as,

$$\frac{E}{12\left(1-\nu^2\right)}\frac{\partial^2}{\partial\lambda^2}\left(\lambda^{3n}\frac{\partial^2\eta}{\partial\lambda^2}\right)+\eta\lambda^n=\lambda-\lambda_s\,, \tag{58}$$

and the load acting on the arches and cantilevers can be simply obtained as,

$$\frac{p_a}{\gamma H}=\frac{p_a}{p_b}=\eta\lambda^n\,, \tag{59}$$

$$\frac{p_m}{\gamma H}=\frac{\lambda-\lambda_s}{1-\lambda_s}\eta\lambda^n\,. \tag{60}$$

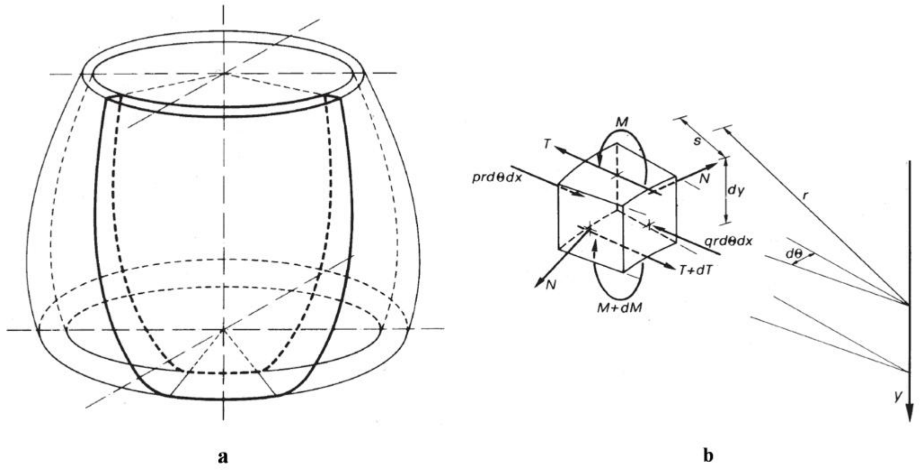

Figure 3.6. a) Solid of revolution; b) conventions.

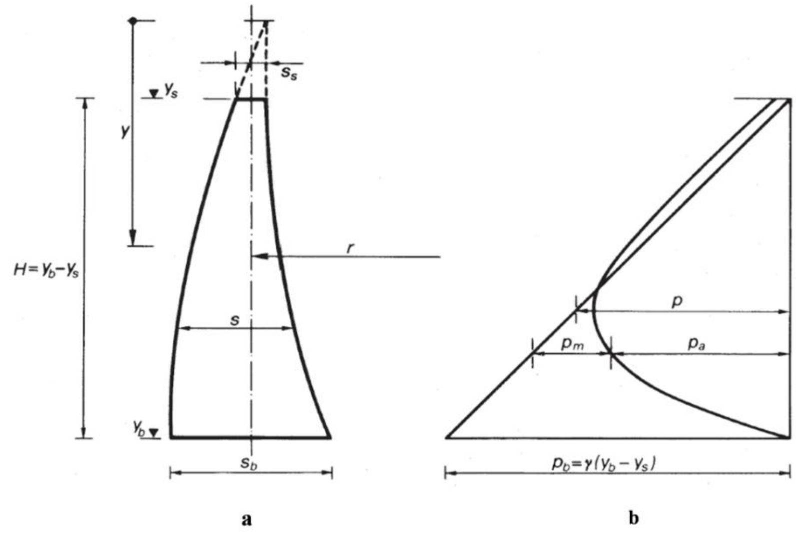

Figure 3.7. a) Main section; b) repartition of load between arch and cantilever system.

The part of the hydrostatic load acting on the arch p_a and referred to the one at the base p_b is $\frac{p_a}{p_b} = f\left(p / p_b; \lambda; \vartheta\right)$.

The repartition of the load as a function of the high of the dam and of the shape of the main section is reported in Figs. 3.8 a,b,c,d [6]. These diagrams can be employed for a first validation of the preliminary dimensions of the dam. The stresses σ_a (positive tractions) on the unitary arch can be evaluated by,

$$\sigma_a = -p_a \frac{r}{s}, \tag{61}$$

and the stresses acting on the cantilever of unitary thickness, on the intrados and extrados, can be evaluated by,

$$\sigma_m = \mp 6 \frac{M}{s^2}, \tag{62}$$

evaluating the momentum M due to the cantilever load $p_m = p - p_a$. Taking into account also the gravity load, it provides a normal force and a momentum that can be added, in terms of stresses, to the previous by means of presso-inflection formula. The obtained values can therefore be compared with the stresses limits. However, the general analysis of the static, and also dynamic, behaviour of the structure, also under other loads such as seismic motion, has to be performed by means of previously mentioned numerical methods.

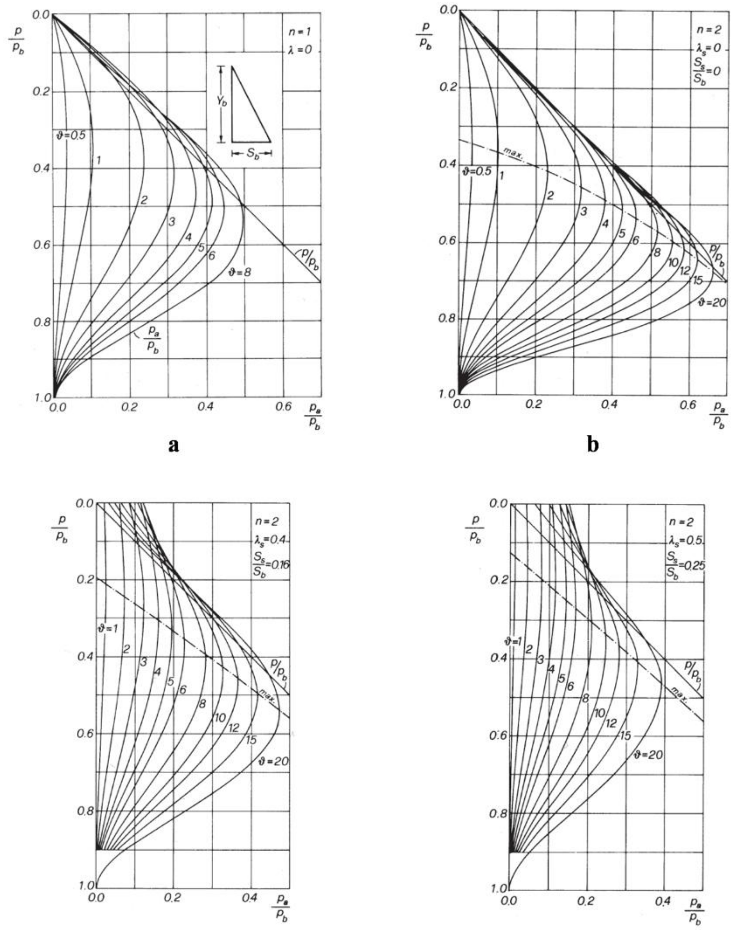

a b

c d

Figure 3.8. Repartition of the hydrostatic load between arch and cantilever system. a) n=1 and λ=0; b) n=2 and λ=0; c) n=2 and λ=0.4; d) n=2 and λ=0.5 [6].

3.3 Finite element modelling

The FEM – Finite Element Method – is a numerical procedure by which a structure, also with a very complex geometry, can be idealized as an assemblage of subdivisions (finite elements), connected at a discrete number of nodal points with a finite number of unknowns [7,8]. The displacement-based finite element method implies that these unknown variables are the displacements of the boundary nodal points of each element. The behaviour of the finite element can be described by a set of functions which represent displacements through the element region and on its contour in terms of element nodal displacements. The aforementioned functions satisfy the continuity condition between adjacent elements and therefore though the whole structure. Once the state of displacement is known, the strain state can be derived as a function of the former. By then imposing the initial strain state and the stress-strain relation of the material, the stress state is also determined. By means of the force equilibrium condition achieved between a system of equivalent nodal forces and any other distributed acting loads, the stiffness of each element can be derived. Finally, combining the elements in a manner that satisfies the equilibrium and compatibility conditions at the boundaries, the equilibrium equations for the entire system can be achieved. They are basically an algebraic equations system that can be solved by means of numerical methods, some of which are explained in §3.1.5.

3.3.1 General formulation

The previous explanation of the finite element method is here provided in mathematical form for a three-dimensional finite element. The solution in term of strain and stress states and element stiffness is achieved as a function of nodal point displacements of the finite element [7,8,9].

- Displacement function

Being a typical finite element *e* described by its nodes *i*, *j*, *m*, etc., the displacement at any point within the element can be approximated and expressed as a column vector,

$$\{u\}^e = \left[N_i^e, N_j^e, \ldots\right] \begin{Bmatrix} a_i \\ a_j \\ \vdots \end{Bmatrix}^e = \left[N^e\right]\{a\}^e , \tag{63}$$

where $\{a\}^e$ is the vector of nodal displacements of the *e* element and N_i^e , N_j^e , etc. are interpolation functions, called *shape functions,* which have to be chosen in such a way that, by inserting the coordinates of a node in Eq. (63), they give its correct displacement. These prescribed functions of position $\left[N_i^e\right]$ satisfy the conditions,

$$\left[N_i^e\left(x_i, y_i, z_i\right)\right] = [I], \tag{64}$$

$$\left[N_i^e\left(x_j, y_j, z_j\right)\right] = \left[N_i^e\left(x_k, y_k, z_k\right)\right] = [0], \tag{65}$$

where $[I]$ is the *identity matrix*. Eqs. (64) and (65) can be achieved simply by adopting suitable linear functions for x, y and z. If the displacement components are specified in the same manner, $[N_i^e]$ can be written as,

$$[N_i^e] = N_i^e [I]. \tag{66}$$

N_i^e can be obtained by Eq. (63) noting that $N_i^e = 1$ at x_i, y_i, z_i and $N_i^e = 0$ at any other vertices.

In general, the displacements within the whole system $\{u\}$ can be written in terms of the shape functions and the vector of nodal displacements as,

$$\{u\} = [N]\{a\}. \tag{67}$$

- Strains

When the displacement within the whole model is known, the strain state can be easily achieved similarly at any points by means of the relation,

$$\{\varepsilon\} = S\{u\}, \tag{68}$$

where *S* is a suitable linear operator. Using Eq. (63), Eq. (68) can be rewritten as,

$$\{\varepsilon\} = [B]\{a\}, \tag{69}$$

where,

$$[B] = S[N]. \tag{70}$$

S, and therefore $[B]$, can be obtained by combining Eq. (69) with the six strain components,

$$\{\varepsilon\} = \begin{Bmatrix} \varepsilon_x \\ \varepsilon_y \\ \varepsilon_z \\ \gamma_{xy} \\ \gamma_{yz} \\ \gamma_{zy} \end{Bmatrix} = \begin{Bmatrix} \dfrac{\partial u}{\partial x} \\ \dfrac{\partial v}{\partial y} \\ \dfrac{\partial w}{\partial z} \\ \dfrac{\partial u}{\partial y} + \dfrac{\partial v}{\partial x} \\ \dfrac{\partial v}{\partial z} + \dfrac{\partial w}{\partial y} \\ \dfrac{\partial w}{\partial x} + \dfrac{\partial u}{\partial z} \end{Bmatrix} . \tag{71}$$

- Stresses

The material within the whole system can be affected by initial strains ε_0 due to temperature changes, shrinkage, etc. therefore the stress state will be caused by the difference between the current and the initial strain state. In addition, an initial residual stress σ_0 can be included, accepting that it can be measured without the knowledge of the whole previous material's history. Assuming a general linear elastic behaviour, the stress-strain relationship can be write as,

$$\{\sigma\} = [D](\{\varepsilon\} - \{\varepsilon_0\}) + \{\sigma_0\}, \tag{72}$$

where $[D]$ is the elasticity matrix that contains the appropriate material properties, and can be arbitrary for each element, otherwise isotropic material properties are mostly used.

- Equilibrium equations

The solution of the displacement-based finite element method is the *principle of virtual displacements* (principle of virtual work). For any compatible small virtual displacements imposed on the body in its state of equilibrium, the total internal virtual work is equal to the total external virtual work, in matrix form, Internal virtual work External virtual work

$$\int_V \{\bar{\varepsilon}\}^T \{\sigma\} dV = \int_V \{\bar{a}\}^T \{f^B\} dV + \int_{S^f} \{\bar{a}^{S_f}\}^T \{f^S\} dS + \sum_i \{\bar{a}^i\}^T \{F^i\}, \qquad (73)$$

where $\{\bar{a}\}$ are the virtual displacements and $\{\bar{\varepsilon}\}$ are the corresponding strains (the over bar denotes virtual quantities). The external work is done by body forces $\{f^B\}$ (forces per unit volume) acting on the volume *V*, by surface forces $\{f^S\}$ (forces per unit surface area) acting on the surface area S_f and by concentrated loads $\{F^I\}$ (where *i* denotes the point of application). Substituting Eqs. (69) and (72) in the left-hand side of Eq. (73), the finite element stiffness matrix $[K]^e$ can be expressed as,

$$[K]^e = \int_{V^e} \left[[B]^T [D][B]\right]^e dV^e . \qquad (74)$$

Eq. (73) can be easily applied to the entire structure, approximating it as an assemblage of elements *e*, and rewriting the equation as a sum of integrations over the volume and area of all the finite elements of the whole structure,

$$\begin{aligned} \sum_e \int_V \left[\{\bar{\varepsilon}\}^T \{\sigma\} dV\right]^e &= \sum_e \int_V \left[\{\bar{a}\}^T \{f^B\} dV\right]^e \\ &\quad + \sum_e \int_{S^f} \left[\{\bar{a}^{S_f}\}^T \{f^S\}\right]^e \\ &\quad + \sum_i \{\bar{a}^i\}^T \{F^i\} \end{aligned} . \qquad (75)$$

Imposing unit virtual displacement $\{\bar{a}\}^T = 1$, the usual static equilibrium equation of the element assemblage can be obtained,

$$[K]\{a\} = \{F\}, \qquad (74)$$

where the load vector $\{F\}$ includes the effect of the body forces, surface forces, initial stresses and concentrated loads. The stiffness matrix $[K]$ of the complete structure can be written as,

$$[K]=\sum_{e}\int_{V^e}\left[[B]^T[D][B]\right]^e dV^e \,. \tag{75}$$

Including the effects of element inertia and damping forces as part of the body forces, the equilibrium equation of the whole structure in dynamic cases is given by Eq. (1). In practice, the damping parameters are not defined for the individual elements but the damping matrix $[C]$ is defined, as explained in detail in §3.1.4, as a combination of the mass and stiffness matrixes of the complete structure.

3.3.2 Isoparametric elements

Analysis of dams is generally carried out by means of finite elements belonging to the *isoparametric* family. The isoparametric finite element formulation states that the element coordinates and the element displacements are defined using the same (*iso*) parameters or interpolation functions, called shape functions [7,8,9]. The aspects that characterize a finite element are: the family, the DOFs – degrees of freedom –, the number of nodes, the formulation and the integration [10]. Fig. 3.9 shows the element families mostly used in a stress analysis. The family is strictly related to the element geometry on which the number of degrees of freedom depends. The DOFs are the unknowns of an analysis and they are evaluated on the nodes or by their interpolation at any other point. In a stress/displacement simulation, the degrees of freedom are translations and, for shell, pipe and beam elements, rotations; moreover, depending on the analysis type, the DOFs can be quantities of different fields. The interpolation order usually depends on the number of nodes of the element. There are elements with nodes only at their corners, which employ linear interpolation in each direction and are called *linear elements*, i.e. 8-node brick, Fig. 3.10 a; elements with mid-side nodes, in addition to those on the corners,

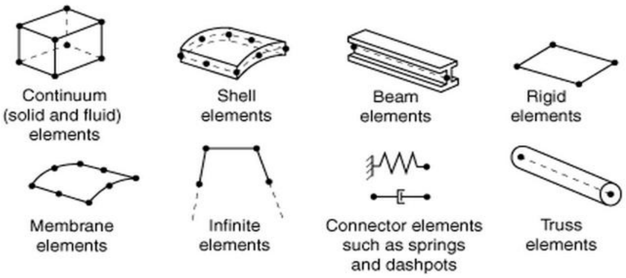

Fig. 3.9 Element families [10].

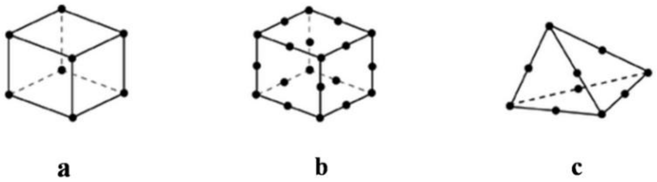

Fig. 3.10 a) linear element (i.e. 8-node brick); b) quadratic element (i.e. 20-node brick); c) second-order modified element (i.e. 10-node tetrahedron) [10].

which employ a quadratic interpolation and are usually called *quadratic elements*, i.e. 20-node brick, Fig. 3.10 b; triangular or tetrahedral elements with mid-side nodes, in addition to those on the corners, which employ a second-order modified interpolation and they are called *modified second-order elements*, i.e. 10-node tetrahedron Fig. 3.10 c. The formulation of an element refers to the mathematical theory used for its definition. Generally stress/displacement elements deform with the material (Lagrangian description) but other more complex formulations are available. Finally, the most common integration technique for integrating various quantities over the volume of each element is the Gaussian quadrature. In relation to the accuracy that would be achieved and to the admitted computational cost, *full* or *reduced* integration can be performed, considering a variable number of gauss points on which to obtain the material response. Three-dimensional solid elements are employed when the complexity of the geometry and/or of the applied loads are such as to not allow to take into account lower spatial dimension elements, Fig. 3.11. The *acoustic elements* that will later play a key role in water reservoir modeling also belong to three-dimensional solid elements.

3.4 Static analyses

The most common loads applied in static analyses of arch-gravity dams are the weight of the dam and the cause quantities, hydrostatic pressure of the impounded water and the temperature changes. Moreover, the contribution of less common loads can be included such as uplift, ice thrust or the weight of ancillary works when they are significant.

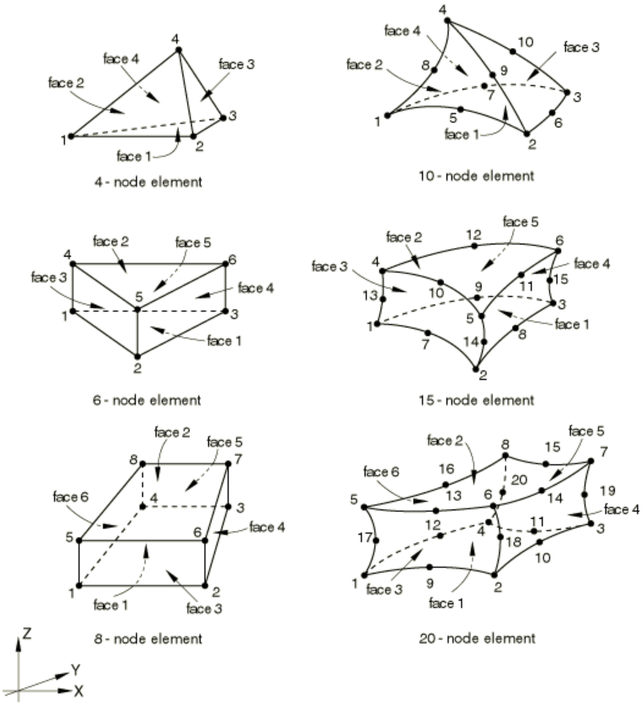

Fig. 3.11. Three-dimensional solid elements [10].

3.4.1 Gravity loads

The dead weight of the dam structure can be taken into account in the model as a uniform weight density throughout each element [8]. The gravity load can be applied by following the construction phases of the structure and then verifying the complete structure or directly on the latter. Gravity loads also affect ancillary works, such as spillways, weight blocks and dissipation basin, and the rock mass.

3.4.2 Hydrostatic loads

The impounded water of the reservoir acts as a hydrostatic pressure orthogonally to the upstream face of the dam. Moreover, if this has a slope, the pressure can be decoupled in vertical and horizontal components. Generally, for a gravity dam with a vertical upstream face, the expression of the pressure *p* acting normal to the surface varies linearly with the depth,

$$p = \gamma_w y \,, \tag{75}$$

where γ_w is the unit weight of the water ($\gamma=\rho_w g$, where ρ_w is the density and g is the acceleration due to gravity) and y is the depth. p assumes zero value at the free surface (y=0) and maximum value $p=\gamma_w H$ at the base of the dam, where H is the maximum height of the structure (or the maximum regulation height) (y=H).

ABAQUS®, in linear elastic static analysis, gives the possibility to simulate such distribution on a selected surface.

Abaqus/CAE usage: Load module, Load, Create, Mechanical from the Category box, Pressure from Type box, select the surface into the model, Hydrostatic from the drop-down menu, specify the Magnitude (M=γH where H is, for example, the maximum water height adopting as reference the base of the generic wall), specify the Zero Pressure Height (in a 3D space, this is the z-coordinate at which the pressure is zero – free surface), specify the Reference Pressure Height (in a 3D space, this is the z-coordinate at which the pressure is the previously specified Magnitude, for example, if the origin of the coordinate system is at the base of the generic wall, the z-coordinate, therefore the reference, would be zero).

3.4.3 Temperature loads

The thermal load plays a key role in arch and arch-gravity dam simulations, especially when the structures operate under severe temperature variations. It should be taken into account daily and seasonal thermal variations by means of air, water and concrete thermometers. In general, the temperature variation throughout the concrete structure varies in a nonlinear manner but it can be approximate by means of uniform and linear variations.

Abaqus/CAE usage: Load module, Predefined Field, Create, Other from the Category box, Temperature from the Type box, select the element set into the model, select the Distribution type and the Magnitude.

3.4.4 Uplift pressures

The uplift and pore pressures acts in the interstitial spaces of the dam body and of the foundation joints. Without drains the distribution of uplift pressure in a gravity dam is linear between the upstream and downstream pressures; the drains act by modifying the uplift distribution in a bilinear law therefore reducing their effect. The uplift pressures decrease the normal compressive stresses along a horizontal direction within the dam, increasing the tensile state. The uplift presence can be negligible in thin arch-gravity dams but it could be important in thicker structures. Uplift effect is generally not incorporated into the analysis because of the minor stress changes it produces and the lack of accuracy in the definition of the magnitude and distribution of uplift pressure.

3.4.5 Ice loads

When the dam structure is located in climates where thick ice can occur in the water reservoir, its effect should be taken into account in the analysis. Ice pressure can be represented by a distributed surface load or by equivalent concentrated forces applied at specific nodal points.

3.5 Earthquake dynamic analysis

Many dams in the World are located in seismic areas, and Italy is among them. Moreover, it is noted that many retaining structures have been built across known active faults [11]. Accurate seismic analyses have to be performed on existing dams so that a better understanding of the current state of the structures and of their supposed behaviour under severe seismic actions is achieved [12]. The response of a dam subjected to an earthquake motion is strictly related to its dynamic interactions with the deformable rock mass and the impounded water of the reservoir. Other factors related to the construction of the dam body, such as vertical joints, also play a key role in the dynamic behaviour of arch-gravity dams.

3.5.1 Fluid-structure interaction

Under a severe seismic event, not only the dam structure undergoes vibrations but also the water impounded in the reservoir. The hydrodynamic effect, in addition to the hydrostatic one, of the water mass on the dam produces a reduction of the natural frequencies of the structure, counteracting the motion due to the earthquake, and a dynamic variation in the pressure distribution acting on the upstream face due to the propagation of pressure waves [13]. Depending on whether and how the hydrodynamic effect is included into the analysis, the stresses in a dam can vary significantly. Therefore, during seismic analysis the FSI – Fluid Structure Interaction – has to be taken into account.

Several methods have been proposed to solve the problem; the procedures can be classified as functions of the employed method, *fluid-dynamic approach* (CDF) and *acoustic approach* [14].

- The fluid-dynamic approach is based on the *Navier-Stokes equations*. They describe the motion of a fluid undergoing a continuous flow, interesting all the fluid particles; the general state of motion can be described by,

$$\rho_f \left(\boldsymbol{F} - \frac{d\dot{\boldsymbol{u}}^f}{dt} \right) = \nabla p - \mu_f \nabla^2 \dot{\boldsymbol{u}}^f \, , \tag{76}$$

being valid the continuity equation, with constant density of the fluid,

$$\nabla \cdot \dot{\boldsymbol{u}}^f = 0 \, . \tag{77}$$

Remembering that, $\boldsymbol{F}$ is the vector of the body forces, $\dot{\boldsymbol{u}}^f$ is the vector of the fluid velocity, p is the pressure, ρ_f is the fluid density and μ_f is the viscosity. These equations are based on the hypothesis of: *real fluid*, with finite values of viscosity and compressibility and *Newtonian fluid* where the tangential stresses are related to the gradient of the velocity in the normal direction to the solid wall, proportional to the viscosity μ_f. This approach allows solving the state of motion of every Newtonian real fluid in every motion condition.

- The acoustic approach, neglecting the fluid viscosity, can be applied only to compressible real fluids or to incompressible ideal fluid, but investigating only motion state in which the fluid stays in quiet state, while the particles oscillate around an equilibrium position, transmitting to each other a certain quantity of motion. Therefore, under the hypothesis of absence of viscosity ($\mu_f=0$) and small oscillations, which means also small pressure variations and therefore small density variation due to the compressibility of the fluid, the *D'Alambert wave equation* for velocity potential is,

$$\nabla^2 \Phi - \frac{1}{c_f^2} \frac{\partial^2 \Phi}{\partial t^2} = 0 \, , \tag{78}$$

which is identical to the wave equation for pressure,

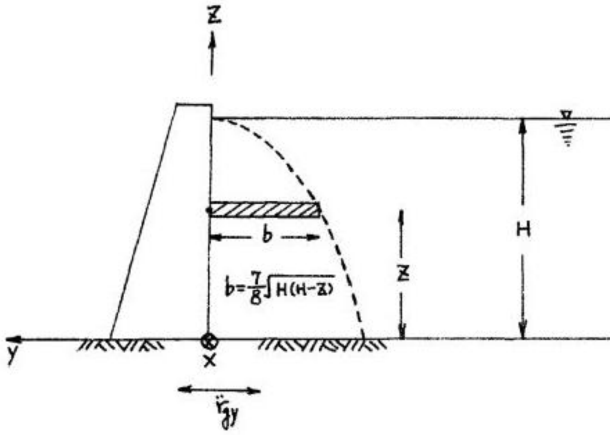

Fig. 3.12 Westrergaard classic hydrodynamic pressure distribution [16].

$$\nabla^2 p - \frac{1}{c_f^2}\frac{\partial^2 p}{\partial t^2} = 0 \, . \tag{79}$$

Φ is the velocity potential defined as $\dot{u}_i^f = \frac{\partial \Phi}{\partial x_i}$, where $\dot{u}_i^f$ is the scalar component of the velocity, and c_f is the speed of sound in the fluid defined as $c_f = \sqrt{\frac{K_f}{\rho_f}}$, where K_f is the bulk modulus of the fluid.

In the field of the acoustic approach, simplified added mass techniques have been developed and used for problems involving small displacement and small deformation of structure coupled to potential flow [15]. The aim of the simplified method is to investigate the dynamic behaviour of structures without coupling the fluid motion and reduce the number of degrees of freedom of the problem, saving computational time [15]. The principle at the base of these methods is the attachment of mass points on the structure in order to change its dynamic properties; the fluid-dynamic field is therefore excluded from the problem, which is reduced to the structural domain. Some of the simplified methods are reported below.

Added mass classical Westergaard formula (1933). This procedure evaluates the hydrodynamic pressure on the vertical upstream face of a 2-D rigid structure of a dam undergoing seismic motion along the upstream-downstream direction $\ddot{r}_{gy}$ [16]. Supposing an infinite reservoir in the upstream direction and ignoring

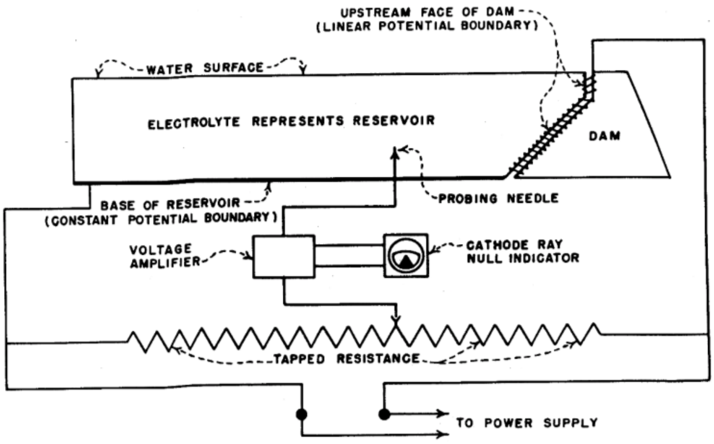

Fig. 3.13 Zangar electric system [17].

the surface waves, the hydrodynamic pressure at z height from the base of the dam is derived from the dynamic equilibrium equations of an infinitesimal volume in the Eulerian system,

$$p_z = \frac{7}{8}\rho_f \ddot{r}_{gy}\sqrt{H(H-z)}, \tag{80}$$

where H is the maximum water height and z is the current height, Fig. 3.12. Physically the hydrodynamic pressure effect is equal to the inertia forces of a certain portion of water close to the dam, with a parabolic shape, imagining as fixed all the rest part of the basin.

Added mass Zangar formulation (1952). Zangar introduces the simplifying hypothesis of incompressible fluid and therefore obtains the Laplace equations by adopting a velocity potential [17]. The hydrodynamic pressure on a varying slope upstream face of a rigid dam, undergoing an earthquake motion along the upstream-downstream direction, can be obtained experimentally by an electrical analogue, Fig. 3.13. The method evaluates the electricity filed into an electrolyte that simulates the basin, evaluating the equipotential lines, orthogonal to the electric field lines, which can be associated to the hydrodynamic pressure acting on the upstream face of the model.

Chopra formulation (1967). Following on from previous works, this method introduces the foundation soil, the deformability of the dam and takes into account the seismic motion with a generic formulation [18]. The hydrodynamic pressures are evaluated as the total of those obtained by the solution of two

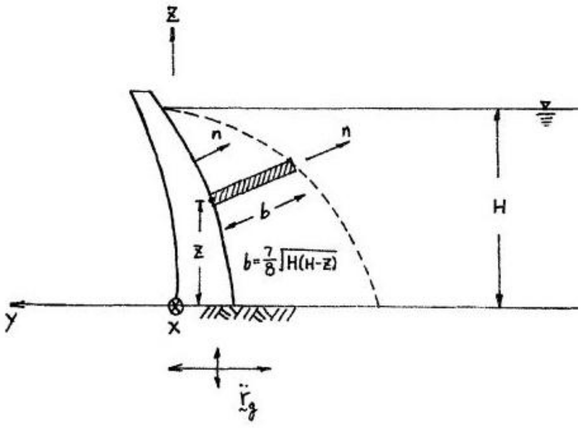

Fig. 3.14 Generalized Westergaard hydrodynamic pressure distribution [16].

different systems: the first considers a rigid dam and the hydrodynamic pressures are generated by the displacements due to the seismic motion; in the second system the hydrodynamic pressures are due to the displacement field related to the first mode of the structure. This procedure is not completely reliable because it does not take into account the relation in terms of frequency between structure and seismic motion and it does not consider the structure-water interaction. Further studies are those of Chopra, 1978 [19], and of Fenves and Chopra, 1985 [20].

Generalized Westergaard formula by Kuo (1982). The hydrodynamic pressure is calculated by the same parabolic distribution used in the classical Westergaard formulation but the Kuo's formulation can be applied also for arch dams with an upstream face curved in one or two directions [16], Fig. 3.14.

3.5.2 Acoustic elements and boundary conditions

The acoustic approach, as well as in simplified methods, is adopted for simulated hydrodynamic pressures also in numerical modelling. This section better describes Eq. (79), presented in §3.5.1, and it specifies the physical boundary conditions in acoustic analysis useful to describe the FSI – Fuild Structure Interaction – problem for dam-reservoirs.

As already mentioned in the previous chapter, the acoustic approach can be employed under the hypothesis of small oscillations and inviscid fluid therefore in seismic analysis of dam systems, where the pressure waves in the reservoir are of main interest and the fluid flow is negligible, the acoustic equations can be employed to describe the fluid dynamic of the problem. All the section is consistent with ABAQUS® documentation, a finite element method software [10]. Neglecting the body forces, the equilibrium equation for small motions and for a compressible fluid can be written in one dimension (*x*) as,

$$\frac{\partial p}{\partial x}+\rho_f\ddot{\boldsymbol{u}}^{\boldsymbol{f}}=0\,, \tag{81}$$

where $\ddot{\boldsymbol{u}}^{\boldsymbol{f}}$ is the vector of fluid acceleration and x is the spatial position of the fluid particle. The constitutive behaviour of an inviscid, linear and compressible fluid is described by,

$$p=-K_f\frac{\partial}{\partial x}\cdot\boldsymbol{u}^{\boldsymbol{f}}\,, \tag{82}$$

where $\boldsymbol{u}^{\boldsymbol{f}}$ is the vector of fluid displacement. Dividing Eq. (81) by ρ_f and combining it with the time derivatives of Eq. (82), the equation of motion in term of the fluid pressure is,

$$\frac{1}{K_f}\frac{\partial^2 p}{\partial t^2}-\frac{\partial}{\partial x}\left(\frac{1}{\rho_f}\frac{\partial p}{\partial x}\right)=0\,, \tag{83}$$

which is Eq. (79) for the x-direction.

The ABAQUS® library includes a set of elements for modelling a fluid medium undergoing small pressure variations, the acoustic elements. In small-displacement linear perturbation analysis, they model an acoustic medium as an elastic material in which the stress is purely hydrostatic (no shear stress) and the pressure is proportional to the volumetric strain. The acoustic field is strictly dependent on the boundary conditions assigned to the acoustic medium, therefore some conditions to simulate the dam-foundation-reservoir interaction will be explained below. The boundary conditions can be applied on the fluid medium contour as a boundary traction *T(x)*,

$$T(x)=\boldsymbol{n}\cdot\ddot{\boldsymbol{u}}^{\boldsymbol{f}}\,, \tag{84}$$

where n is the normal vector to the boundary. It is equal to the inward acceleration of the particles of the acoustic medium [10,13].

- Prescribed pressure. Imposing a fixed value of pressure p on a surface means imposing $\partial p = 0$, an alternative is to impose a normal derivative of the pressure,

$$T(x) = T_0 \,. \tag{85}$$

Prescribing a nonzero value represents a sound source to model for instance an acoustic source; whereas imposing a zero value means a rigid immobile boundary for instance a “free surface”.

Abaqus/CAE usage: Load module, Boundary Conditions – BC –, Create, Other from Category box, Acoustic Pressure from Types box, select the region into the model, assign the Magnitude of the pressure (zero for a “free surface”).

- Acoustic-structural coupling

The motion of an acoustic medium can be strictly coupled with that of a solid media, enforcing the condition,

$$\boldsymbol{n}^{-} \cdot \boldsymbol{u}^{f} = \boldsymbol{n}^{-} \cdot \boldsymbol{u}^{s} \,, \tag{86}$$

where $\boldsymbol{u}^{s}$ is the vector of solid (or structure) displacement. Eq. (86) defines the normal behaviour only, while the tangential one in uncoupled. The acoustic boundary traction can be written as,

$$T(x) = \boldsymbol{n}^{-} \cdot \ddot{\boldsymbol{u}}^{s} \,, \tag{87}$$

where $\ddot{\boldsymbol{u}}^{s}$ is the vector of the solid (or structure) acceleration.

This condition can be implemented either by introducing acoustic-structural interface elements or by defining a surface-based procedure. Adopting the latter method, which implies low computational costs, the tractions and volumetric acceleration fluxes are computed between structural and acoustic media. In place of distributed quantities, one side (“slave” surface) receives tractions/fluxes based on interpolation with the shape functions from the other side (“master” surface). Since the physical degrees of freedom of the fluid and the solid representation are different, two cases can occur. Solid master and fluid slave: designing the fluid surface as slave constraint values at each fluid node to assume an average of the values at close master surface nodes; displacement degrees of freedom are added to the fluid slave surface being constrained by the master displacements and therefore eliminated, instead of the slave pressures not being constrained directly. Non-physical coupled degrees of freedom are the displacements of the acoustic medium that “follow” the solid one in the motion. Fluid master and solid slave: designing the solid surface as slave constrains its values to be equal to interpolated values on the fluid master surface. Again, the coupling condition is enforced at the slave nodes, adding acoustic pressure degrees of freedom to the solid slave surface that are therefore eliminated, while the slave displacements are not constrained directly. Non-physical coupled degrees of freedom are the acoustic pressures distribution on the solid medium due to the effect of the acoustic one.

The acoustic-solid coupling is useful for modelling the reservoir-dam interaction or the reservoir-basin surface interaction when there are no bottom absorption phenomena.

Abaqus/CAE usage: Interaction module, Constraint, Create, Tie from the Types box, choose the Master surface from the model, choose the Slave surface from the model, accept or modify the options of the Edit Constraint.

- Acoustic-structural coupling with impedance and radiation

This is an acoustic-solid interaction where the displacements are linearly coupled but not necessarily the same due to the presence of a reactive layer that acts as a spring and a dashpot in series distributed between the two media. This layer introduces an impedance condition that relates the relative velocity between the acoustic medium and the solid one to the acoustic pressure *p* by acting on the fluid-structural interface and its rate of change,

$$\boldsymbol{n}^{-} \cdot \left(\dot{\boldsymbol{u}}^{s} - \dot{\boldsymbol{u}}^{f} \right) = \frac{1}{k} \dot{p} + \frac{1}{c} p \,, \tag{88}$$

where *k* and *c* are the spring and dashpot parameters respectively associated to the boundary. The traction term can be expressed as,

$$T(x) = \boldsymbol{n}^{-} \cdot \left(\ddot{\boldsymbol{u}}^{s}\right) - \frac{1}{c}\dot{p} - \frac{1}{k}\ddot{p} \,. \tag{89}$$

In some cases the acoustic medium has to be extended sufficiently far from the area of interest in order to consider it as infinite; therefore, in such cases it is useful to truncate the extension and apply to the acoustic boundary a wave passing condition outward from the domain without reflecting phenomena. This condition is ensured by specifying the corresponding impedance,

$$T(x) = -\frac{1}{c}\dot{p} \,, \tag{90}$$

where the damping coefficient c can be related to the fluid characteristics, bulk modulus K_f and density ρ_f,

$$c_f = \frac{1}{\sqrt{\rho_f K_f}} \,. \tag{91}$$

In order to reduce the computational efforts, in a dam analysis the extension of the basin can be truncated by imposing, at the end side, non-reflecting surfaces. These can be implemented by radiation boundary conditions previously described by Eq. (90).

Abaqus/CAE usage: Interaction module, Create, Acoustic Impedance from the Types box, select the surface from the model, Nonreflecting.

A further method for considering the reservoir basin as infinite consists in taking into account a reservoir length sufficiently extended as to ensure that the pressure waves generated by the fluid-structure interaction reach the end of the basin in a time longer than the duration of the seismic event [13]. This condition is achieved by considering a distance of the fictitious water boundary from the dam as approximately equal to 3÷4H, where H is the maximum height of the structure [21].

A partial absorption of waves by the bottom sediments of a dam reservoir can be simulated by combining Eq. (88) with the radiation settings provided by Eq. (91) and introducing a reflection coefficient ψ,

$$T(x) = \boldsymbol{n}^{-} \cdot \ddot{\boldsymbol{u}}^{s} - \frac{1}{\rho_f c_f} \frac{1-\psi}{1+\psi} \dot{p} \, . \tag{92}$$

Abaqus/CAE usage: Interaction module, Create, Acoustic Impedance from the Types box, select the surface from the model, Tabular, define the Acoustic Impedance Properties.

3.5.3 Definition of the seismic input

The Italian regulation NTC2008 – Technical Construction Normative – D.M. 14/01/2008, in accordance with the European Eurocode 8: design of structures for earthquake resistance, suggests three different methods for the definition of the seismic input, to which are associated different analysis procedures, linear (static or dynamic) or nonlinear (static or dynamic) [22,23].

- *Equivalent static seismic loads*. Horizontal forces, related to the PGA – Peak Ground Acceleration – expected for the site, are applied to regular structures proportionally to the element masses of the system. Static linear analyses are performed with this type of seismic input, assuming that the response is dominated by the first mode response.

- *Design response spectrum*. This type of seismic input is adopted for modal analysis (usually identified as dynamic analysis), explaining the maximum response of an SDOF system to a particular input motion. In relation to the participant mass and the spectral response of each mode, equivalent lateral forces can be evaluated for each of these and, finally, the maximum stresses of the whole structure can be evaluated by means of different modal combination rules. The response spectrum can be employed also in nonlinear static analyses, generally called pushover analysis. This consists of a synthetic procedure that identifies a synthetic control parameter, i.e. a virtual displacement, representative of the response, elastic and inelastic, of the whole structure. As a function of this parameter, a performance curve can describe the progressive damage of the structure, dissipating energy during plastic deformation.

The basic definition of elastic response spectrum is briefly recalled here. The elastic response spectrum of an acceleration record consists of the representation of the maximum values of the responses of each elastic SDOF oscillator as a function of their natural period *T*, when at the base of the basement the investigated acceleration time history is applied. The solution is obtained by integrating the general equation of motion for each oscillator with natural period *T*; by plotting the maximum value of an assigned parameter, i.e. displacement, as a function of period *T*, the response spectrum of the assigned parameter is achieved, i.e. displacement response spectrum $S_d(T)$. Starting from the response displacement spectrum $S_d(T)$, other two significant spectra can be derived, the pseudo velocity response spectrum $S_{pv}(T)$ and the pseudo acceleration response spectrum $S_{pa}(T)$.

- *Acceleration time history*. Natural acceleration records, derived from the recording of past seismic events, have to be preferred to artificial and synthetic accelerograms [24]. The main factors that characterize the seismic motion are the peak values of the ground movement (i.e. displacement, velocity or acceleration), the frequency content, the distribution of the acceleration impulses and the duration of the maximum acceleration period. This information can be gleaned from seismic monitoring networks available on the Italian territory (Italian Accelerometric Network – RAN) as well as on the main seismic interest areas of the World. Recorded data are then digitalized and archived in databases available online, such as Itaca – Italian Accelerometric Archive – of the National Institute of Geophysics and Volcanology [25] or the international IRIS. This type of seismic input can be employed for linear or nonlinear dynamic analyses by applying the records directly at the base of numerical models. In general, accelerograms have to be compatible with the reference spectrum expected for the site obtained by specific hazard analyses or provided by national regulations. Indeed, the Italian regulations provide, by means of a square geographic grid of 5 Km each side, parameters for the construction of the spectral shapes for each exceedance probability, depending on the considered limit states, in the reference period, which is a function of the aim of the structure. The parameters of a site, which are not coincident with a vertex of the grid, can be achieved by taking the weighted average between the values of the four vertex points of the square in which the position of interest is located. Italian regulations state that, in a dynamic time integration analysis, suitable sets of seven real time-history records can be employed, matching the target design spectrum of the specific site. NTC2008 states that the two horizontal seismic components (and the vertical one, if necessary) of a seismic event are applied simultaneously and the effects on the structure are the average values of the more unfavorable effects if seven groups (each group consisting of at least two horizontal components) of accelerograms are employed. In other cases, the effects on the structure are the values of the most unfavorable effects; in any case no fewer than 3 groups of accelerograms are employed. In the field of seismic analysis of dams the main limit states are [26]:

SLS – Serviceability Limit States –: OLS – Operational Limit State – defined by the exit from the condition of normal operation without damages and SLD – Damage Limit State – defined by the passing from the condition of repairable damages without release of water to the condition of non-repairable damages without release of water.

ULS – Ultimate Limit States –: SLV – Life-Safety Limit State – defined by the condition of damages that determine the uncontrolled release of water or the risk of loss of human life and SLC – Collapse Limit State – defined by the condition of collapse of the structure.

Time history accelerations can be analyzed and compared by means of different parameters. Effective acceleration a_{rms} can be defined as,

$$a_{rms} = \sqrt{\frac{1}{n}\sum_{i=1}^{n} a_i^2} \; , \tag{93}$$

where a_i, is the i-th acceleration time-history. The effective acceleration can be defined for a whole accelerogram record or for a generic time period *Δt*. Moreover, the effect of an earthquake on a structure can be described by the Spectrum Intensity of Housner, which is defined as the area under the velocity response spectrum curve S_V, the function of the relative damping ξ and of the fundamental period without damping T of a single degree of freedom system, between the periods 0.1 and 2.5 seconds [27,28]

$$I_H = \int_{0.1s}^{2.5s} S_V(T,\xi)\,dT \; , \tag{94}$$

The interval 0.1s ≤ T ≤ 2.5s allows us to take into account, in the intensity evaluation, the main effects of earthquakes on civil structures.

3.6 Material constitutive behaviour

Generally, in static and dynamic analyses of dam structures, linear elastic constitutive behaviour is adopted for the materials of the FE models. Constitutive equations generally relate stress σ to strain ε and also to temperature T [29,30]. Hook in 1660 theorized that for a certain class of solid the stress-strain relationship may be described by a linear relationship. This relation can be written in matrix form as,

$$\boldsymbol{\sigma} = [Z]\varepsilon \,, \tag{95}$$

where $[Z]$is a 6x6 matrix in a general three-dimensional state of stress. If the material is defined as *homogeneous*, the constants Z_{ij}, where i=1,...,6 and j=1,...,6, are all independent of x, y, z at any time t. Moreover, if the material is defined as *isotropic*, for a given point the constants Z_{ij} are independent of the orientation of the coordinate system. Imagine a parallelepiped with its sides parallel to the coordinate axes and submitted to the action of normal stress σ_x uniformly distributed over two opposite sides [30]. Experimentally it is known that these normal stresses do not produce any angular distortion in the element. The unit elongation of the element is,

$$\varepsilon_x = \frac{\sigma_x}{E} \,, \tag{96}$$

where E is a constant of the material called *Young's modulus*. Extension along x-direction is accompanied by lateral contraction,

$$\varepsilon_y = -\nu \frac{\sigma_x}{E} \,, \qquad \varepsilon_z = -\nu \frac{\sigma_x}{E} \,, \tag{97}$$

where v is a constant of the material called *Poisson's coefficient*. If the above element is subjected to the action of normal stresses σ_x, σ_y, σ_z, uniformly distributed along the sides, and of shear stresses, Hooke's law for a linear elastic isotropic solid is,

$$\{\varepsilon\}=\begin{Bmatrix}\varepsilon_{xx}\\ \varepsilon_{yy}\\ \varepsilon_{zz}\\ \varepsilon_{xy}\\ \varepsilon_{xz}\\ \varepsilon_{yz}\end{Bmatrix}=\begin{Bmatrix}\frac{1}{E}\left[\sigma_{xx}-\nu\left(\sigma_{yy}+\sigma_{zz}\right)\right]\\ \frac{1}{E}\left[\sigma_{yy}-\nu\left(\sigma_{xx}+\sigma_{zz}\right)\right]\\ \frac{1}{E}\left[\sigma_{zz}-\nu\left(\sigma_{xx}+\sigma_{yy}\right)\right]\\ \frac{1+\nu}{E}\sigma_{xy}\\ \frac{1+\nu}{E}\sigma_{xz}\\ \frac{1+\nu}{E}\sigma_{yz}\end{Bmatrix}. \tag{98}$$

To get this result, the strain components, produced by each of the stress components, have to be superposed by means of the method of superposition. This method is legitimate if the deformations are small and the corresponding small displacements do not affect the action of the external forces. By means of an algebraic inversion of Eq. (98), Hook's law can be rewritten as a relationship of stress in terms of strain,

$$\{\sigma\}=\begin{Bmatrix}\sigma_{xx}\\ \sigma_{yy}\\ \sigma_{zz}\\ \sigma_{xy}\\ \sigma_{xz}\\ \sigma_{yz}\end{Bmatrix}=\begin{Bmatrix}\frac{E}{(1+\nu)(1-2\nu)}\left[(1-\nu)\varepsilon_{xx}+\nu\varepsilon_{yy}+\nu\varepsilon_{zz}\right]\\ \frac{E}{(1+\nu)(1-2\nu)}\left[\nu\varepsilon_{xx}+(1-\nu)\varepsilon_{yy}-\nu\varepsilon_{zz}\right]\\ \frac{E}{(1+\nu)(1-2\nu)}\left[\nu\varepsilon_{xx}+\nu\varepsilon_{yy}+(1-\nu)\varepsilon_{zz}\right]\\ \frac{E}{1+\nu}\varepsilon_{xy}\\ \frac{E}{1+\nu}\varepsilon_{xz}\\ \frac{E}{1+\nu}\varepsilon_{yz}\end{Bmatrix}. \tag{99}$$

The term $\frac{E}{1+\nu}=2G$ defines the *Shear modulus G* that relates the shear stress to the shear strain. G is defined in terms of *E* and *ν*, therefore it is not a new property of the material. Therefore, the three-dimensional constitutive behaviour of a homogeneous linear elastic isotropic solid can be described by only two material properties: Young's modulus E and Poisson's coefficient ν or, in alternative, Lamé's constants, $\mu = G$ and $\lambda = \frac{E\nu}{(1+\nu)(1-2\nu)}$.

In relation to the states of deformation, the volumetric waves, which propagate into a medium, can be divided into longitudinal waves (P – waves) and transverse waves (S – waves). Under the hypothesis of propagation of such waves into an isotropic homogeneous elastic half-space, the velocities of propagation V_p and V_s can be related to the *Shear modulus G* and to the *Oedometric Constrained modulus E_{oed}* by means of the relations,

$$G = \rho V_s^2 , \tag{100}$$

$$E_{oed} = \rho V_p^2 , \tag{101}$$

where ρ is the bulk density. From the Theory of Elasticity, Young's modulus E is related to the Oedometric Constrained modulus E_{oed},

$$E = \frac{E_{oed}(1+\nu)(1-2\nu)}{(1-\nu)} . \tag{102}$$

The influence of discontinuities such as construction joints in the behaviour of concrete arch and arch-gravity dams are of crucial importance and they often require a finite element non linear modelling [31]. The non linear modelling also of blocks would allow for the identification of the evolution of damage through the whole structure. A wide review of inelastic constitutive models for concrete dams is offered in literature by Lee and Fenves, 1998 [32]. Considering the non linearity in the constitutive model of the materials, different theories can be taken into account. A fracture mechanics approach studies discrete cracking in simple concrete, as the crack surface changes the domain is re-meshed [33]. This model is well suited for slowly applied loads such as gravity and hydrostatic loads but dynamic analyses require large computational efforts. Fixed smeared crack models are those of Pal, 1976 [34], Vargas-Loli and Fenves, 1989 [35], and El-Aidi and Hall, 1989 [36,37]. They use a softening modulus related to the characteristic length of an element and fracture energy for concrete. Bhattacharjee and Léger, 1993 [38], applied an improved smeared crack approach to dams under seismic loads. A secant stiffness in the direction of maximum principal strain represents softening and the crack closure is modeled by modifying the softening parameter. Viscous damping is related to tangent stiffness to represent energy dissipation. Continuum damage mechanics, in contrast with the smeared crack approaches, also model material dam behaviour. The concept of degradation damage means the stiffness degradation does not include the evolution of elasto-plastic yield surface. As the name suggests, the basic concept of continuum damage mechanics is to provide an effective stress that maps the same stress in the micro cracked surface. Ghrib and Tinawi, 1995 [39], provided an orthotropic damage model dealing with the opening/closing of cracks, damage evolution and loading/unloading by total strain. Cervera et al., 1995 [40], developed an isotropic model taking into account the different concrete behaviour in tension and compression by dividing the stress tensor in the two components, both with an damage surface and evolution law. Also using the latter damage model, it is difficult to model the loading and unloading states because of the absence of inelastic strain. In this context, the plastic-damaged models proposed by Lee and Fenves, 1998 [41], combine the classical damage with plasticity providing inelastic strain and a defined evolution of the failure surface.

3.6.1 Plastic-damage constitutive model for concrete

The plastic damage model proposed by Lee and Fenves, 1998 [41], extends that developed by Lubliner et al., 1989 [42], called the Barcelona model. It is well suited to cyclic loading using the concept of fracture-energy-based damage. The model uses two damage variables, for tensile and compressive damage respectively and the yield function proposed by Lubliner is modified with multiple damage variables. The uniaxial strength functions are factorized into two parts to represent the effective stress and the stiffness degradation. Moreover the strength function is used to control the evolution of the yield surface.

- Constitutive relations

The incremental theory of plasticity decomposes the strain tensor $\boldsymbol{\varepsilon}$ into the elastic part $\boldsymbol{\varepsilon}^{\mathbf{e}}$ and the plastic $\boldsymbol{\varepsilon}^{\mathbf{p}}$ one. Remembering that the double dot product between the tensors **a** and **b** is defined as $\mathbf{a}:\mathbf{b}=a_{ij}b_{ij}$, for linear elasticity it is,

$$\boldsymbol{\varepsilon} = \boldsymbol{\varepsilon}^{e} + \boldsymbol{\varepsilon}^{p}\,; \qquad \boldsymbol{\varepsilon}^{e} = \boldsymbol{E}^{-1} : \boldsymbol{\sigma}\,, \tag{103 a, b}$$

where **E** is the elastic stiffness tensor and **σ** the Cauchy stress tensor. The stress-strain relation is,

$$\boldsymbol{\sigma} = \boldsymbol{E} : \left(\boldsymbol{\varepsilon} - \boldsymbol{\varepsilon}^{p}\right). \tag{104}$$

As explained by the continuum damage theory, the stress is proposed as effective stress $\overline{\boldsymbol{\sigma}}$ by a rank four tensor **D**,

$$\overline{\boldsymbol{\sigma}} = \boldsymbol{D} : \boldsymbol{\sigma}\,. \tag{105}$$

Defining the effective stress with the undamaged elastic stiffness, (104) becomes,

$$\overline{\boldsymbol{\sigma}} = \boldsymbol{E}_{0} : \left(\boldsymbol{\varepsilon} - \boldsymbol{\varepsilon}^{p}\right), \tag{106}$$

where $\mathbf{E_0}$ is the initial elastic-stiffness tensor. The isotropic damage is represented by a scalar degradation damage variable 0≤D<1, then **D**=1/(1-D)**I**, where **I** is the four rank identity tensor. Therefore Eq. (105) becomes,

$$\boldsymbol{\sigma} = \left(1 - \boldsymbol{D}\right)\overline{\boldsymbol{\sigma}}\,; \qquad \overline{\boldsymbol{\sigma}} = \left(1 - \boldsymbol{D}\right)\boldsymbol{E}_{0} : \left(\boldsymbol{\varepsilon} - \boldsymbol{\varepsilon}^{p}\right). \tag{107a,b}$$

The comparison between Eqs. (104) and (107) shows that $E=(1-D)\cdot E_0$, where D is the degradation of the elastic stiffness. In absence of damage, D=0, the effective stress $\overline{\boldsymbol{\sigma}}$ is equivalent to the Cauchy stress **σ** [10]. When damage occurs the effective stress is more representative than the Cauchy stress because the first takes into account the effective area that resists to the external loads.

For quasi-brittle material, the surface for which a state of failure or damage can be determined is called yield surface. This evolves with the damage evolution. The yield function for frictional material like concrete can be written as,

$$\overline{F}\left(\sigma\right) - c_{o} = 0\,, \tag{108}$$

where $\overline{\mathrm{F}}$ is a scalar function of invariants of stress tensor and c_o is the cohesion. In the Barcelona model the algebraically largest principal stress is included in order to give a yield function that better describes the compressive and tensile behaviours of concrete. It could therefore be written as,

$$\overline{F} = \frac{1}{1-o}\left(oI_1 + \sqrt{3J_2} + \varpi\langle\sigma_{max}\rangle\right); \tag{109}$$

where o and ϖ are two dimensionless constant, I_1 is the first invariant of stress tensor, J_2 is the second invariant of deviatoric stress tensor and $\sigma_{\max}$ is the algebraic maximum principal stress. Fig. 3.15 shows a plane stress cross section of the yield surface in the principal stress space. o depends on the initial shape of the yield function instead the evolution of the yield function is described by ϖ and the cohesion parameter c_0.

Plastic flow is described by a scalar plastic potential function Φ and in the effective stress space the plastic strain can be written as,

$$\dot{\varepsilon}^p = \dot{\lambda}\nabla\Phi\left(\overline{\sigma}\right) \tag{110}$$

where $\dot{\lambda}$ is the non-negative plastic multiplier. To describe the damage states another internal variable set κ is introduced, and its evolution can be expressed as,

$$\dot{\kappa} = \dot{\lambda}W\left(\overline{\sigma},\kappa\right); \tag{111}$$

where $\dot{\lambda}$ is the non-negative plastic multiplier and W can be derived considering plastic dissipation. For modelling cyclic behaviour of concrete, which has different tensile and compressive yield strengths, it is necessary to use two cohesion variables in the yield function: c_c compressive cohesion variable and c_t tensile cohesion variable. Therefore (108) can be expressed as,

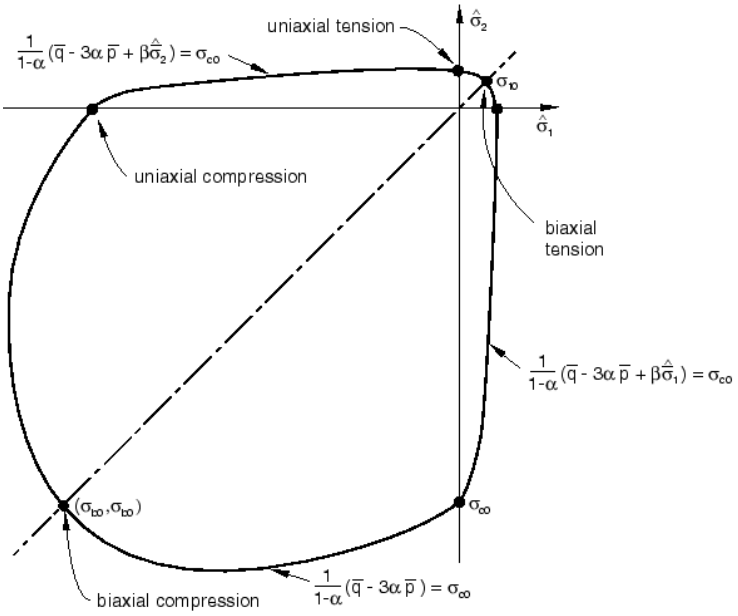

Fig.3.15. Yield Function in plane stress space [10].

$$\bar{F}(\sigma) = c_0(\kappa); \tag{112}$$

and (109) becomes,

$$\bar{F}(\sigma,\kappa) = \frac{1}{1-o}\left(oI_1 + \sqrt{3J_2} + \varpi\langle\sigma_{max}\rangle\right) - c_0(\kappa); \tag{113}$$

Because (112) is a combination of two different Drucker-Prager type functions, a function of the same type is used as plastic potential function in this model,

$$\Phi = \|s\| + \alpha_p I_1, \tag{114}$$

where $\|s\| = \sqrt{s:s}$ is the norm of the deviatoric stresses. α_p is chosen to express proper dilatancy. Therefore the plastic strain rate becomes,

$$\dot{\varepsilon}^p = \dot{\lambda}\left(\frac{s}{\|s\|} + \alpha_p I\right). \tag{115}$$

- Damage and Stiffness degradation

The evaluation of dissipated fracture energy required to generate microcracks in quasi-brittle material can define the damage. In the Barcelona model only one scalar variable is used to describe tensile and compressive damages [42], which is not appropriate to describe cyclic behaviour of concrete because of the different tensile and compressive damage processes. Lee and Fenves, 1998 [41], use two damage variables, one for tensile behaviour and one for compressive behaviour. Both are factorized into the effective-stress response and stiffness degradation response parts. The evolution of the hardening variables $\varepsilon^p{}_t$ and $\varepsilon^p{}_c$ is at first formulated for unaxial loading conditions and then extended to the multiaxial ones.

Uniaxial condition. Assuming the uniaxial stress-strain curves converted into compressive and tensile stress-plastic strain curves as,

$$\sigma_t = \sigma_t\left(\tilde{\varepsilon}_t^{\,p}, \dot{\tilde{\varepsilon}}_t^{\,p}, \vartheta, f_i\right);$$

$$\sigma_c = \sigma_c\left(\tilde{\varepsilon}_c^{\,p}, \dot{\tilde{\varepsilon}}_c^{\,p}, \vartheta, f_i\right); \tag{116}$$

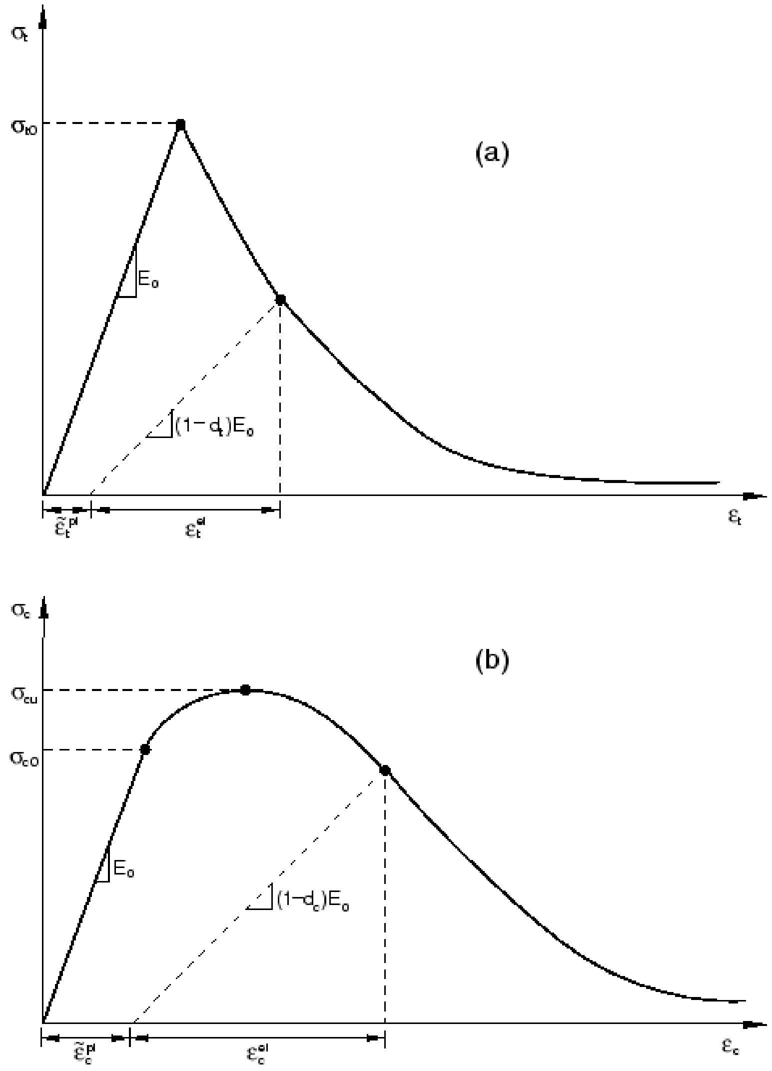

Fig. 3.16. Uniaxial loading response of concrete in (a) tension and (b) compression [10].

where $\dot{\tilde{\varepsilon}}_t^p$ and $\dot{\tilde{\varepsilon}}_c^p$ are the equivalent plastic strain rates, $\tilde{\varepsilon}_t^p = \int_0^t \dot{\tilde{\varepsilon}}_t^p dt$ and $\tilde{\varepsilon}_c^p = \int_0^t \dot{\tilde{\varepsilon}}_c^p dt$ are the equivalent plastic strains, ϑ is the temperature and f_i (i=1,2,...) are other predefined variables, the effective plastic strain rates can be written as,

$$\begin{aligned} \dot{\tilde{\varepsilon}}_t^{pl} &= \dot{\varepsilon}_{11}^{pl}\text{, in uniaxial tension,} \\ \dot{\tilde{\varepsilon}}_c^{pl} &= -\dot{\varepsilon}_{11}^{pl}\text{, in uniaxial compression.} \end{aligned} \tag{117}$$

Fig. 3.16 shows that when a concrete specimen is unloaded from any point of the softening branch of the stress-strain curves, both in tension and in compression, the stiffness of the material appears reduced due to damage. The behaviour in tension and compression is very different although it is more pronounced as the plastic strains increase. As mentioned before, the degraded response is characterized by two independent uniaxial damage variables, d_t and d_c, assumed functions of the plastic strain, temperature and other predefined fields,

$$d_t = d_t\left(\tilde{\varepsilon}_t^p, \vartheta, f_i\right), \quad \left(0 \le d_t \le 1\right),$$
$$d_c = d_c\left(\tilde{\varepsilon}_c^p, \vartheta, f_i\right), \quad \left(0 \le d_c \le 1\right), \tag{118}$$

and they assume a value close to zero for undamaged material and close to the unity for totally damaged material. Therefore, if E_0 is the undamaged elastic stiffness, the stress-strain relations under uniaxial load for tensile and compressive behaviours are,

$$\sigma_t = \left(1 - d_t\right)E_0\left(\varepsilon_t - \tilde{\varepsilon}_t^p\right),$$
$$\sigma_c = \left(1 - d_c\right)E_0\left(\varepsilon_c - \tilde{\varepsilon}_c^p\right). \tag{119}$$

Therefore the effective uniaxial stresses $\overline{\sigma}_t$ and $\overline{\sigma}_c$ are defined as,

$$\overline{\sigma}_t = \frac{\sigma_t}{\left(1 - d_t\right)} = E_0\left(\varepsilon_t - \tilde{\varepsilon}_t^p\right),$$
$$\overline{\sigma}_c = \frac{\sigma_c}{\left(1 - d_c\right)} = E_0\left(\varepsilon_c - \tilde{\varepsilon}_c^p\right). \tag{120}$$

Uniaxial cyclic conditions. Under cyclic conditions describing the damage process is quite complex due to the opening and closing of micro-cracks as well as their interactions. Moreover, the opening-closing process determines a stiffness recovery which is more evident during the switch from tension to compression stress, causing the cracks to close. For uniaxial cyclic conditions the stiffness reduction variable d is a function of the two uniaxial damage variables defined before, d_t and d_c, and of the stress state with s_t and s_c taking into account the stiffness recovery due to the loading changes.

$$(1-d)=(1-s_t d_c)(1-s_c d_t), \quad 0 \le s_t, \ s_c \le 1, \tag{121}$$

where,

$$\begin{aligned} s_t &= 1 - w_t r^*(\bar{\sigma}_{11}), \quad 0 \le w_t \le 1, \\ s_c &= 1 - w_c(1 - r^*(\bar{\sigma}_{11})), \quad 0 \le w_c \le 1, \end{aligned} \tag{122}$$

where,

$$r^*(\bar{\sigma}_{11}) = H(\bar{\sigma}_{11}) = \begin{cases} 1 & if \quad \bar{\sigma}_{11} > 0 \quad (tension) \\ 0 & if \quad \bar{\sigma}_{11} < 0 \quad (compression) \end{cases}, \tag{123}$$

w_t and w_c are material properties that control the stiffness recovery.

The equivalent plastic strain can be rewritten for the uniaxial cyclic conditions, reducing the strain values of Eq. (108), as,

$$\begin{aligned} \dot{\tilde{\varepsilon}}_t^{pl} &= r^* \dot{\varepsilon}_{11}^{pl}, \\ \dot{\tilde{\varepsilon}}_c^{pl} &= -(1 - r^*)\dot{\varepsilon}_{11}^{pl}. \end{aligned} \tag{124}$$

Multiaxial conditions. For the multiaxial conditions the equivalent plastic strain rates are defined as,

$$\begin{aligned} \dot{\tilde{\varepsilon}}_t^{pl} &= r(\hat{\bar{\sigma}})\hat{\dot{\varepsilon}}_{\max}^{pl}, \\ \dot{\tilde{\varepsilon}}_c^{pl} &= -(1 - r(\hat{\bar{\sigma}}))\hat{\dot{\varepsilon}}_{\min}^{pl}, \end{aligned} \tag{125}$$

where $\hat{\dot{\varepsilon}}_{\max}^{pl}$ and $\hat{\dot{\varepsilon}}_{\min}^{pl}$ are respectively the maximum and the minimum eigenvalues of the plastic strain rate tensor $\dot{\varepsilon}^{pl}$ and, remembering that the Macaulay brackets $\langle a \rangle$ describe a ramp function as $\{a\} = \begin{cases} 0, & x < 0, \\ 1, & x \ge 0, \end{cases}$,

$$r\left(\hat{\bar{\sigma}}\right) = \frac{\sum_{i=1}^{3} \left\langle \hat{\bar{\sigma}}_i \right\rangle}{\sum_{i=1}^{3} \left| \hat{\bar{\sigma}}_i \right|}, \quad 0 \le r\left(\hat{\bar{\sigma}}\right) \le 1, \tag{126}$$

is a stress weight factor. It is equal to the unity if all the principal stresses $\hat{\bar{\sigma}}_i$ are positive and it is equal to zero if $\hat{\bar{\sigma}}_i$ are negative. Ordering the eigenvalues of the plastic strain rate tensor $\dot{\varepsilon}^{pl}$ so that $\hat{\dot{\varepsilon}}^{pl}_{\max} = \hat{\dot{\varepsilon}}_1 \ge \hat{\dot{\varepsilon}}_2 \ge \hat{\dot{\varepsilon}}_3 = \hat{\dot{\varepsilon}}^{pl}_{\min}$, the equivalent plastic strains $\dot{\tilde{\varepsilon}}^{pl}$ can be expressed in the matrix form,

$$\dot{\tilde{\varepsilon}}^{pl} = \begin{bmatrix} \dot{\tilde{\varepsilon}}_t^{pl} \\ \dot{\tilde{\varepsilon}}_c^{pl} \end{bmatrix} = \hat{h}\left(\hat{\bar{\sigma}}, \tilde{\varepsilon}^{pl}\right) \cdot \hat{\dot{\varepsilon}}^{pl}, \tag{127}$$

where $\hat{\dot{\varepsilon}}^{pl} = \begin{bmatrix} \hat{\dot{\varepsilon}}_1 \\ \hat{\dot{\varepsilon}}_2 \\ \hat{\dot{\varepsilon}}_3 \end{bmatrix}$ and $\hat{h}\left(\hat{\bar{\sigma}}, \tilde{\varepsilon}^{pl}\right) = \begin{bmatrix} r\left(\hat{\bar{\sigma}}\right) & 0 & 0 \\ 0 & 0 & -\left(1 - r\left(\hat{\bar{\sigma}}\right)\right) \\ & & \end{bmatrix}$.

- Tension stiffening behaviour

The strain-softening behaviour for cracked-concrete is defined by tension stiffening. This relation allows to take into account also reinforcement in the concrete. The tension stiffening can be specified in this damage plasticity model by means of two approaches: a post-failure stress-strain relation or by adopting a fracture energy cracking criterion.

Post-failure stress-strain relation. This method assigns a function to describe the post-failure behaviour related to the cracking strain $\tilde{\varepsilon}_t^{ck}$, defined as,

$$\tilde{\varepsilon}_t^{ck} = \varepsilon_t - \varepsilon_{t0}^{el}, \tag{128}$$

where ε_t is the total strain and ε_{t0}^{el} is the elastic strain of the undamaged material defined as,

$$\varepsilon_{t0}^{el} = \frac{\sigma_t}{E_0}. \tag{129}$$

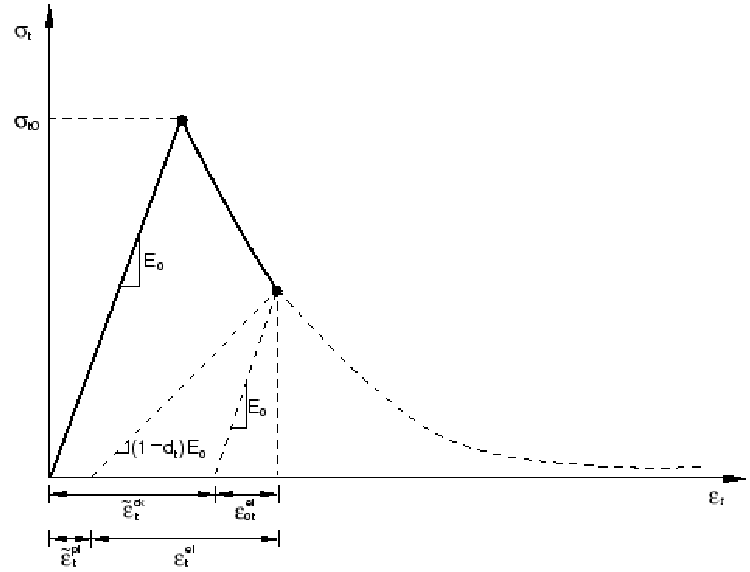

Fig. 3.17. Definition of the cracking strain $\tilde{\varepsilon}_t^{ck}$ functional to the definition of the tension stiffening data [10].

Fig. 3.17 explains the variables definition. The tension stiffness data are provided in terms of cracking strain, and when the unloading data are available, the tensile damage can be expressed by the $d_t - \tilde{\varepsilon}_t^{ck}$ curve. The tensile damage d_t can be defined for the descending branch by means of,

$$d_t = 1 - \frac{\sigma_t}{\sigma_{to}}, \tag{130}$$

where σ_t is the generic tensile stress value of the descending branch and σ_{to} is the peak value of the tensile stress diagram. The tensile damage can be specified by means of a tabular function of the cracking strain. ABAQUS® automatically evaluates the plastic strain values $\tilde{\varepsilon}_t^{pl}$ starting from the cracking strain values $\tilde{\varepsilon}_t^{ck}$ by means of the relation,

$$\tilde{\varepsilon}_t^{pl} = \tilde{\varepsilon}_t^{ck} - \frac{d_t}{(1-d_t)}\frac{\sigma_t}{E_0}, \tag{131}$$

In absence of tensile damage $\tilde{\varepsilon}_t^{pl} = \tilde{\varepsilon}_t^{ck}$.

In cases of little or no reinforcement, such as simple concrete arch, gravity or arch-gravity dams the specification of a post-failure stress-strain relation introduces mesh sensitivity to the results. The finite element prediction does not

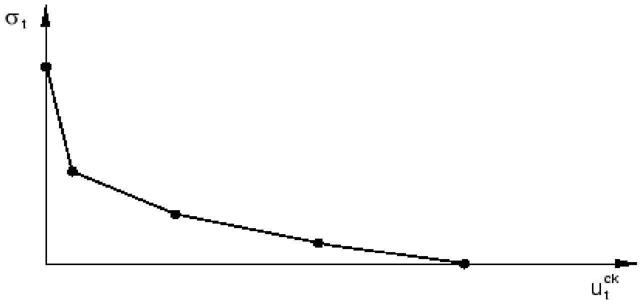

Fig. 3.18. Post-failure stress displacement curve [10].

converge to a unique solution refining the mesh, because finer mesh leads to narrower crack bands.

Fracture energy cracking criterion. In order to avoid the mesh sensitivity problem discuss previously, for simple concrete structures the Hillerborg's fracture energy proposal [43,10] can be employed. The criterion proposes considering the energy required to open a unit area of crack, G_f, as a material parameter, using brittle fracture concepts. In this way the post-failure behaviour is described by a stress-displacement response rather than a stress-strain response defining the post-failure stress as a function of the cracking displacement, Fig. 3.18. An alternative is to directly specify the fracture energy G_f as a material property, such as the area under the $\sigma_t - u_t$ curve. If the tensile damage d_t is specified as reported by Eq. (121), ABAQUS® evaluates the "plastic" displacement as a function of cracking displacement,

$$u_t^{pl} = u_t^{ck} - \frac{d_t}{(1-d_t)}\frac{\sigma_t l_0}{E_0}, \tag{132}$$

where the specimen length l_0, is assumed to be unitary, not influencing the crack opening. However, the method requires the definition of a characteristic length associated with an integration point. Its definition depends on the geometry and formulation of the element and it is generally a line across the element. The definition of crack length is required because the crack direction is not known in advance: elements with large aspect ratio can have different behaviour depending on the crack direction; therefore, elements with aspect ratio close to one have to be preferred. The tensile damage can be specified, in the fracture energy criterion, by means of a tabular function of the cracking displacement.

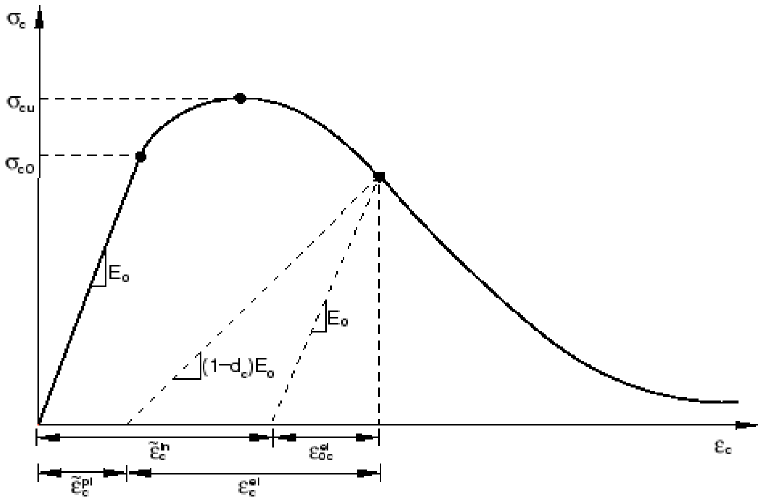

Fig. 3.19. Definition of the compressive inelastic strain $\tilde{\varepsilon}_c^{in}$ functional to the definition of the compression hardening data [10].

- Compressive behaviour

The stress-strain compressive behaviour can be defined outside the first ascending elastic branch, beyond the ultimate compressive stress, in the strain-softening descending branch. The hardening behaviour is defined by an inelastic strain $\tilde{\varepsilon}_c^{in}$ rather than in terms of plastic strain $\tilde{\varepsilon}_c^{pl}$,

$$\tilde{\varepsilon}_c^{in} = \varepsilon_c - \varepsilon_{c0}^{el} , \tag{133}$$

where ε_c is the total strain and ε_{c0}^{el} is the elastic strain of the undamaged material defined as,

$$\varepsilon_{c0}^{el} = \frac{\sigma_c}{E_0} . \tag{134}$$

Fig. 3.19 explains the variables definition. When the unloading data are available, the tensile damage can be expressed by the $d_c - \tilde{\varepsilon}_c^{in}$ curve. The compressive damage d_c can be defined for the descending branch by means of

$$d_c = 1 - \frac{\sigma_c}{\sigma_{cu}} , \tag{135}$$

where σ_c is the generic compressive stress value of the descending branch and σ_{cu} is the peak value of the compressive stress diagram. The compressive damage can be specified by means of a tabular function of the inelastic strain. ABAQUS® automatically evaluates the plastic strain value $\tilde{\varepsilon}_c^{pl}$ starting from the inelastic strain value $\tilde{\varepsilon}_c^{in}$ by means of the relation,

$$\tilde{\varepsilon}_c^{pl} = \tilde{\varepsilon}_c^{in} - \frac{d_c}{(1-d_c)}\frac{\sigma_c}{E_0}\,. \tag{136}$$

- Stiffness recovery

ABAQUS® deals with the stiffness recovery aspect by means of stiffness recovery factors w_c and w_t. From experimental observation of quasi-brittle materials behaviour, it was found that the compressive stiffness is recovered as the load changes from tension to compression. On the other hand, once micro cracks have been developed, the tensile stiffness is not recovered as the load changes from compression to tension. This condition is implemented by the software by default, imposing w_c=1 and w_t=0.

3.7 Vertical joint modelling

A detailed representation of the dam structure allows to better understand the local and then the global system response. Indeed, concrete arch and arch-gravity dams are built as a system of cantilever blocks separated by vertical joints [8]. During the construction phase the joints are open in order to allow cooling and shrinkage phenomena of the concrete. The concrete casting of the cantilevers proceeds in several layers, during which the blocks are independent but the joints are grouted before the next layer is built. After the construction of the cantilevers is completed, some phenomena of shrinkage can broaden the joints; therefore, from the inspection galleries, that cross longitudinally dam structures at different levels, they can be re-injected midway between two blocks, in a radial direction and repeated several times in order to fill the contacts as much as possible. The mortar injections restore the monolithic behaviour between the blocks and, at the same time, ensure the correct deformation, avoiding structural cracking due to concrete shrinkage, hydrostatic level variations and other factors such as temperature. However, the joints are also planes of weakness of the structure, in particular when dynamic forces such as seismic events occur [44]. As underlined by ICOLD – International

Committee on Large Dams – and by ITCOLD – Italian Committee on Large Dams – the effects of historical earthquakes on concrete dams are mostly related to contraction joints [45,46,47]. Indeed, in literature several models are available to simulate the opening, closing and/or shear sliding of joints under seismic events, also including non-linear effects [48,49]. Joint discontinuities can be treated by constraint equations or by springs at the surface nodes [50]. This procedure, although less time consuming, cannot take into account the real joint properties in terms of geometry or material. Other works treat the joint interface by means of special finite elements such as that developed for two or three dimensional FEM analyses by Bfer, 1985 [51]. An extension for dynamic analysis is provided by Fenves, 1992 [52], developing a non-linear three dimensional joint element for simulating non-linear behaviour along the normal direction when the joints open or close, while along the tangential direction an elastic behaviour is adopted. The model is improved by Fenves, 1992 [53] by giving an approximation of the sliding force in the joint. A zero-thickness element simulating opening and closing as well as tangential behaviour is developed by Lau et al., 1998 [48], and by Azmi et al., 2001 [44]. Azmi et al., 2001 [44], also underline how nonlinear seismic analyses of dams are mostly carried out by means of two-dimensional simulations and how, instead, three-dimensional analyses are required to better describe the seismic response of concrete dams including nonlinearity of vertical joints. Ahmadi et al., 2001 [49], propose a nonlinear joint element model with a coupled shear-tensile behaviour included into a realistic three-dimensional dam-reservoir model. Recently Qiang et al., 2014 [54], propose, in a dam-foundation-reservoir system, a new contraction joint element to model the joint-block interface in cases where the meshes of the two parts are different. Also experimental studies on the influence of vertical joints have been carried out, such as the work of Wang et al., 2015 [55]. They include, in a physic model of an arch dam, vertical joints as 1mm wide cracks; no continuity between adjacent parts is therefore ensured. According to reports in all the previous works, in arch, gravity and arch-gravity dams a crucial role is played by vertical construction joints mostly when dynamic forces such as seismic events occur. Therefore a detailed representation of the dam structure allows for a better understanding of the local and then the global system response.

3.7 Chapter bibliography

[1] Chopra A., "Dynamic of structures", 4th ed., Paerson Prentice Hall, Ed., 2012.

[2] Cluni F.. "Dynamic of Structures", [Online]. http://www.strutture.unipg.it/fms/DS/#materiale

[3] Panico P., "Progettazione antisismica multiprestazionale di pareti in cfs e pannelli basata su analisi dinamiche inelastiche," 2007.

[4] Newmark N. M., "A Method of Computation for Structural Dynamics," *Journal of the Engineering Mechanics Division*, vol. 85, no. 3, pp. 67-94, 1959.

[5] Mantica I., "Hydraulic Constructions", 1992.

[6] Arredi F., "Arch-gravity dams", 1956.

[7] Zienkiewicz R. L., Cecil O. and Taylor, "The finite element method Volume 1: The Basis", 5th ed., 2000.

[8] Ghanaat Y., "Theoretical manual for analysis of arch dams", *Quest structures emeryville CA*, 1993.

[9] Bathe K., "Finite element procedures", Second Edition ed., 2016.

[10] (2012) Abaqus Documentation.

[11] ICOLD, "Bulletin 148 - SELECTING SEISMIC PARAMETERS FOR LARGE DAMS Guidelines", 2016.

[12] ICOLD, "Bulletin 155 - Guidelines for use of numerical models in dam engineering", 2013.

[13] Hellgren R., "Inuence of Fluid Structure Interaction on a Concrete Dam during Seismic Excitation -Parametric analyses of an Arch Dam-Reservoir-Foundation system," 2014.

[14] Buttarazzi G., "Fluid-structure interaction in the seismic assesment of large gravity dams: appllications to study cases," Pisa, 2014.

[15] Souli M. and Benson D. J., "Arbitrary Lagrangian-Eulerian and Fluid-Structure Interaction", 2013.

[16] Kuo J. S.-H., "Fluid-Structure Interactions: added mass computations for incompressible fluid", Repot, 1982.

[17] Zangar C.N., "Hydrodynamic Pressures on Dams due to Horizontal

Earthquake Effects", *Engineering Monographs No. 11, Denver*, 1952.

[18] Chopra A. K., "Hydrodynamic Pressures on Dams During Earthquakes", *Journal of the Engineering Mechanics Division*, vol. 93, no. 6, pp. 205-224, 1967.

[19] Chopra A. K., "Earthquake Resistant Design of Concrete Gravity Dams", *Journal of the Structural Division*, vol. 104, no. 6, pp. 953-971, 1978.

[20] Fenves G. and Chopra A. K., "Simplified Earthquake Analysis of Concrete Gravity Dams", *Journal of Structural Engineering*, vol. 113, no. 8, pp. 1688-1708, Aug. 1987.

[21] Bari S. et al., "Water Length and Height Effects on the Earthquake Behavior of Arch Dam-Reservoir-Foundation Systems", *KSCE Journal of Civil Engineering*, vol. 15, no. 2, pp. 295-303, 2011.

[22] Ministero delle Infrastrutture e dei Trasporti, D.M. 14-01-2008. Norme Tecniche per le Costruzioni, 2008.

[23] Parducci A., "Fondamenti di ingegneria sismica in 80 lezioni : per un'ingegneria ed un'architettura antisismiche : D.M. 14 gennaio 2008", Liguori, 2011.

[24] Bommer J.J. and Acevedo A. B., "The use of real earthquake accelerograms as input to dynamic analysis", *Journal of Earthquake Engineering*, vol. 8, no. sup001, pp. 43-91, Jan. 2004.

[25] Luzi L. et al., "ITACA (ITalian ACcelerometric Archive): A Web Portal for the Dissemination of Italian Strong-motion Data", *Seismological Research Letters*, vol. 79, no. 5, pp. 716-722, Sep. 2008.

[26] Ministero delle Infrastrutture e dei Trasporti, D.M. 26-06-2014. Norme tecniche per la progettazione e la costruzione degli sbarramenti di ritenuta (dighe e traverse), 2014.

[27] Housner G. W., "Spectrum Intensities of Strong-Motion Earthquakes", 1952.

[28] Caterino M., Manfredi N. and Polese G., "Effetto delle serie sismiche per il danneggiamento strutturale. Effect of earthquakes for the structural damage", Master Thesis, 2003.

[29] *CONSTITUTIVE RELATIONS FOR LINEAR ELASTIC SOLIDS - Mechanical Constitutive Equations*. Foundation Coalition, 2001.

[30] Timoshenko S. and Goodier J. N., "Theory of elasticity", McGraw-Hill,

1970.

[31] ICOLD, "Bulletin 155 - GUIDELINES FOR USE OF NUMERICAL MODELS IN DAM ENGINEERING", 2013.

[32] Lee J. and Fenves G. L., "A plastic-damage concrete model for earthquake analysis of dams", *Earthquake Engineering & Structural Dynamics*, vol. 27, no. 9, pp. 937-956, Sep. 1998.

[33] Ayari V. E. and Saouma M. L., "A fracture mechanics based seismic analysis of concrete gravity dams using discrete cracks", *Engineering Fracture Mechanics*, vol. 35, no. 1-3, pp. 587-598, Jan. 1990.

[34] Pal N., "Seismic Cracking of Concrete Gravity Dams", *Journal of the Structural Division*, vol. 102, no. 9, pp. 1827-1844, 1976.

[35] Vargas-Loli L. M. and Fenves G. L., "Effects of concrete cracking on the earthquake response of gravity dams", *Earthquake Engineering & Structural Dynamics*, vol. 18, no. 4, pp. 575-592, May 1989.

[36] El-Aidi B. and Hall J. F., "Non-linear earthquake response of concrete gravity dams part 1: Modelling", *Earthquake Engineering & Structural Dynamics*, vol. 18, no. 6, pp. 837-851, Aug. 1989.

[37] El-Aidi B. and Hall J. F., "Non-linear earthquake response of concrete gravity dams part 2: Behaviour", *Earthquake Engineering & Structural Dynamics*, vol. 18, no. 6, pp. 853-865, Aug. 1989.

[38] Bhattacharjee S. S. and Léger P., "Seismic cracking and energy dissipation in concrete gravity dams", *Earthquake Engineering & Structural Dynamics*, vol. 22, no. 11, pp. 991-1007, Nov. 1993.

[39] Ghrib F. and Tinawi R., "An application of damage mechanics for seismic analysis of concrete gravity dams", *Earthquake Engineering & Structural Dynamics*, vol. 24, no. 2, pp. 157-173, Feb. 1995.

[40] Cervera M., Oliver J., and Faria R., "Seismic evaluation of concrete dams via continuum damage models", *Earthquake Engineering & Structural Dynamics*, vol. 24, no. 9, pp. 1225-1245, Sep. 1995.

[41] Lee J. and Fenves G. L., "Plastic-Damage Model for Cyclic Loading of Concrete Structures", *Journal of Engineering Mechanics*, vol. 124, no. 8, pp. 892-900, Aug. 1998.

[42] Lubliner E., Oliver J., Oller J. and Oñate S., "A plastic-damage model for concrete", *International Journal of Solids and Structures*, vol. 25, no. 3,

pp. 299-326, Jan. 1989.

[43] Hillerborg P.-E., Modéer A., Petersson M., "Analysis of crack formation and crack growth in concrete by means of fracture mechanics and finite elements", *Cement and Concrete Research*, vol. 6, no. 6, pp. 773-781, Nov. 1976.

[44] Azmi M. and Paultre P., "Three-dimensional analysis of concrete dams including contraction joint non-linearity", *Engineering Structures*, vol. 24, no. 6, pp. 757-771, June 2002.

[45] Berberian M., Qorashi M., Jackson J. A., Priestley K. and Wallace T., "The rudbar.tarom earthquake of 20 June 1990 in NW Persia: preliminary field and sismological observations, and its tectonic significance", *Bulletin of the Seismological Society of America*, vol. 82, no. 4, 1755.

[46] ITCOLD, "Work group - Behaviour of the existing dams under seismic actions [Comportamento delle dighe esistenti sottoposte a sollecitazioni sismiche]", 2017.

[47] ICOLD, "13rd Congress - Congresses Proceedings", New Delhi, 1979.

[48] David T. L., Noruziaan B. and Razaqpur A. G., "Modelling of contraction joint and shear sliding effects on earthquake response of arch dams", *Earthquake Engineering & Structural Dynamics*, vol. 27, no. 10, pp. 1013-1029, Oct. 1998.

[49] Bachmann H., Ahmadi M. T. and Izadiniaa M., "A discrete crack joint model for nonlinear dynamic analysis of concrete arch dam", *Computers & Structures*, vol. 79, no. 4, pp. 403-420, Feb. 2001.

[50] Dowling M. J. and Hall J. F., "Nonlinear Seismic Analysis of Arch Dams", *Journal of Engineering Mechanics*, vol. 115, no. 4, pp. 768-789, Apr. 1989.

[51] Bfer G., "An isoparametric joint/interface element for finite element analysis", *International Journal for Numerical Methods in Engineering*, vol. 21, no. 4, pp. 585-600, Apr. 1985.

[52] Fenves G. L., Mojtahedi S. and Reimer R. B., "Effect of Contraction Joints on Earthquake Response of an Arch Dam", *Journal of Structural Engineering*, vol. 118, no. 4, pp. 1039-1055, Apr. 1992.

[53] Fenves G. L., "Parameter study of joint openings effects on earthquake response of arch dams", University of California, 1992.

[54] Qiang X., Jian-yun C., Jing L. and Hong-yuan Y., "A study on the contraction joint element and damage constitutive model for concrete arch dams", *Journal of Zhejiang University SCIENCE A*, vol. 15, no. 3, pp. 208-218, Mar. 2014.

[55] Wang S. S., Zhang Y. F., Cao M. S. and Xu W., "Effects of Contraction Joints on Vibrational Characteristics of Arch Dams: Experimental Study", *Shock and Vibration*, vol. 2015, pp. 1-7, Sep. 2015.

4. From the dense point cloud to the finite element model: the Ridracoli case history

For many years now, FEM simulations have been recognized as essential tools in the analysis of the behaviour of dam systems. International committees such as ICOLD – International Committee on Large Dams – and the parallel national organizations such as the Italian ITCOLD – Italian Committee on Large Dams – have acknowledged that the use of numerical tools has become standard practice in dam engineering [1,2,3,4,5]. A detailed representation of the dam structure allows for a better understanding of the local and subsequently of the global system response.

4.1 The structure and the monitoring system

The structure. The Ridracoli dam is an arch-gravity dam in simple concrete. The dam body is a double-curved structure, symmetrical with respect to the main section, resting on a *pulvino* foundation base that extends all around the perimeter of the abutments. The upstream and downstream facings, following

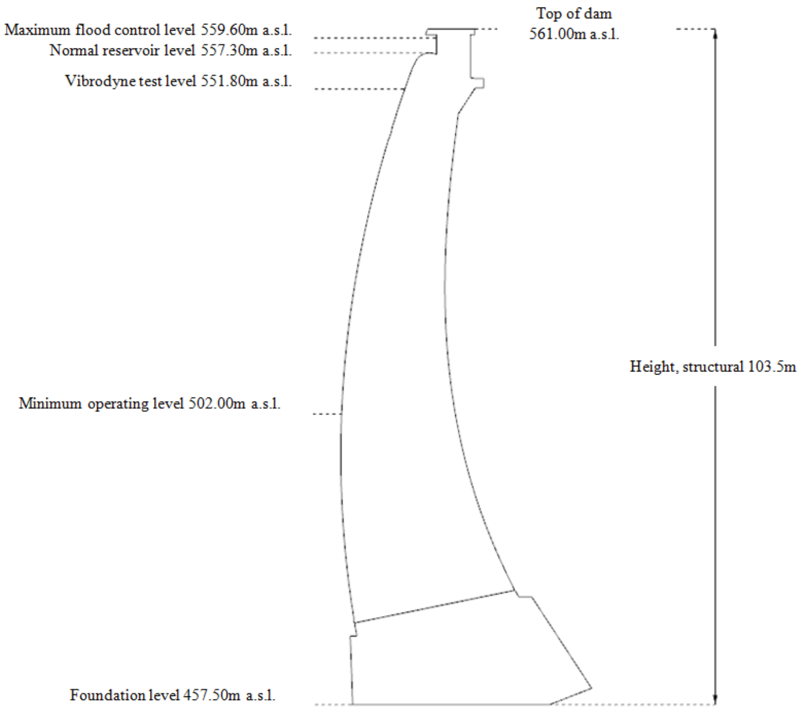

Fig. 4.1. Key cantilever of the Ridracoli dam.

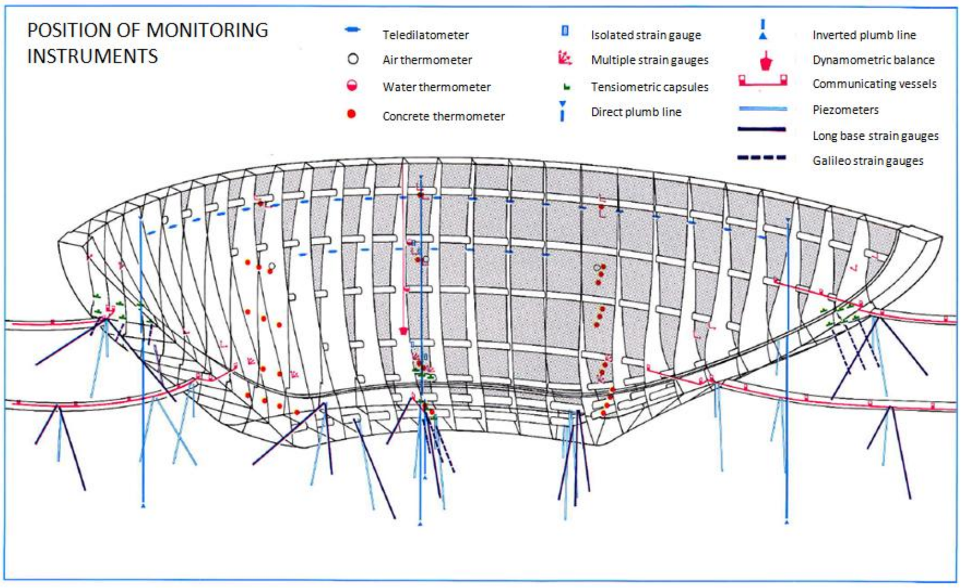

Fig. 4.2. The monitoring system of Ridracoli dam [6].

specific analytical laws, give progressively increasing thickness to the arches along the horizontal sections, from the middle to the sides and along the vertical section from the top to the base, in line with the arch gravity construction type. Three different arches, with variable curvature centres in the three-dimensional space, characterize the downstream face and only one characterizes the upstream face. After the construction of the *pulvino*, which regularizes the excavation of the abutments and allows for the redistribution of stresses and strains, the dam body was built in blocks. Indeed, the construction in subsequent blocks avoids structural cracking due to concrete shrinkage and variations in hydrostatic level and temperature. The connection between the 27 cantilevers was ensured by the injection of mortar (fluid concrete) into the joints. The injections were performed through the inspection galleries midway between two blocks, in a radial direction and repeated several times in order to fill the contacts as much as possible. Moreover, during the concrete casting of adjacent blocks, plastic water-stop elements were placed along the perimeter of the inspection galleries and along the external perimeter of the joint. They have the dual function of preventing infiltration of the water and spillage of the cement grout, used for the suture of the joints. The principal dimensions of the structure are reported in Fig. 4.1. The dam structure has a maximum height of 103.50m and a crest length of 432.00m, in the key section the top thickness is

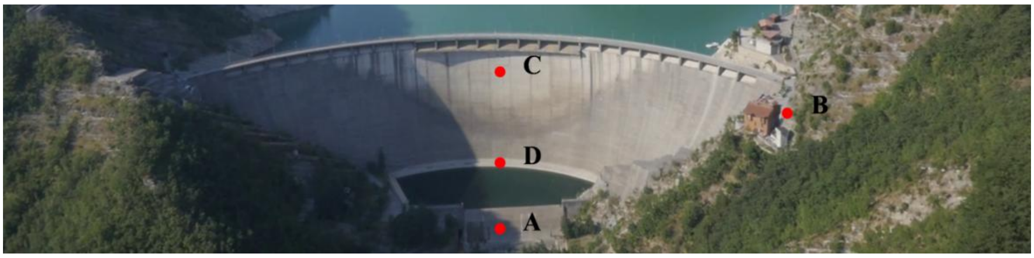

Fig. 4.3. The Ridracoli dam: accelerometers positions. In red the positions of the accelerometers.

of 7.00m and the base thickness is of 36.00m. The structure has, in the central part of the crest, eight square free overflow (ogee crest) spillways, the water discharge throughout them is governed by their geometry, with a maximum capacity of 600m^3/s. During overflow, the flowing water dissipates its energy in the stilling basin constructed at the foot of the downstream face of the dam. Moreover, the dam has a middle height sluice gate, a bottom sluice gate and a depletion sluice gate.

The monitoring system. The control of the behaviour of the structure, the foundation rock, the reservoir banks and the downstream rocky slopes is achieved through a complex monitoring system activated during the construction phase [6]. Most of the instruments and measuring points are located in the five radial sections of the structure: the key section, the two external lateral ones and the two intermediate lateral ones, Fig. 4.2 [6,7]. Hydrostatic level, concrete, water and air temperatures, displacements, uplift pressures, deformations of concrete and rocks, and stresses in the dam body are periodically measured. Moreover, the dynamic monitoring system includes a seismometer, accelerometers, strain gauges and hydrodynamic capsules. The seismometer, which acquires all seismic events, triggers the dynamic monitoring system when the recorded acceleration time-history at the crest exceeds 0.2 m/s^2 along the upstream-downstream direction. Furthermore, the seismic monitoring system records measurements for the entire duration of a seismic event. Moreover, at the end of the event, the static monitoring system performs an exceptional recording in order to compare the state of the structure before and after the motion [7]. The seismic motion at the foundation rock is recorded by an accelerometer located near the left side of the dam, at the same level of the crest, point B, and in the foundation rock at 40m depth, point A, Fig. 4.3. The structural response is monitored by two accelerometers placed near the foundation base, point D, and near the crest of the dam, point C, Fig. 4.3. The centralized acquisition of 284 instruments out of a total of 985 is performed in the guardhouse. Data are acquired with different temporal frequencies and they are stored in a computerized system called INDACO, active since 1992; this is connected on-line with the CESI-ISMES centre of Bergamo. It allows for the design of trend diagrams of variables, the storage of measurements and the comparison, in real time, of the current behaviour of the structure with that provided by a theoretical model. The latter is contained in MISTRAL, a decision support system, which analyses and filters the data from 42 automatic instruments deemed significant for the identification of the state of the structure. In a dual way, the on-line control is combined with a further off-line system; it is based on the totality of the manual and automatic data stored in the MIDAS system in order to validate the correct operation of the structure [6,8,9].

4.1.1 Interactive database

In addition to the previously mentioned on-line and off-line data storage and interpretation systems, an interactive database in Microsoft Access® is developed in the present study. This catalogues all the 985 instruments and acquisition points (an instrument can be characterized by different measurement points) and their records from the testing phase of the dam, circa 1983, to 02/02/2015 (the beginning of the present study). The key *Tools Table*, which

Fig. 4.4. UAV Dense Point Cloud missing of part of the upstream face because of the presence of the water.

reports the instrument/acquiring points characteristics in terms of description, position, functionality, acquired quantity, acquiring frequency and so on, is connected to the *Quantities Tables*, which contain the records of hydrostatic level, temperature, stresses, strains, uplift pressures, hydrometeorology, seismic data and so on. The database allows for the identification of sets of data resulting from the overlapping of several circumstances: by means of *queries*, from the wide amount of data, for example, all the significant seismic events can be extracted, with the same peak acceleration, which occurred at the same hydrostatic level, or the selection can concern the static field extracting, for example, the horizontal displacement of the structure due to certain thermal and/or hydrostatic level variations.

4.2 UAV dense point cloud integration

Although the drone survey was performed in August 2015 when the reservoir level was as close as possible to the average value of the minimum operating level of the last 10 years (518.83m a.s.l.), the water level during the survey was 543.28m a.s.l. and the majority of the upstream face of the dam was under the hydrostatic level. Therefore, the drone was able to shoot frames of neither that

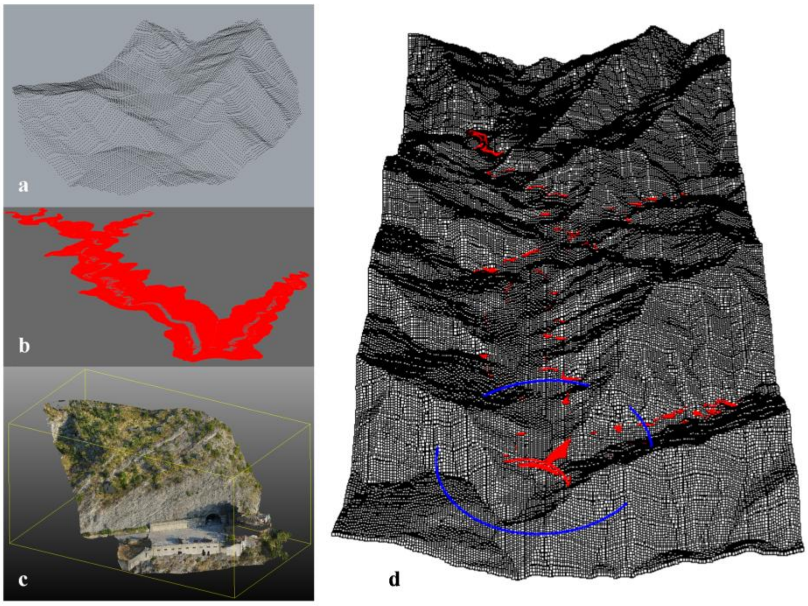

Fig. 4.5. a) DEM of the Ridracoli area; b) bathymetry of the lake; c) UAV dense point cloud of the left side of the dam; d) merging of the data sets, in blue the circle that is considered as the proper extension of the water and rock mass parts.

Fig. 4.6. Extraction of the significant points describing the vertical joints in CloudCompare®.

part nor the foundation all around the excavation perimeter, Fig. 4.4. As confirmed by the validation analysis reported in §2.6.5, the technical drawings, in digital format, can be employed to integrate the UAV dense point cloud in the missing parts of the structure. Moreover, in order to simulate a proper extension of the surrounding area, the UAV dense point cloud is integrated, also in this field, by data from different sources. The general overview of the area is provided by the DEM – Digital Elevation Model – TINITALY/01 [10]. The spatial reference system is WGS84 – World Geodetic System – / UTM – Universal Transverse Mercator – zone 32 and the cells are 10X10m in dimension, Fig 4.5 a. To be employed into the integration of the UAV dense point cloud, this data is converted in the Gauss-Boaga cartographic system by means of a geographic information system. The shape of the bottom of the lake is reproduced in detail by the contour lines of the bathymetry of the lake, provided by the owners of the dam, Fig. 4.5 b. This data source is already in Gauss-Boaga cartographic system. The lines are converted into points, by means of a 3D modelling software, to guarantee the homogeneity of the sets of information. Finally, the areas around the structure are described in more detail by the UAV dense point cloud, Fig. 4.5 c. The high detail of the drone information, including also the RGB information of the points, allows for reproduction of the transition surfaces between the different parts of the dam system. All the presented data sets are aligned, as explained, to the common Gauss-Boaga reference system and then appropriately merged, Fig. 4.5 d. All the data sets are homogenized to punctual format, therefore, on overlap areas of different information sources, all the point sets are employed to create the surface or identifying the significant lines of contour or, if the surface is not a plane, employing the points as support of the double curvature surface.

4.3 Solid model construction

The UAV dense point cloud is the base for the construction of the solid model of the dam system. Significant points, that can describe elements with different mechanical characteristics, interactions or boundary conditions, are extracted. The criteria are based on the knowledge of the dam system elements, RGB information associated to the points and/or on the recognizable curvature changes. The selection operations are carried out using the CloudCompare® open source 3D point cloud editing and processing software, by means of the *point list picking*, Fig. 4.6. Subsequently, the extracted points are exported into .txt format and they are imported to the Rhinoceros® commercial 3D modelling software. This is the environment in which all the previously described integration procedures are carried out. Connecting the significant points, lines are drawn: these are the contours for close polysurfaces that, including a volume, are solids by definition. The high accuracy of the survey allows for the modelling of some important details such as the vertical joints, the spillways, the stilling basin and the concrete blocks of the right and left sides, Fig. 4.7 a. Each element is exported in .stp/.step format and then, one at a time, they are imported to the Abaqus/CAE® – Computer-Aided Engineering – pre-processor of the commercial Abaqus FEA® – Finite Element Analysis – platform, Fig. 4.8. After assigning the properties, the parts are assembled and loads, interactions and boundary conditions are specified, as discussed below.

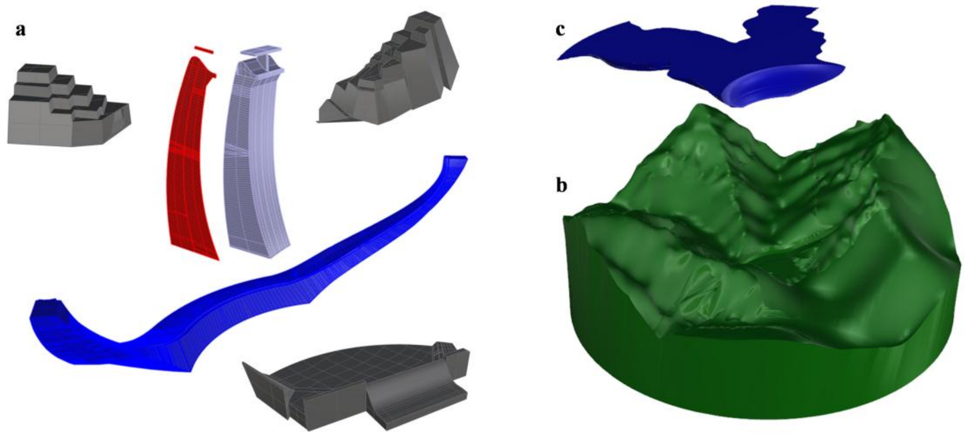

Fig. 4.7. Solid elements in Rhinoceros®. a) a joint, a block, pulvino foundation, the left and right weight concrete blocks and the stilling basin; b) the rock mass; c) the water reservoir.

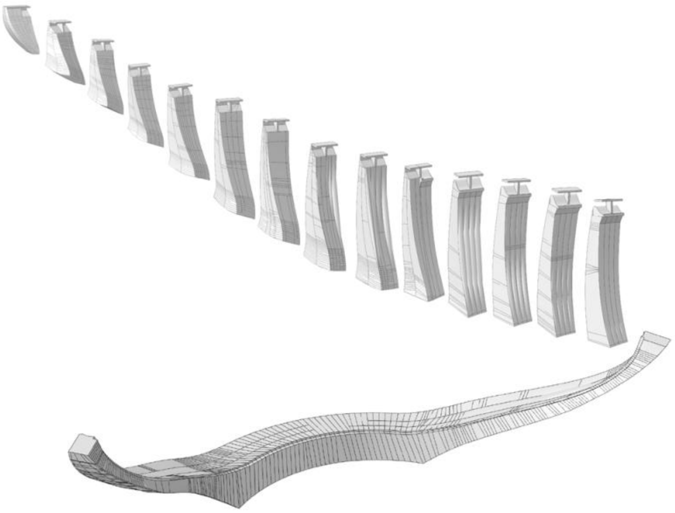

Fig. 4.8. Some imported parts in Abaqus/CAE®.

4.3.1 Dam body modelling

As already underlined, the high accuracy of the UAV survey allows for the reconstruction of important details of the structure. By employing the technical drawings to integrate some missing parts of the UAV dense point cloud, it is possible to represent the behaviour of the vertical joints. As outlined in §3.7, several authors deal with the vertical joint modelling of masonry dams. They propose their joint model, implementing it for numerical procedures, but rarely or never are different modelling procedures tested on the same structure. Therefore, the present study proposes and analyses three vertical joint modelling procedures, progressively closer to reality, building as many FEM models of the same dam structure: monolithic, surface-to-surface and solid element joint representations.

The monolithic model ensures the continuity between adjacent blocks, Fig. 4.9 a. Although the blocks have been modelled as independent parts also in this representation, the rigid connection between them is ensured by means of surface-based *tie* constraint, which makes the translational degrees of freedom equal for the pair of surfaces.

The surface-to-surface joint model simulates the discontinuity between blocks along the contact surfaces, Fig. 4.9 b. A general-contact interaction has

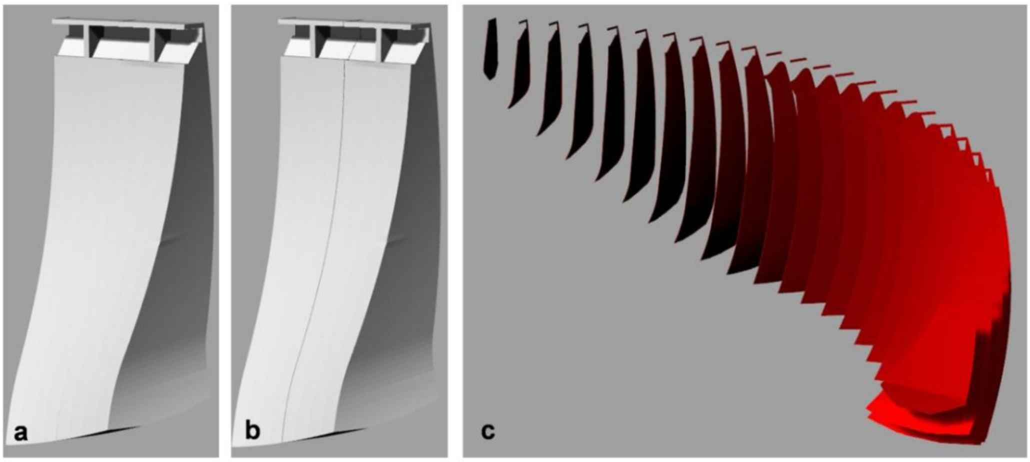

Fig. 4.9. Vertical joint modelling procedures. a) Two adjacent blocks of the monolithic representation, there is no discontinuity between them; b) two adjacent blocks of the surface-to-surface joint representation, there is a surface of discontinuity; c) joints of the solid element joint representation, there is an element of discontinuity between adjacent blocks.

been assigned to the joint surfaces between adjacent blocks. The contact property model describes tangential and normal behaviour. A very large coefficient of friction is adopted to avoid the slipping of a pair of surfaces in the radial direction. Subsequently, along the normal direction, a pressure-overclosure relationship is adopted: the surfaces transmit contact pressure and the slope of the relationship is assumed to be equal to the stiffness of the joint mortar, as described in §4.3.4.

The solid element joint model simulates the joints between the blocks as independent solid elements, Fig. 4.9 c. The joint elements are built splitting the discontinuity surface and spacing the two resulting surfaces at 10cm. This distance is adopted intentionally larger than the mortar joint because it is also intended to represent, by simulating a heavier discontinuity, the interfaces with the adjacent blocks. These thin slices between blocks are characterized by their own mechanical properties, as described in §4.3.4. Then joints and blocks are connected by means of surface-based *tie* constraint, adopting the joint surfaces as “slave” and the block surfaces as “master” because the block mesh is coarser than that of the joint. In this way the nodes on the slave surfaces of joints better follow the sparser nodes of the master surfaces of blocks.

All three models simulate the connections between the bases of the blocks and joints (in the element joint model) and the pulvino foundation by means of surface-based *tie* constraint. In this case, all the base surfaces of joints and blocks are defined as “slave” of the “master” extrados *pulvino* foundation surface due to its coarser mesh (and sparser nodes). Tab. 4.1 summarizes the differences between the three models.

Four-noded trilinear tetrahedral elements C3D4 are used to discretize the concrete structure: *pulvino* foundation, blocks, joints, when they are present, as in the third model, and ancillary works such as weight blocks and stilling basin. Sometimes imprecise geometry does not allow for the import and/or mesh procedures of parts. In these cases, *Geometry Edit* tools can be employed in the *Part* module to restore the validity of the part; if some problems occur in the mesh phase, the *Virtual Topology* tool can be employed in the *Mesh* module to ignore small faces or edges that would be redundant in the numerical analysis and/or that would require a finer mesh. Generally, improving the *Seed* of the whole *Instance*, the majority of the problems related to the geometry can be solved; otherwise, the mesh can be locally improved by means of *Edges Seed*, not increasing the number of the elements elsewhere. If all the previous correction tools fail or the mesh refinement is not suitable, the part can be divided by means of the *Partition* tool in the *Part* module or it can be modified in the previous pre-processing phase in Rhinoceros® and imported again. The element mesh size varies in relation to the object of the analysis: the ancillary works, just reproducing the boundary load conditions, have a coarser mesh than that of the blocks; on the other hand joints, being small slices and interesting the evolution of the damage throughout them, have a finer mesh than that of the blocks. In Tab. 4.2 the mesh characteristics of the solid element joint model are reported: the applied maximum global size, the number and the type of elements for each part. A total of 827431 linear tetrahedral elements characterize the whole solid element joint model with water reservoir close to the normal reservoir level (557.3 m a.s.l.), Fig. 4.10 a and b.

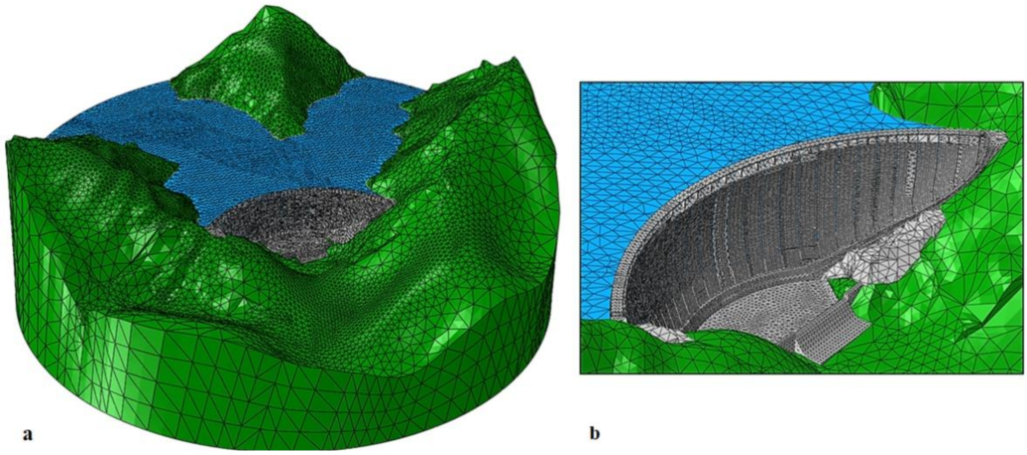

Figure 4.10. The FE model of the Ridracoli dam. a) a general overview; b) a zoom of the dam structure.

Table 4.1. Dam body modelling procedures of the three representations.

Models	**Vertical joints**	***Pulvino* saddle foundation joint**
Monolithic	Surfaces-based *tie* constraint	Surface-based *tie* constraint
Surface-to-surface joints	General-contact interaction with normal and tangential behaviour	Surface-based *tie* constraint
Solid element joints	Solid elements	Surface-based *tie* constraint

Table 4.2. Mesh characteristics of the solid element joint model.

Mesh Instance	**Maximum global size (m)**	**Element number**	**Element type**
Block	5	9925	C3D4
Joint	1	8733	C3D4
Pulvino foundation	20	61779	C3D4
Concrete weight blocks	50	1548	C3D4
Stilling basin	50	1182	C3D4
Rock mass	175	33008	C3D4
Reservoir water 557.3 m a.s.l.	20	79869	AC3D4
Reservoir water 523 m a.s.l.	20	40463	AC3D4

4.3.2 Soil-structure-fluid interaction

In dynamic analysis, the hydrodynamic overpressure effect has to be added to the hydrostatic load. As suggested by literature and reported in §3.5.2, the acoustic water mass can be truncated not so far away from the dam structure, applying no reflecting surfaces at the fluid end. Although this method reduces the computational efforts, it cannot take into account the topographic asymmetry of the valleys, and therefore of the water basin, in the back of the retaining structure. The asymmetric shape of the acting water mass can influence the dynamic response of the dam structure, Fig. 4.11. Therefore a proper extension of the water mass has to be taken into account. Adopting, from literature, 3÷4H, where H is the maximum water height [11], the condition of infinite reservoir is achieved. In the present study, an extension of 5H (5H~500m) is employed: a circle with its centre on the main cantilever at the crown level and with a 500m radius isolates a cylinder of water and rock masses, Fig. 4.5 d. The dimension of the rock mass is therefore related to the infinite reservoir condition, Figs. 4.7 b and c, and it has a minimum thickness, starting from the base structure, of 1.5 times the maximum height of the dam (1.5H~150m). Four-noded linear tetrahedral elements C3D4 and acoustic four-noded linear tetrahedral elements AC3D4 are used to discretize respectively the rock mass and the water reservoir volume. The mesh size in both cases are coarser than that employed to model the dam structure, Tab. 4.2. Although a propter extension of the water mass is adopted, no reflecting surfaces are applied on the far end of the fluid. Moreover, the water reservoir is directly coupled by a surface-based *tie* constraint with the upstream face of the dam structure as well as with the bed rock, without any bottom absorption

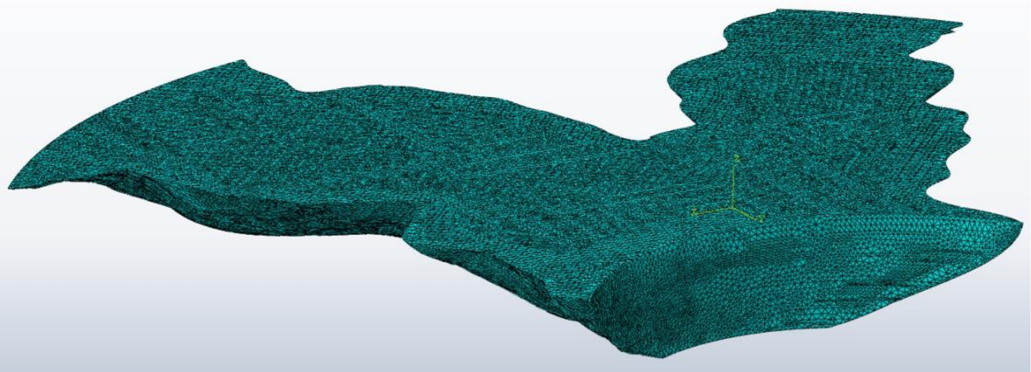

Figure 4.11. The water reservoir meshed part. The asymmetry of the water mass is visible due to the topographic shape of the two upstream valleys.

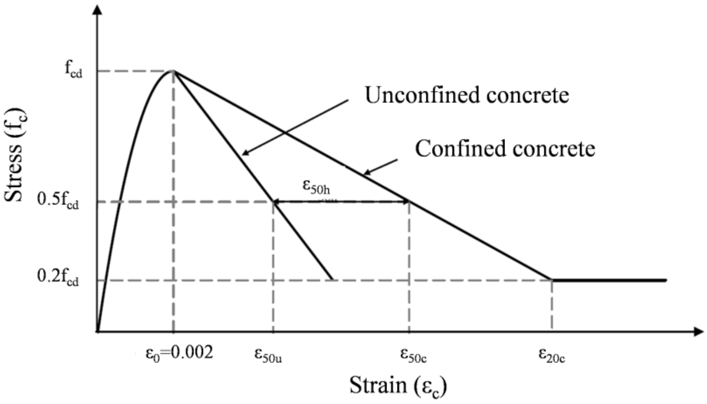

Figure 4.12. Kent and Park model for confined and unconfined concrete [18].

phenomena. Finally, the top of the water reservoir is modelled as a free surface without any sloshing mechanism. The excavation perimeter is created y splitting the base of the *pulvino* foundation; the rock mass and the foundation are directly coupled by means of a surface-based *tie* constraint. The base and the lateral surfaces of the rock mass are restrained in general by fixed constraints.

Table 4.3. Mechanical properties of rock mass, block concrete, joint mortar and water. E_s static elastic modulus, E_d dynamic elastic modulus, E’ drained Young’s modulus, E_u undrained Young’s modulus, G’ drained shear modulus, G_u undrained shear modulus, ν Poisson’s coefficient, ρ bulk density, B bulk modulus and ζ damping ratio [16,15,17].

	Rock Mass	Concrete of blocks	Mortar of joints	Water
E_s (kPa)	-	$3.07 \cdot 10^7$	$2.20 \cdot 10^7$	-
E_d (kPa)	-	$3.70 \cdot 10^7$	$2.65 \cdot 10^7$	-
E' (kPa)	$4.80 \cdot 10^7$	-	-	-
E_u (kPa)	$2.17 \cdot 10^7$	-	-	-
G' (kPa)	$1.92 \cdot 10^7$	-	-	-
G_u (kPa)	$8.70 \cdot 10^6$	-	-	-
ν	0.25	0.20	0.20	-
ρ (t/m^3)	2.635	2.470	2.100	1.000
B (kPa)	-	-	-	$2.15 \cdot 10^6$
ζ	0.05	0.02	0.02	-

4.3.3 Material properties and constitutive modelling

The mechanical proprieties of the concrete of the structure and of the rock mass are taken from the technical reports and specific site investigations, Tab. 4.3. The static elastic modulus E_s of the concrete blocks is derived by the arithmetic mean of the values acquired by means of compression tests of

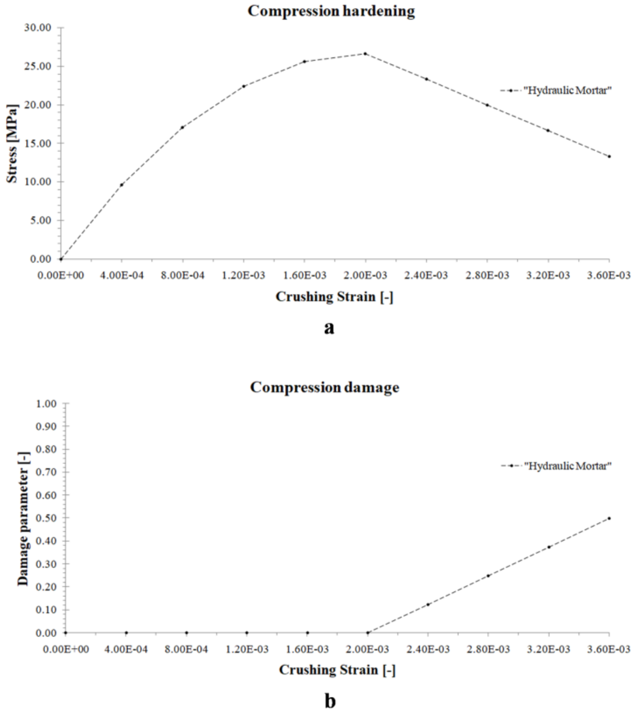

Figure 4.13. Compressive behaviour of the hydraulic mortar of the joints. a) Compression stress-strain relationship; b) compression damage evolution.

concrete specimens. In dynamic analyses, a dynamic modulus of elasticity E_d greater than the static one is used [12,13,14], $E_s = 0.83E_d$.

As for the rock mass properties, a large site investigation has been conducted in the dam area, including plate loading tests in exploratory tunnels and a series of geophysical investigations, aimed at measuring the compression and shear wave velocities of the rock [15,16]. Starting from these compression wave velocities V_p, by means of the theory of elasticity, introduced in §3.6, Oedometric Constrained modulus E_{oed} is achieved and, from this, Young's modulus E and shear modulus G, for drained and undrained conditions, can be obtained, Tab. 4.3. In the analyses an average value between the drained and undrained moduli is assumed, the water content of the soil being unknown.

In general, for static and dynamic (also modal) analyses, linear elastic homogeneous isotropic materials are employed, specifying for each of them the static or dynamic Young's modulus and Poisson's coefficient. The solid element joints FEM model is adopted for elasto-plastic damage dynamic analyses. In this case, the non-linearity is included in the joints material. The

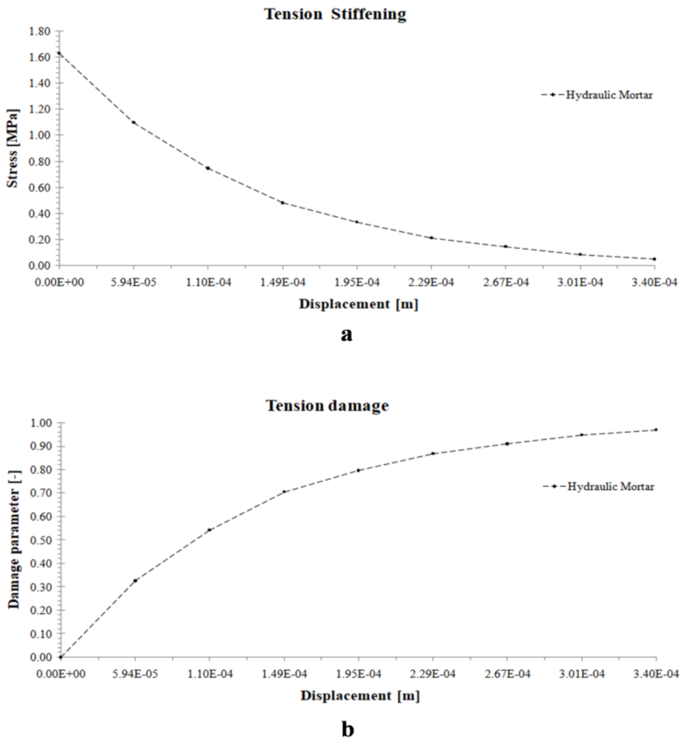

Figure 4.14. Tensile behaviour of the hydraulic mortar of the joints. a) Tensile stress-displacement relationship; b) tension damage evolution.

entire model has a linear elastic behaviour while the hydraulic mortar of the joint elements is modelled by means of a CDP – Concrete Damage Plasticity – model. The mechanical characteristics of the hydraulic mortar are derived from technical datasheets of the materials usually employed for the injection of joints. The adopted compression behaviour, function of cylinder concrete design compressive stress f_{cd} , is defined by Kent and Park, 1971 [18]. This stress-strain relationship is develo ped for confined concrete, but the equation of the ascending branch is equal for confined and unconfined concrete,

instead of it differs for the descending branch, Fig. 4.12. The pre-peak behaviour is described by,

$$f_c = f_{cd}\left[\frac{2\varepsilon_c}{\varepsilon_{c0}} - \left(\frac{\varepsilon_c}{\varepsilon_{c0}}\right)^2\right], \tag{2}$$

where ε_{c0} =0.002. In the present study, dealing with unconfined concrete, a linearly descending branch is adopted from the peak stress f_{cd} to the maximum compressive strain ε_{cu} , Fig. 4.13 a. The concrete compression damage, as explained in §3.6, is defined as,

$$d_c = 1 - \frac{f_c}{f_{cd}}, \tag{3}$$

where f_c is the generic compressive stress value of the descending branch, Fig. 4.13 b. The tensile behaviour of the hydraulic mortar of joints is derived from the existing data of a concrete gravity dam [19].

The values of tensile stress are linearly scaled, applying a proportion, for the tensile design strength f_{ctd} of the hydraulic mortar of joints, Fig. 4.14 a. As recalled in §3.6, Hillerborg's criterion is adopted to describe the tensile behaviour: a stress-displacement response rather than a stress-strain response is adopted. This method reduces the mesh sensitivity of the results in structures with no reinforcement such as simple concrete arch, gravity or arch-gravity dams. The concrete tensile damage, as explained in §3.6, is defined as,

$$d_t = 1 - \frac{f_{ct}}{f_{ctd}}, \tag{4}$$

where f_{ct} is the generic tensile stress value of the descending branch, Fig. 4.14 b.

The CDP model requires the definition of some parameters which identify the shape of the flow of the potential surface and the yield surface, introduced in §3.6.1. The parameters β_d, the dilatation angle, and m, the eccentricity, describe the shape of the flow potential function; instead the parameters f_y, defined as the ratio of biaxial compressive yield stress to uniaxial compressive yield stress, and K_I, defined as the ratio of the second stress invariant on the tensile meridian to that on the compressive meridian for the yield function, describe the shape of the yield function. Moreover, some additional parameters can be specified such as the viscosity parameter μ_P. This is used for the visco-plastic regularization of the concrete constitutive equations but it can affect the results. The identification of the constitutive parameters of the CDP model requires the following laboratory tests: the uniaxial compression, the uniaxial tension, the biaxial failure in plane state of stress and the traxial test of concrete. Therefore in the present work the parameters are derived from suggestions offered in scientific literature [20,21], Tab. 4.4.

Tab. 4.4. Parameters of the CDP model.

CDP parameters				
Dilatation Angle β_d	Eccentricity m	f_y	K_I	Viscosity parameter μ_P
35	0.1	1.16	0.667	0.01

4.4 Seismic input

The dynamic calibration of the solid element joint FEM model, described in detail in the following §5.2 and §5.3, is based on real recorded seismic time-histories. As already mentioned, a seismic event, to be considered significant for the Ridracoli dam structure, has to shake the dam crest with at least 0.2 m/s^2 acceleration. From the list of significant seismic events which have occurred on the structure, two of them are employed in the following calibration procedures, Tab. 4.5. The accelerograms of the free-field motions, recorded in position A, of the motions at the base of the structure, acquired in position D, and of the responses of the dam, measured in position C, are reported in the Appendices 4.1 and 4.2 for the events which occurred on 26/01/2003 and on 04/06/2011 respectively.

Tab. 4.5. Two real recorded seismic time-histories which occurred at the Ridracoli site on 26/01/2003 and 04/06/2011.

Real recorded seismic time-histories adopted for the FEM calibration		
Date	26/01/2003	04/06/2011
Time GTM	19:57:03.2	18:06:50
Hydrostatic level [m a.s.l.]	557.3	551.8
Duration [s]	-	24.5
Lat. N. [°]	43.88	43.89
Long. E [°]	11.96	11.98
Depth [km]	6.5	9.2
M_L [-]	4.3	3.3
Epicentre	Spinello (FC)	Bagno di Romagna (FC)
Distance from the dam [km]	10	11.7
Maximum upstream-downstream crest acceleration [m/s^2]	0.357	0.305

In order to perform elasto-plastic damage time-history analyses, strong seismic events have to be applied on the structure. As already mentioned in §3.5.3, the Italian regulation NTC2008 – Technical Construction Normative – D.M. 14/01/2008, in accordance with the European, Eurocode 8, permits the use of suitable sets of seven real seismic time-history records. The selection of such groups of events has to be performed on the basis of their matching the target design spectrum of the site. This procedure can be performed by REXELite application, which automatically builds code spectra for any limit state according to the previous mentioned regulations [22,23]. It finds the sets of seven records having the most similar spectral shape compared to that of the code, and whose average also matches the target spectrum in a specified period range and with the desired tolerance.

The target spectrum is built as a function of the site position (Latitude and Longitude), the EC8 site classification (A, B, C, D, and E), the topography (T1, T2, T3, and T4), the aim of the structure (Nominal life and C_U) and of the limit state probability (SLO, SLD, SLV, and SLC). The records are extracted according to specific features, in terms of magnitude (M_L or M_W), epicentral distance and focal mechanism. Some spectrum matching parameters can be specified, such as the tolerance and the range period in which to perform the comparison. Finally, unscaled (original) or amplitude-scaled records can be chosen. In this last case, the seismic acceleration time-history vectors have to be multiplied for the provided scale factor in order to adapt the motions to the specific site.

Imposing the characteristics of the Ridracoli site, specifying the reference period V_R for strategic structures (V_R=200 years) and a limit state probability for the Collapse Limite State (5%), to which is associated a return period T_R for strategic dams of 2475 years, and a local magnitude between 5.5 and 7, REXELite provides seven groups (two horizontal components) of suitable earthquakes that occurred in central Italy, Tab. 4.6. In order to have a larger amount of available records, the selection is performed on spectrum-matching sets of records which are ground motions linearly scaled in amplitude. Fig. 4.15. shows the spectra comparison: in green the target spectrum with the upper and lower tolerances, in red and blue respectively, and the other 14 spectra (two for each event, one for each horizontal direction) of the real seismic time-history records. The seismic event that occurred in Accumoli (RI) on

30/10/2016 is employed for the elasto-plastic damage time-history anlyses in §5.4. Indeed, the scale factor of these events is the closest to the unit and its accelerogram time-histories do not have to be extremely distorted. The three components (East-West, North-South and up-down) of the selected seismic event are reported in Appendices 4.3.

Tab. 4.6. Combination of seven strong motion records, provided by REXELite, compatible in average with the target spectrum of Ridracoli [22,23].

Station Place	Event time	Scale factor	Max PGA [m/s^2]	Duration [s]	M_L
Leonessa (RI)	24/08/2016 01:36:32	N-S: 17.560 E-W: 14.473	0.23	80.0	6
Accumoli (RI)	30/10/2016 06:40:18	N-S: 0.867 E-W: 0.778	5.47	60.0	6.1
Montemonaco (AP)	30/10/2016 06:40:18	N-S: 1.791 E-W: 1.790	1.85	60.0	6.1
Baregnano (MC)	30/10/2016 06:40:18	N-S: 1.314 E-W: 1.423	2.52	193.4	6.1
Auletta (SA)	23/11/1980 18:34:53	N-S: 6.056 E-W: 5.910	0.56	66.49	6.5
Bisaccia (AV)	23/11/1980 18:34:53	N-S: 3.524 E-W: 4.114	0.95	76.21	6.5
Viggianello (PZ)	09/09/1998 11:28:00	N-S: 4.623 E-W: 4.825	0.72	21.62	5.5

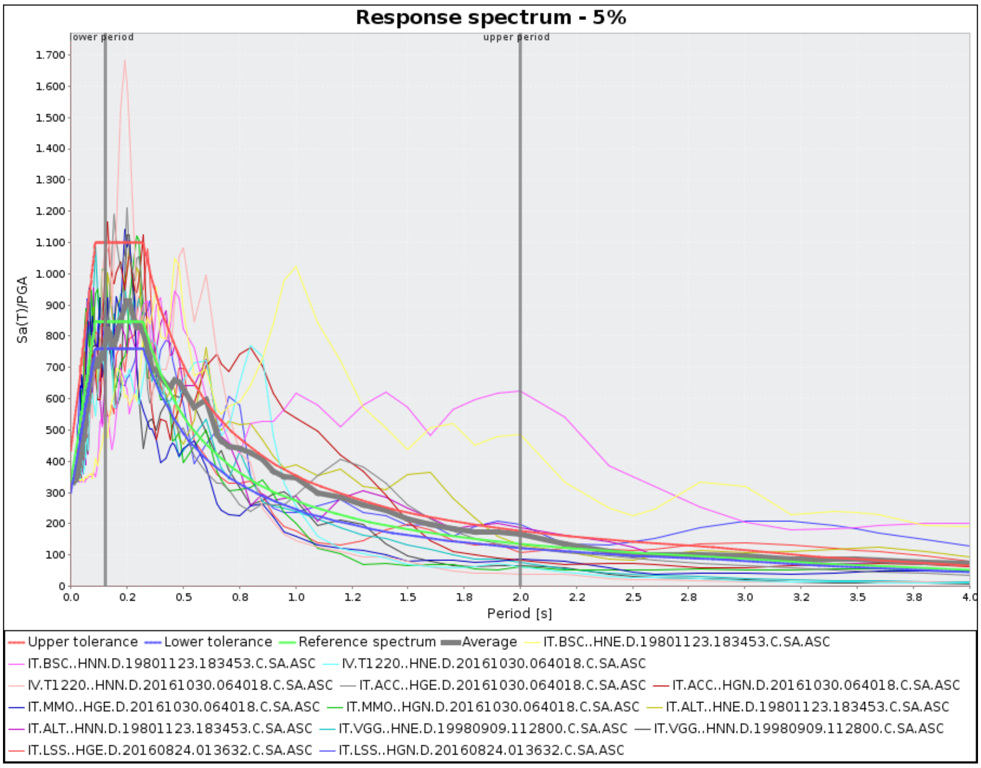

Fig. 4.15. Collapse State Limit Spectra (5%) comparison: in green the target spectrum, with the upper and lower tolerances, in red and blue respectively, and the other 14 spectra (two horizontal components for each event) of the suitable real seismic time-history records.

4.5 Chapter bibliography

[1] ICOLD, "Buletin 30 - Finite elements methods in analysis and design of dams", 1978.

[2] ICOLD, "Bulletin 52 - Earthquake analysis for dams", 1986.

[3] ICOLD, "Bulletin 94 - Computer software for dams - Validation Comments and proposals", 1994.

[4] ICOLD, "Bulletin 122 - Computational procedures for dam engineering - Reliability and applicability", 2001.

[5] ICOLD, "Bulletin 155 - GUIDELINES FOR USE OF NUMERICAL MODELS IN DAM ENGINEERING", ICOLD, 2013.

[6] Consorzio Acque Forlì Ravenna, "Diga di Ridracoli [The Ridracoli dam]," Alpina S.p.A., 1985.

[7] Bavestrello F., Gallico A. Piccinelli F., "Ridracoli dam: test and data acquisition.", 15th ICOLD Congress, Lausanne, Switzerland, 1985, pp. 1415-1438.

[8] A. Piccinelli, F., Bavestrello, F., Gallico, "Ridracoli dam: test and data acquisition", 15th ICOLD Congress, Lausanne, Switzerland, 1985.

[9] Salvaneschi P. Lazzari M., "Improved Monitoring and surveillance through integration of artificial intelligence and information management system.", 10th IEEE Conference on Artificial Intelligence for Applications, San Antonio, Texas, 1994.

[10] Simone Tarquini et al., "Release of a 10-m-resolution DEM for the Italian territory: Comparison with global-coverage DEMs and anaglyph-mode exploration via the web", *Computers & Geosciences*, vol. 38, no. 1, pp. 168-170, Jan. 2012.

[11] Bari Sevim et al., "Water Length and Height Effects on the Earthquake Behavior of Arch Dam-Reservoir-Foundation Systems", *KSCE Journal of Civil Engineering*, vol. 15, no. 2, pp. 295-303, 2011.

[12] Adam M Neville, "Properties of concrete", Longman London, 1995.

[13] "British Code for design of concrete structures BS CP 110:1972" 1972.

[14] R.V. Lydon, F.D., Balendran, "Some observations on elastic properties of plain concrete", *Cement and Concrete Research*, vol. 16, no. 3, pp. 314-

324, May 1986.

[15] G. Oberti, F. Bavestrello, P. P. Rossi, and F. Flamigni, "Rock mechanics investigations, design and construction of the Ridracoli dam", *Rock Mechanics and Rock Engineering*, vol. 19, no. 3, pp. 113-142, 1986.

[16] R. Grandori, A. Lembo-Fazio, and R. Ribacchi, "Excavation of the ridracoli hydraulic tunnels using a double-shield TBM", *Rock Mechanics and Rock Engineering*, vol. 23, no. 3, pp. 141-165, 1990.

[17] MAPEGROUT BM, technical schedule | Mapei. [Online]. http://www.mapei.com/it/it/prodotti-e-soluzioni/prodotti/dettaglio/mapegrout-bm

[18] D C Kent and R Park, "Flexural members with confined concrete", *Journal of the Structural Division*, July 1971.

[19] Abaqus 6.10. (2010) Seismic analysis of a concrete gravity dam. [Online]. http://abaqusdoc.ucalgary.ca/books/exa/default.htm?startat=ch02s01aex74.html

[20] Tomasz Jankowiak and Tomasz Àodygowski, "Identification of parameters of concrete damage plasticity constitutive model", Foundation of civil and environmental engineering, 2005.

[21] Szczecina Michał and Winnicki Andrzej, "Calibration of the CDP model parameters in Abaqus", Congress on Adavances in Structural Engineering and Mechanics, Korea, Aug. 2015.

[22] Iunio Iervolino, Carmine Galasso, Roberto Paolucci, and Francesca Pacor, "Engineering ground motion record selection in the ITalian ACcelerometric Archive", *Bull Earthquake Eng*, vol. 9, pp. 1761-1778, 2011.

[23] Iunio Iervolino, Carmine Galasso, and Edoardo Cosenza, "REXEL: computer aided record selection for code-based seismic structural analysis", *Bulletin of Earthquake Engineering*, vol. 8, no. 2, pp. 339-362, Apr. 2010.

5. Numerical analyses: calibration procedures, vertical joint modelling influence and earthquake safety assessment

Numerical analyses have become the tools of knowledge of the behaviour of large structures such as dams. A prompter choice of parameters and a validation of the overall functionality of the model are primary aspects for the correct simulation of the reality. In this field, as well as a detailed reproduction of geometries, accurate calibrations of static and dynamic parameters and comparisons of simulated quantities with the real ones are required to obtain a reliable FEM model of the structure. In this chapter, linear elastic static analyses of the whole model are performed in order to validate the behaviour of the structure under static *cause* quantities, hydrostatic level and temperature; subsequently, dynamic properties are acquired by means of modal analyses: the influence of vertical joint modelling is investigated. The results are useful for the subsequent calibration of the damping parameters of the rock mass and of the concrete of the structure. Finally, the tested FEM model is employed for an earthquake safety assessment of the structure undergoing a strong design SLC earthquake which has a spectrum compatible with the target spectrum evaluated for the site of Ridracoli. All the subsequent analyses are carried out adopting the solid element joint model.

5.1 Linear elastic static simulations

To evaluate the static behaviour of the FEM model, the *cause* quantities, hydrostatic level and temperature, are applied, together with the gravity load, to perform a linear elastic static analysis of the structure. The *effect* quantity, the displacement of the crest of the dam at the central section, is acquired by the direct plumb line. It measures the two planimetric components (upstream-downstream and left-right) of the displacement of the dam body with respect to the dam foundation. Such displacement is related to seasonal changes in the hydrostatic level and in the air/concrete temperature: the regime of dams located in the Apennines generally presents an increase in hydrostatic level during the winter/spring and a decrease during the summer period due to seasonal water requirements. Therefore, to quantify the effect of such actions on the structure, the water level and concrete temperature conditions on two days in different seasons are taken into account: 30/04/2014 (hydrostatic level: 556.22 m a.s.l. and concrete temperature:11.4°), the day, at the end of spring, after which the hydrostatic level started to decrease; and 31/10/2014 (hydrostatic level: 528.94 m a.s.l. and concrete temperature: 14.7°), when the minimum water level of 2014 was reached. The consequent variation of the dam crest position, provided by the direct plumb line along the upstream-downstream direction, is Δd_y=0.025m. To test the overall static functionality of the FEM model, two *steps* are applied, that simulate the water level/constant concrete temperature conditions on the two days, as described in §3.4.2 and §3.4.3. Moreover, the gravity load is also included in relation to the densities of the model materials, as reported in Tab. 4.3 (Chapt. 4). At the base and on the lateral surfaces of the rock mass are applied fixed boundary conditions.

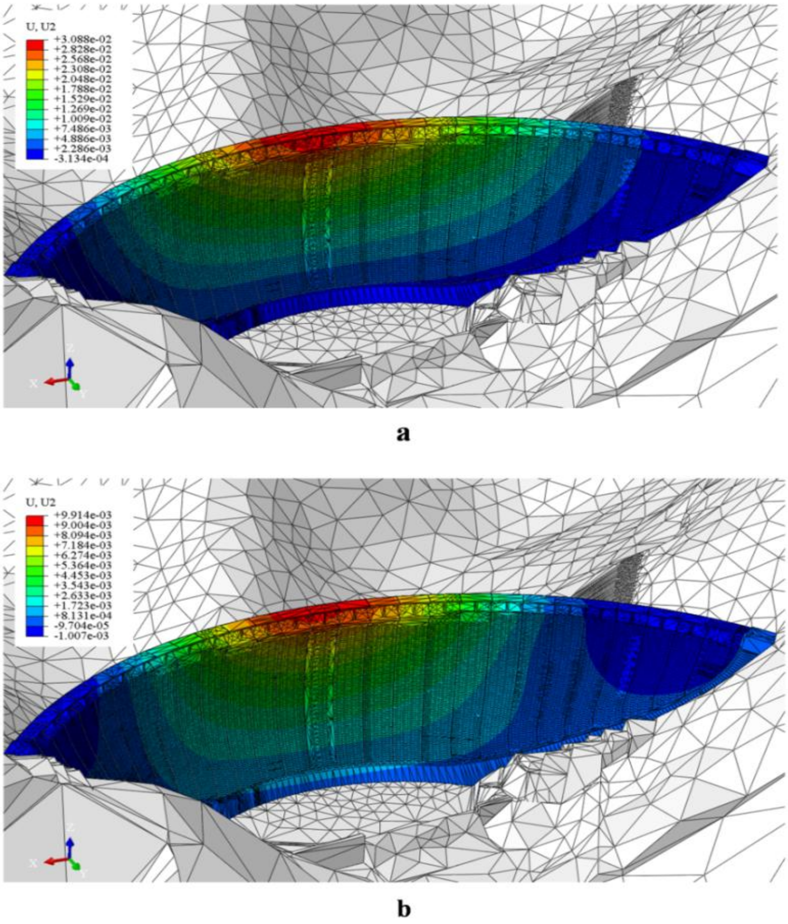

Fig. 5.1. Linear elastic static analysis with gravity load, hydrostatic level and concrete constant temperature: upstream-downstream U2 displacement distribution. a) first *step*: h.l. 556.22m a.s.l. and c.t. 11.4°; b) second *step*: h.l. 528.94m a.s.l. and c.t. 14.7°.

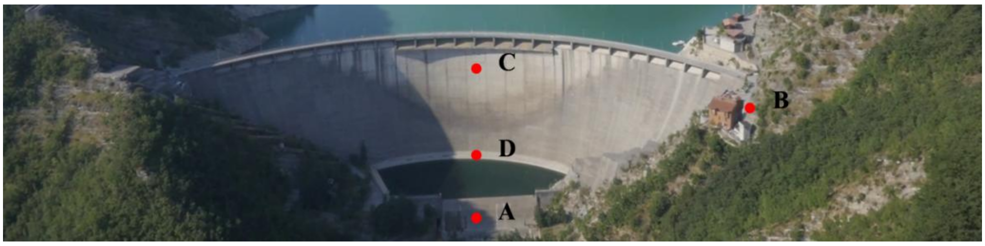

Fig. 5.2. The Ridracoli dam: accelerometers positions. In red the accelerometer positions.

The results of the analysis are expressed in terms of displacement distribution. The upstream-downstream displacement U2 distribution is shown after the application of the first and second steps respectively, Fig. 5.1 a and b. The evaluated displacement variation of the crown of the dam at the central section is Δd_y=0.021m. The value is very close to that provided in reality by the direct pendulum evaluated previously. This result shows, therefore, the overall reliability of the FEM model in static simulations.

5.2 Dynamic properties and modal analysis

The dynamic structural identification of real structures can be performed using excitation techniques. The modalities can be different, the most reliable consists in the application of vibrators on the structure (Non-balanced rotating masses, hydraulic pistons). The Ridracoli dam was tested with the vibrodyne in 1987, after its construction phase. This procedure allows the generation of forces adjustable in both frequency and amplitude. The hydrostatic level during the test was 551.8m a.s.l., close to the normal reservoir level (557.3m a.s.l.). The response of the structure was acquired by seismometers applied in different sections and elevations on the dam body. A different, cheaper excitation source is represented by environmental vibrations. In this case the signals can be influenced by noises and some corrections are needed. For the comparison the seismic event of June 2011, during which the reservoir level was at 551.8m a.s.l., is also considered, as described in §4.4. The response of the structure is acquired by the accelerometer placed near the dam crest in position C, as shown in Fig. 5.2 (the same as Figure 4.3 in Chapter 4 but here reported for clarity). Introducing the Power Spectral Density function, which describes the signal power distribution in the frequency domain, the experimental natural frequencies of the structure can be obtained as the peaks of the curve, Fig. 5.3. Moreover, modal analyses of FEM models may also provide dynamic

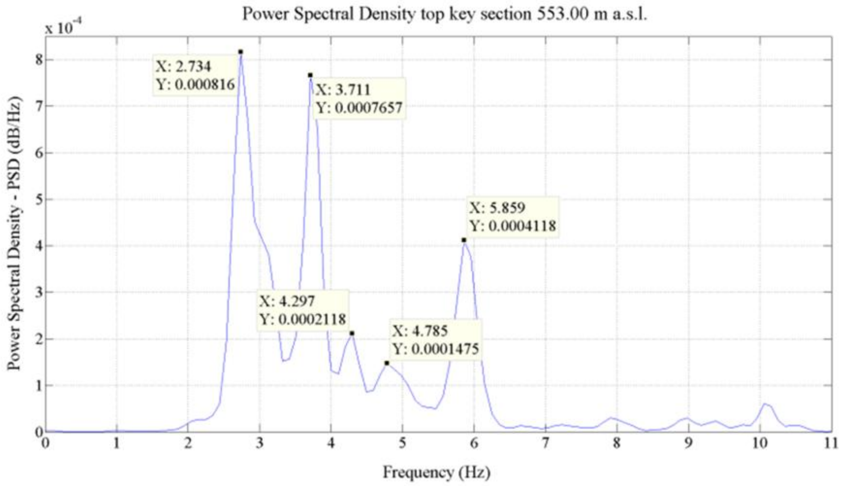

Fig. 5.3. PSD – Power Spectral Density – function of the recorded signal on the crest of the dam on June 2011.

proprieties of the structure, in terms of natural frequencies and vibration modes. Therefore, a modal analysis of the monolithic FEM model of the Ridracoli dam is performed beforehand. As shown in Fig. 5.4, the natural frequencies extracted by the vibrodyne test (blue columns) and by the FEM monolithic model (red columns) are similar, except for the higher modes (8,9,10) on which the fluid vibration effect is elevated and not distinguishable through the vibrodyne excitation. It might also be noted that the natural frequencies provided by the PSD function (green columns) are only partly identified. This is due to the signal noise, the reduced structure acceleration related to the selected seismic event and probably to the accelerometer position, on the key cantilever close to the dam crowing.

5.2.1 Influence of joint modelling on the dynamic properties of the structure

As already explained in §4.3.1 and earlier in §3.7, several authors deal with vertical joint modelling, although their main aim is to test a single modelling procedure, often employing a reduced detailed model in terms of prompter rock mass extension and fluid-structure interaction. Therefore, in the present study, three models of the same structure are proposed: monolithic, surface-to-surface joint and solid element joint representations. In order to compare their behaviour in terms of dynamic properties, modal analyses are also performed on the surface-to-surface joint FEM model and on the solid element joint FEM model.

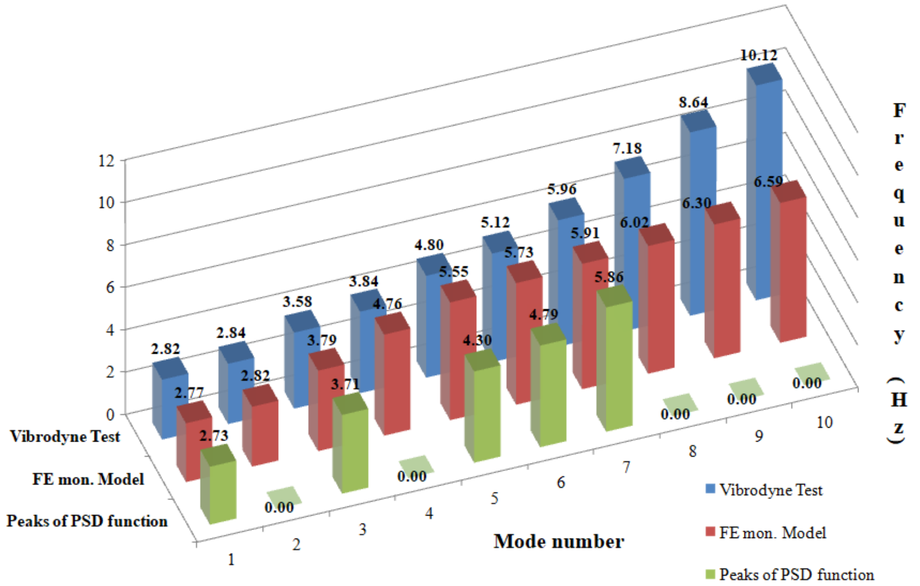

Fig. 5.4. Natural frequencies of the dam structure derived from the vibrodyne test (blue column), from the finite element monolithic model (red column) and from the power spectral density function (green column).

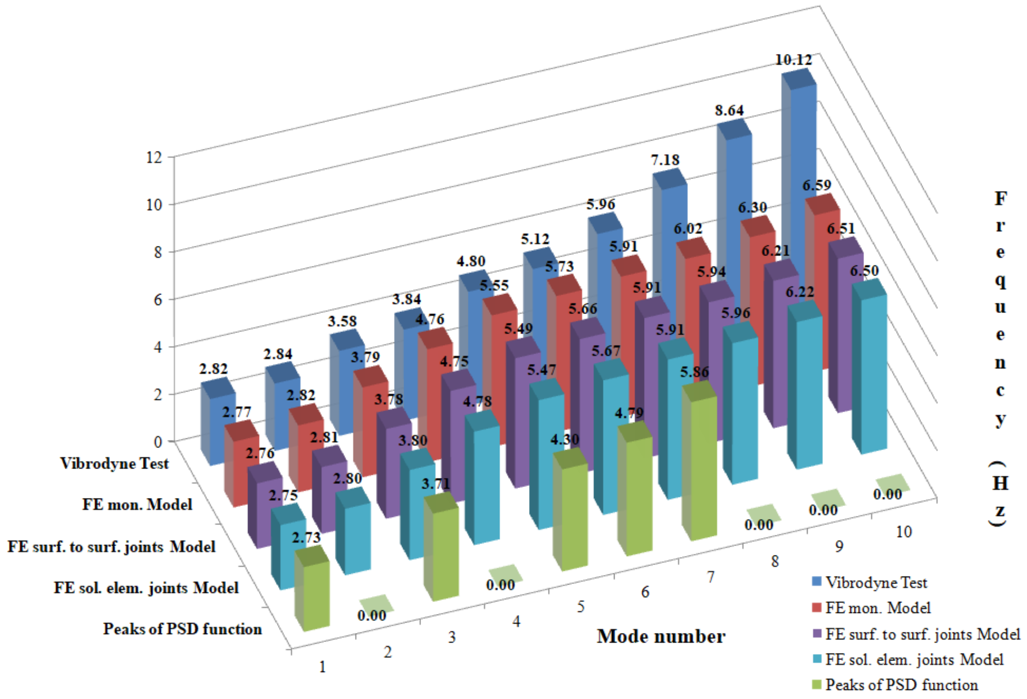

Fig. 5.5. Natural frequencies of the Ridracoli dam derived from vibrodyne test, FE models (monolithic, surface-to-surface joint and solid element joint representations) and environmental vibrations (peaks of PSD function).

The analyses are carried out including the same hydrostatic level of the experimental tests of 551.8m a.s.l.. The comparison of the three FEM representations with the experimental results is performed in terms of natural frequencies and mode shapes. The FEM model results (red, purple and light blue columns) provide similar values of natural frequencies, Fig 5.5. Passing from the monolithic to the surface-to-surface joint, and to the solid element joint representations, the stiffness of the structure decreases progressively. Therefore, also the natural frequencies of the three models tend to decrease with the same trend, moving closer to the peaks of the PSD function. As expected, the modal analyses of the three FEM models provide the same deformed shapes, given that the reduction of the stiffness is not sufficient to cause a change in the deformed shapes, and they also fit with those provided by the vibrodyne tests, Fig. 5.6.

5.2.2 Results

All the results provided by the FEM models are in line with the experimental ones, as already noted, a larger gap is more evident only for the higher modes on which the influence of the fluid mass is more significant. The stiffness of the modelled structure tends to decrease when adopting more detailed joints representations, and the natural frequencies of the different representations also tend to decrease and to approach the values extracted from the PSD function. An accurate joints representation, such as that provided by the solid element joints model, reproduces reality better than more simplified procedures. However, the differences in terms of natural frequencies between the models are minimal, Fig.5.5. The average percentiles of the gap in terms of natural frequencies are: 0.75% between the monolithic m. and the surface-to-surface joint m., 0.82% between the monolithic m. and the solid element joint m., 0.31% between the surface-to-surface joint m. and the solid element joint m.. This gap could be crucial if the study deals with the monitoring of the state of conservation of a structure. In such cases, an accurate evaluation of the natural frequencies is required to detect any small change in the behaviour of the structure, employing the FEM model for a parametric study of the mechanical characteristics of the materials. Moreover, if the aim of the analyses is the inspection of damage in the joints, independent elements with their own mechanical properties and degradation models allow us to detect the evolution

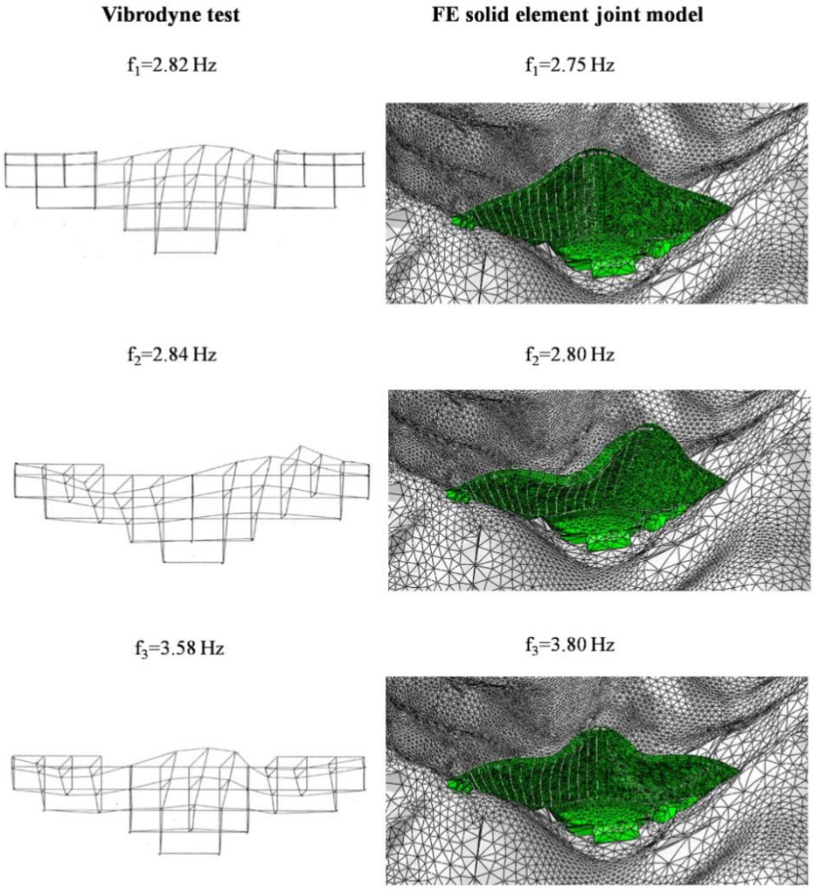

Fig. 5.6. First three mode shapes of the Ridracoli dam derived from vibrodyne test and FE solid element joint model including the water level effect (hidden in the representation).

of damage under severe seismic events. On the other hand, a sophisticated model, such as that with solid elements like joints, requires important pre-processing work-time and computational costs in relation to the type of analyses required. Furthermore, if the goal is to analyse the general response of the structure under seismic events, joint modelling does not substantially influence global behaviour and simplified models such as the monolithic one can be employed. Indeed, the mode shapes of the three FEM models are equal, fitting also with the ones provided by the vibrodyne test; furthermore, the joints representation does not influence the global dynamic behaviour of the structure.

5.3 Linear dynamic elastic analysis

Depending on the constitutive models adopted for the dam and foundation rock materials, a key aspect in such a modelling task is typically represented by the appropriate selection of Rayleigh damping coefficients. Indeed, their values may significantly affect the results in terms of seismic performance indicators (i.e. amplitude of accelerations, velocities and displacements as well as response spectra at suitable control points). The parameter identification should concern both the structure, seen as a deformable body and the rock mass at the dam foundation. Indeed, ignoring the deformability of the rock mass in the dynamic analysis could result in significant overestimation of dam stresses [1,2]. Some recommendations about the critical damping percentage of dam systems are available in literature [3,4,5]. In particular, values of critical damping ratios in the range between 1-7% and 5-20% have been suggested for concrete structures and rock masses, respectively [3,4]. However, these literature references provide only general indications, which may not be adequate for a specific dam. The present study intends to provide, in this section, an operative procedure to estimate separately viscous damping parameters for the rock mass and for the structure of a dam-foundation rock-reservoir water system, including water-structure interaction effects. To this purpose, modal analyses of two systems are employed, i.e., a rock mass model and a complete model with mass less rock. Adopting Rayleigh damping formulation, the provided natural frequencies allow for the evaluation, for different critical damping percentages, of the damping parameters for the two systems. The rock mass model is tested first, varying the aforementioned damping parameters, under a real earthquake record by means of dynamic linear elastic analysis. Subsequently, the same procedure is repeated on the complete model, including rock mass and fluid-structure interaction. The signals are compared in terms of accelerograms and response spectra by effective accelerations (RMS – root mean square – accelerations) and Housner Spectrum Intensities, respectively, as described in §3.5.3.

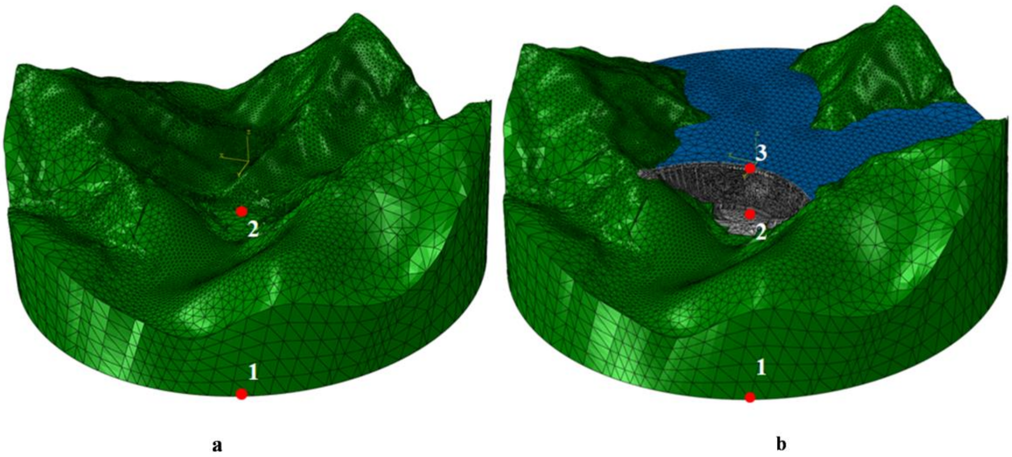

Fig. 5.7. FE model of the Ridracoli dam, in red the seismic application point (1) and the seismic response acquisition points (2,3). a) rock mass model; b) complete model.

5.3.1 Calibration of rock mass damping parameters

The finite element model of the rock mass is rigidly constrained at the base and at the vertical cylindrical external boundary, Fig. 5.7 a. The mechanical characteristics of the rock are reported in Tab. 4.3 (Chapt. 4). In this phase of the calibration procedure, rock density is taken into account. A modal analysis of the system provides the natural frequencies and, starting from these, the coefficients α and β can be derived for different values of damping ratio ζ, as explained in §3.1.4, Tab. 5.1. In order to minimize the total errors on the other modes, the frequencies of the first and the second modes are employed in the evaluation. After that, linear elastic dynamic analyses of the rock mass finite element model are performed for each of the five pairs of values α and β, corresponding to different damping ratios. The seismic free-field motion, as previously mentioned in §4.4, recorded on 26/01/2003 at the A position, Fig. 5.2, is uniformly applied at the base area of the FEM model along the upstream-downstream direction in position 1, Fig. 5.7 a. The simulated motion extracted at position 2, Fig. 5.7 a, is compared with the real one recorded by means of an accelerometer placed in position D, Fig. 5.2. An extract of the real motion and the simulated ones in terms of the accelerations time-history, for different values of damping ratio, is reported in Fig. 5.8. Moreover, in Fig. 5.9 the spectral accelerations S_A for the same signals are plotted. A damping ratio of 5% (α=0.1780 and β=0.0140) allows the best accordance between the simulated response signal at the ground level and the recorded one. A quantitative comparison is provided by the effective acceleration and by the Spectrum Intensity of Housner, Tab. 5.2. Both parameters agree that the best damping ratio for the rock mass finite element representation is 0.05. A further dynamic analysis is performed applying at the base area of the rock mass model the seismic input of the earthquake that occurred on 04/06/2011. Tab. 5.3 confirms the accordance in terms of effective acceleration and Spectrum Intensity of Housner of the ground level record and the simulated signal with a damping ratio of 0.05.

Tab. 5.1. Modal analysis results of the rock mass FEM model.

Rock mass finite element model				
Frequencies		**Damping parameters**		
mode	***f* (1/s)**	**ζ**	**α (1/s)**	**β (s)**
1	3.49	0.05	0.1780	0.0140
2	3.63	0.06	0.2136	0.0168
3	3.80	0.07	0.2492	0.0197
4	4.21	0.08	0.2848	0.0225
5	4.23	0.09	0.3204	0.0253
6	4.39			
7	4.50			

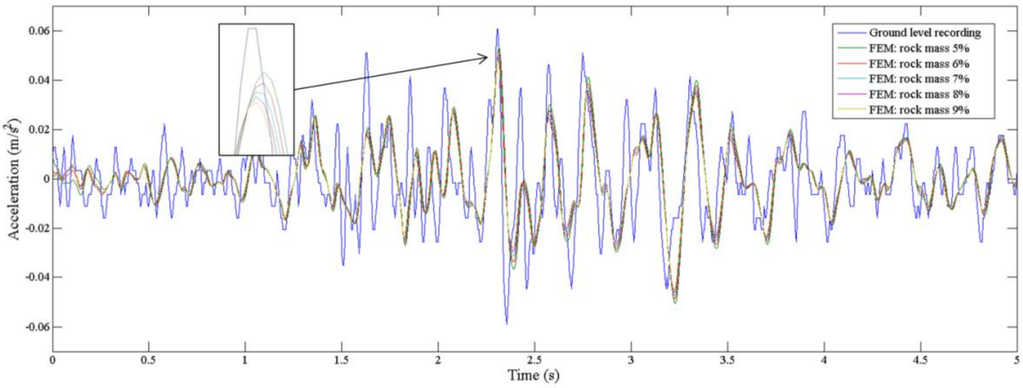

Fig. 5.8. Accelerograms of the ground level record (26/01/2003), acquired at position D, and of the simulated signals for different damping ratios (5%, 6%, 7%, 8%, 9%).

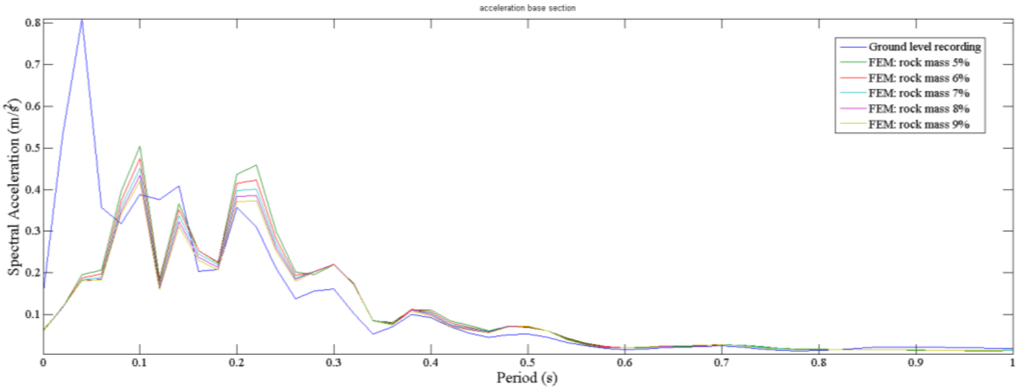

Fig. 5.9. Spectral response accelerations of the ground level record (26/01/2003), acquired at position D, and of the simulated signals for different damping ratios (5%, 6%, 7%, 8%, 9%).

Tab. 5.2. Effective accelerations a_{RMS} and Spectrum Intensity of Housner I_H of the ground level record (26/01/2003) and of the simulated signals for different damping ratios (5%, 6%, 7%, 8%, 9%).

Rock mass finite element model						
	Record	**0.05**	**0.06**	**0.07**	**0.08**	**0.09**
a_{RMS}(m/s^2)	0.0155	0.0137	0.0131	0.0126	0.0123	0.0119
I_H (m)	0.0124	0.0096	0.0093	0.0092	0.0090	0.0089

Tab. 5.3. Effective accelerations a_{RMS} and Spectrum Intensity of Housner I_H of the ground level record (04/06/2011) and of the simulated signal for 0.05 of damping ratio.

Rock mass finite element model		
	Record	**0.05**
$\mathbf{a_{RMS}(m/s^2)}$	0.0045	0.0052
$\mathbf{I_H}$ **(m)**	0.0042	0.0044

5.3.2 Calibration of structure damping parameters

The natural frequencies of the dam structure, composed of the dam body and the foundation, are evaluated by means of a modal analysis performed on an FEM model of the dam-foundation rock structure, considering the rock as a massless material and assuming an empty reservoir. This allows us to extract the dynamic properties of the dam structure alone, yet including the effects of the rock mass deformability. The mechanical characteristics of the concrete and of the rock are reported in Tab. 4.3 (Chapt. 4). Starting from the natural frequencies, the α and β coefficients can be derived for different values of damping ratio ζ, as explained in §3.1.4, Tab. 5.4. In order to minimize the total damping errors on the other modes, the frequencies of the first and the fourth modes are employed in the evaluation. After that, linear elastic dynamic analyses of the complete dam system FEM model are performed for each of the three pairs of values α and β, corresponding to different damping ratio of the concrete of the structure, Tab. 5.4. The rock mass is taken into account with a damping ratio equal to 0.05, as previously calibrated. The fluid-structure interaction is included by means of acoustic elements. The same water level of 557.3m a.s.l., present at the time that the earthquake occurred (26/01/2003), is simulated into the dynamic analyses. Applying the seismic input motion at the base area of the model at position 1, Fig. 5.7 b, the simulated structure responses acquired at position 3 are compared with the real record measured by the accelerometer located in position C, Fig. 5.2. An extract is reported in Fig. 5.10, including the maximum acceleration time-history peak of the real motion and the simulated ones in terms of accelerations time-history along the upstream-downstream direction, for different values of damping ratio. Moreover, in Fig. 5.11 the spectral accelerations S_A for the same signals are plotted. A critical damping fraction of 2% (α=0.0820 and β=0.0046) allows the best accordance between the simulated response signal at the crowning level and the recorded one. A quantitative comparison is provided by the effective acceleration and by the Spectrum Intensity of Housner, Tab. 5.5. Both parameters agree that the best critical damping fraction for the concrete of the structure is 0.02. A further dynamic analysis is performed applying at the base area of the rock mass model the seismic input of the earthquake that occurred on 04/06/2011. The results shown in Tab. 5.6 confirm the accordance, in terms of effective acceleration and Spectrum Intensity of Housner, of the crowning level record and the simulated signal with a damping ratio of 0.02.

Tab.5.4. Modal analysis results of the FEM model of the dam structure.

Dam structure finite element model				
Frequencies		**Damping parameters**		
mode	**f (1/s)**	**ζ**	**α (1/s)**	**β (s)**
1	3.31	0.005	0.0205	0.0012
2	3.32	0.010	0.0410	0.0023
3	4.47	0.020	0.0820	0.0046
4	5.38			
5	6.59			
6	7.41			
7	7.88			

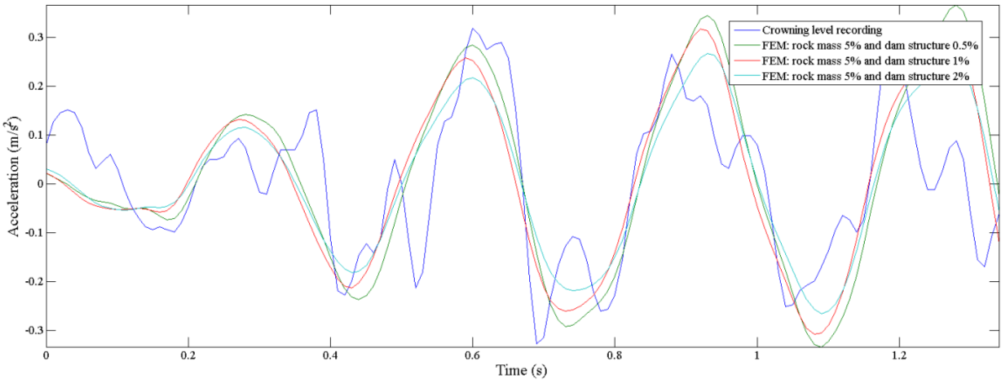

Fig. 5.10. Accelerograms extracts of the crowning level record (26/01/2003), acquired at position C, and of the simulated signals for different damping ratios (0.5%, 1%, 2%).

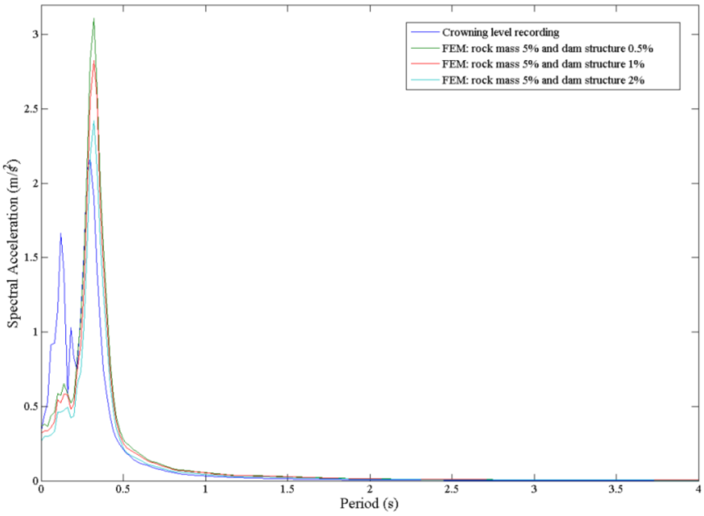

Fig. 5.11. Spectral response accelerations of the crowning level record (26/01/2003), position C, and of the simulated signals for different damping ratios (0.5%, 1%, 2%).

Tab. 5.5. Effective accelerations a_{RMS} and Spectrum Intensity of Housner I_H of the crowning level record (26/01/2003) and of the simulated signals for different damping ratios (0.5%, 1%, 2%).

Complete finite element model				
	Record	**0.005**	**0.010**	**0.020**
a_{RMS}(m/s^2)	0.1509	0.1882	0.1705	0.1444
I_H (m)	0.0530	0.0692	0.0623	0.0518

Tab. 5.6. Effective accelerations a_{RMS} and Spectrum Intensity of Housner I_H of the crowning level record (04/06/2011) and of the simulated signal for 0.020 of damping ratios.

Complete finite element model		
	Record	**0.020**
a_{RMS}(m/s^2)	0.0741	0.0680
I_H (m)	0.0424	0.0350

5.3.3 Results

Damping parameters evaluation is a fundamental aspect of finite element modelling and values are very often given in general literature indications. Large structures such as dams need a careful characterization of this aspect. The present study aims to provide an operative procedure to identify the damping ratio firstly of the rock mass FEM model and secondly of the structure FEM model. Modal analyses of the two systems provide the natural frequencies required for the evaluation of α and β damping parameters. By means of linear elastic dynamic analyses, the best accordance between real and simulated signals for the rock mass is given by a 0.05 of the critical damping ratio. Looking at the range provided by literature, the damping level is low. It should be taken into account that the free-field motion is recorded at 40m depth, in position A, Fig. 5.2, and the same signal is employed as input of the FEM model at 150m depth, in position 1, Fig. 5.7. Therefore, the signal in the FEM model, in order to reach ground level, has to travel a longer distance than it does in reality. Because of this, the estimated damping ratio for the rock mass can appear low in relation to the usual real values. However the rock mass FEM model is rightly calibrated, the simulated signal at ground level is in accordance with the recorded one in terms of the effective value of acceleration and Spectrum Intensity of Housner. Similarly, employing the calibrated damping ratio for the rock mass, the whole FEM model of the dam system is in accordance with the real records, adopting, as a material property of the concrete structure, a damping ratio of 0.02. The complete FEM model of the Ridracoli dam, previously calibrated, allows us to reproduce the real behaviour of the structure under seismic input motion. The simulated signals are in accordance in terms of maximum accelerations time-history and frequencies with the real records.

5.4 Elasto-Plastic damage time-history analysis

The solid element joint model, including the vertical joints as slices with their own thickness and material, allows us to investigate the damage evolution throughout such discontinuities. Indeed, the CDP – Concrete Damage Plasticity – model is adopted for the concrete of the vertical joints while the other materials have linear elastic constitutive behaviour. The constitutive models are described in §3.6.1 and the assigned mechanical properties are reported in §4.3.3. The compressive and tensile behaviours of the hydraulic mortar of the joints are included in tabular form, as stress-strain and stress-displacement relationships respectively. Similarly, the related damage evolutions are expressed as damage C parameter-strain and damage T parameter-displacement respectively. Indeed, the adoption of a stress-displacement relationship rather than a stress-strain relationship reduces the mesh sensitivity of the results in tensile behaviour [6]. Until the ultimate tensile/compressive strength is reached, no damage occurs; indeed, it is defined, for the descending branch of the relationships, as the unit minus the ratio between the generic stress and the ultimate peak strength. In order to analyse damage evolution throughout the joint elements, a strong seismic motion has to be applied. Therefore, given that the events that occurred on the Ridracoli site were not sufficiently intense, a suitable seismic event has to be employed. As described in §4.4, the Italian and European regulations allow, in the assessment of seismic vulnerability by means of nonlinear analysis, the use of suitable real seismic time-history records, as long as their spectra fits with the design target spectrum of the site. Adopting for the Ridracoli site a collapse limit state (SLC) target spectrum, the selection, performed by means of REXELite [7,8], extracts seven groups of seismic events that occurred in central Italy, Tab. 4.5 (Chapt. 4). Between them, the Accumoli (RI) event, which occurred on 30/10/2016, with a scale factor closest to the unit, is adopted into the analysis. The three components are reported in Appendix 4.3, two horizontal along North-South and East-West directions, and the vertical one along up-down direction. The accelerations time-history is uniformly applied at the base surface of the FEM model: the N-S component along the upstream-downstream direction, the E-W component along the left-right direction and the U-D component along the vertical direction. The analysis is performed taking into account three significant water levels: the normal reservoir level of 557.3m a.s.l., the minimum operating level of 523m a.s.l. and the empty reservoir condition. The time step of the analysis is defined in relation to the time sampling: the inverse of the instrumental frequency is assumed as maximum values of the time period ($\Delta t=0.005s$). Instead, the minimum value is fixed short enough to be compatible with the computational time. The compressive C and tensile T damage parameters, at the end of the maximum acceleration peaks, for the joints of the FEM model with empty reservoir are reported in Figs. 5.12 and 5.13 respectively. Moreover, the results of all three-water level analyses are shown in Appendices 5.1, 5.2, 5.3, 5.4, 5.5 and 5.6. The upper part, close to the dam crowning, of the joint 1, located close to the key section of the dam, is showed in Fig 5.14: the tensile damage parameter is reported, at the end of the maximum acceleration peaks of the seismic event, for each of the aforementioned water level.

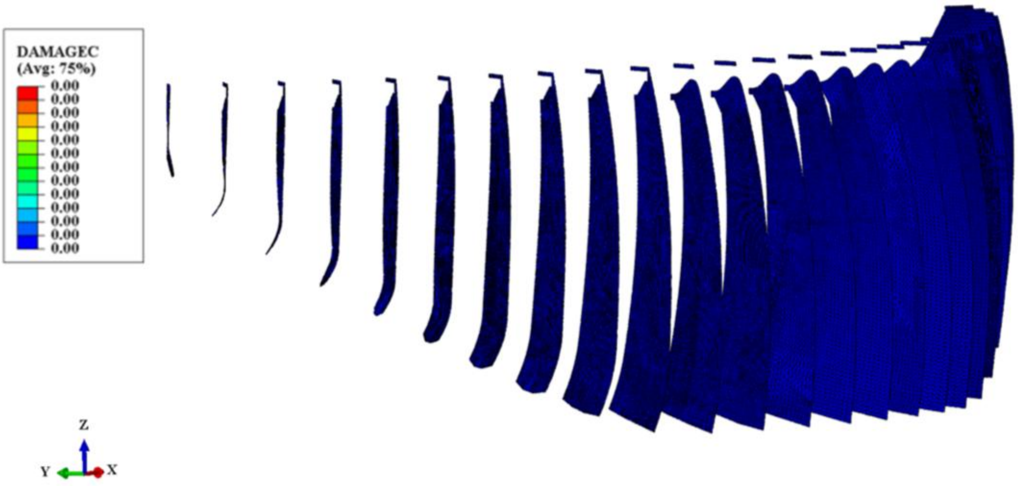

Fig. 5.12. Compressive (C) damage parameter distribution of the vertical joints at the end of the maximum acceleration peaks of the Accumuli (RI) seismic event and with empty reservoir condition. No compressive damage occurs.

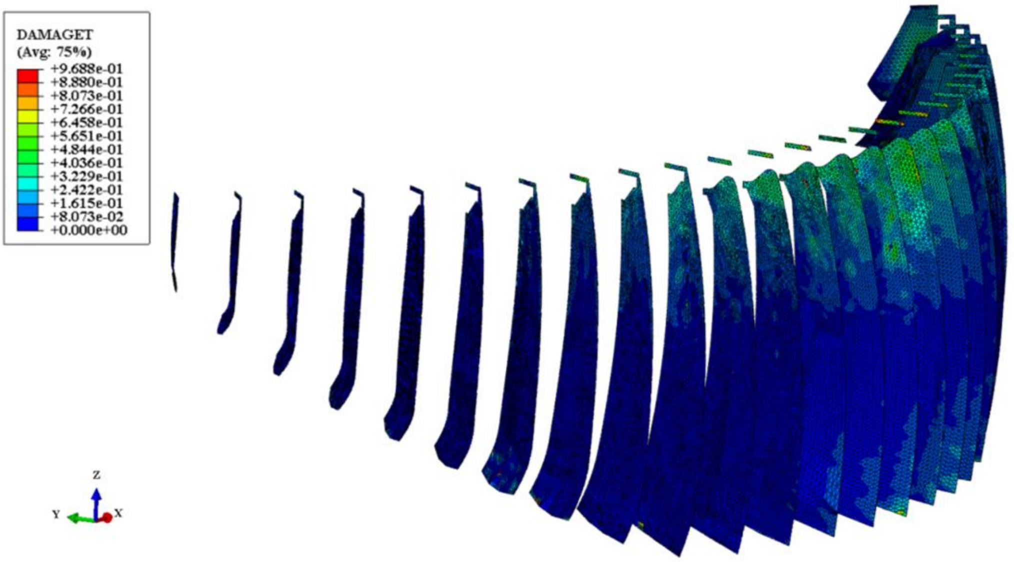

Fig. 5.13. Tensile (T) damage parameter distribution of the vertical joints at the end of the maximum acceleration peaks of the Accumoli (RI) seismic event and with empty reservoir condition. The tensile damage appears concentrated in the central joint and close to the dam crowing.

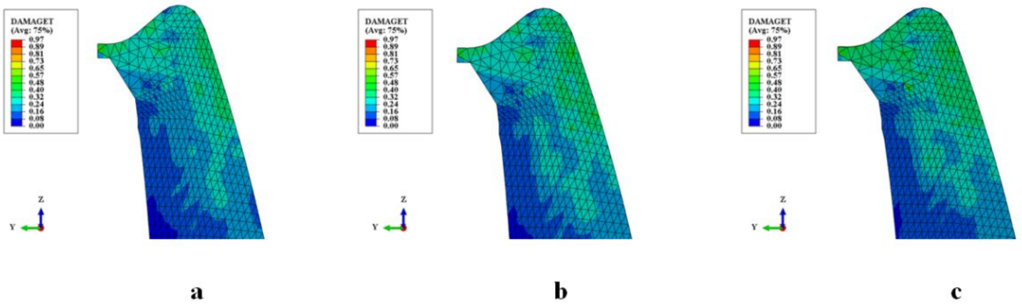

Fig. 5.14. The upper part of the joint 1, located close to the key section. The tensile damage, under Accumoli (RI) seismic event, progressively increases with the decrease of the water level, passing from a) normal reservoir level (557.3m a.s.l.), to b) minimum operating level (523m a.s.l.), to c) empty reservoir condition.

5.4.1 Results

The value of the compression C damage parameter appears null in all three analyses, App. 5.1, 5.2, 5.3. This means that the ultimate compressive strength is never reached and compressive damage does not occur in joint elements. As expected, the tensile T damage is the most significant parameter for describing the behaviour of the hydraulic mortar. As the water level increases in the reservoir, resonant frequencies generally decrease due to the additional mass added to the dam–reservoir system [3]. Consequently, the effect of the accelerations time-history applied at the base of the model is less damaging on the structure. Passing from the empty reservoir condition, to the minimum operating level (523m a.s.l.) and then to the normal reservoir level (557.3m a.s.l.), the propagation of the tensile damage decreases throughout the joint elements, Fig. 5.12. The tensile damage appears generally located in the central joints and mostly close to the dam crest, Fig. 5.13 and App. 5.4, 5.5, 5.6. Moreover, all three analyses show that the damage T parameter reaches the unit value (red colour), which physically means the complete loss of material stiffness, just in really reduced areas such as the end part of the ramp of the spillway; it is probably due to a local tensile concentration. In general the decrease of the stiffness of the hydraulic mortar assumes maximum value of 50% close to the cortical area of the joint, close to the spillway. In every case, such stiffness reduction does not involve fracturing of the material. Therefore, the dam can withstand the heavier SLC – Collapse Limit State – which corresponds the applied seismic input, shaking without release of water from the reservoir, as also required by the Italian regulation DM 26/06/2014 for such a level of seismic event.

5.5 Chapter bibliography

[1] Berrabah A. T., Belharizi M., Laulusa A. and Bekkouche A., "Three-Dimensional Modal Analysis of Brezina Concrete Arch Dam, Algeria", *Earth Science Research*, vol. 1, no. 2, June 2012.

[2] Chopra A. K., "Earthquake analysis of arch dams: factors to be considered", 14th World Conference on Earthquake Engineering, October 12-17, 2008, Beijing, China.

[3] Proulx J., Darbre G. R. and Kamileris N., "Analytical and experimental investigation of damping in arch dams based on recoreded earthquakes", 13th World Conference on Earthquake Engineering Vancouver, Canada August 1-6, 2004.

[4] Goldgruber G., Shahriari M., Zenz S., "Influence of damping and different interaction modelling on a high arch dam", Vienna Congress on Recent Advances in Earthquake Engineering and Structural Dynamics 2013 (VEESD 2013), 2013.

[5] Fenves G. and Chopra A. K., "Earthquke analysis and response of concrete gravity dams", Report, 1984.

[6] Hillerborg P.-E., Modéer A. and Petersson M., "Analysis of crack formation and crack growth in concrete by means of fracture mechanics and finite elements", *Cement and Concrete Research*, vol. 6, no. 6, pp. 773-781, Nov. 1976.

[7] Iervolino I., Galasso C. and Cosenza E., "REXEL: computer aided record selection for code-based seismic structural analysis", *Bulletin of Earthquake Engineering*, vol. 8, no. 2, pp. 339-362, Apr. 2010.

[8] Iervolino I., Galasso C., Paolucci R. and Pacor F., "Engineering ground motion record selection in the ITalian ACcelerometric Archive", *Bull Earthquake Eng*, vol. 9, pp. 1761-1778, 2011.

6. Conclusions and suggestions for further studies

Safety and proactive vision are key aspects in the management of large structures such as dams. Nowadays, FEM simulations are widely recognized as essential tools in the analysis of the behaviour of dam systems. A detailed representation of the dam structure allows for a better understanding of the local response of important structural elements. From this perspective, the application of UAVs – Unmanned Aerial Vehicles – to surveys of infrastructures with a complex geometrical shape, such as dams, is the basis, when adequately supported by topographic instruments, for the development of an accurate metric reconstruction. The present study provides an operative procedure that covers all the process from the UAV surveying, to the dense point cloud validation, to the three-dimensional FEM modelling of masonry dams applied to a concrete arch gravity dam located in central Italy: the Ridracoli dam.

6.1 Summary

The drone technique makes it possible, with more than 3000 frames, to cover the entire dam system; the correct geo-referencing and matching of the dense point cloud is ensured by the placement and acquisition of the coordinates, also using traditional topographic tools (i.e. Total Station, Laser Scanner and GPS Station), of 218 points, between markers and natural points. The validation by points evaluates an average gap, between the reference markers acquired by Total Station and the same generated by the UAV dense point cloud, of ±1.0cm. The average distance between lines, at the same level, extracted by the Laser Scanner model and the UAV dense point cloud is ±2.0cm. Finally, the validation by surfaces evaluates a distance between the mesh built on the laser scanner scans and the UAV dense point cloud of ±0.9cm on average. Moreover, the accuracy of the UAV product is ensured by its comparison with the technical drawings of the dam in terms of construction points (i.e. curvature centres).

The high accuracy of the UAV technique allows for the reproduction of the geometry of the structure, of the surrounding area and of ancillary works in great detail (i.e. stilling basin, weight blocks on the sides). A prompter extension of the rock mass is included in the representation to reproduce the boundary deformability conditions; the fluid-structure interaction is taken into account by means of acoustic elements reproducing the hydrodynamic effect of the retained water during dynamic analyses. By means of the high density point cloud and the design geometry, the vertical and *pulvino* foundation construction joints are included into the dam modelling. In order to analyze the influence of vertical construction joints modelling on the dynamic properties of the structure, three FEM models of the dam body are built. Monolithic, surface-to-surface joint and solid element joint representations are tested in terms of natural frequencies and mode shapes with experimental results provided by a vibrodyne test and environmental vibrations of real seismic events. All three representations provide results close to the experimental ones, higher modes show a larger gap probably due to the fluid vibration effect, elevated and not distinguishable through the vibrodyne excitation. The natural frequencies extracted by the PSD – Power Spectral Density – function mostly approach the values provided by the solid element joint FEM model. The stiffness of the FEM models decreases passing from the monolithic to the surface-to-surface joint to the solid element joint representations. The three sets of natural frequencies differ slightly: 0.75% between the monolithic m. and the surface-to-surface joint m., 0.82% between the monolithic m. and the solid element joint m., 0.31% between the surface-to-surface joint m. and the solid element joint m.. Moreover, the mode shapes provided by the three FEM models are equal, fitting also with the ones provided by the vibrodyne test, thus the joint representation does not influence the global dynamic behaviour of the structure.

Adopting the solid elements joint representation, a first static test under *cause* quantities, hydrostatic load and constant temperature, verifies the overall functionality of the FEM model in terms of crest displacements. Furthermore, a procedure is proposed for evaluating the Rayleigh damping parameters for the rock mass and for the concrete of the structure. The best accordance, in terms of Effective Acceleration a_{RMS} and Spectrum Intensity of Housner I_H, is reached for damping ratios of 0.05 and 0.02 for the rock mass and the concrete of the structure respectively.

By means of the selection of suitable seismic events, compatible with the target spectrum of the Ridracoli site for SLC – Collapse Limit State – seismic probability, nonlinear damage dynamic time-history analyses are performed. Three water levels are taken into account to simulate the empty reservoir, the minimum operating level (523m a.s.l.) and the normal reservoir level (557.3m a.s.l.). The CDP – Concrete Plasticity Damage – model is assigned only to the joint material and the Accumoli (RI) seismic event, which occurred on 30/10/2016, is employed in the simulations. In all three analyses, compression damage does not occur. Instead, the tensile damage is generally located in the central joints, close to the crowing of the dam, and its propagation increases with the decrease of the water level. Indeed, the additional mass added to the dam–reservoir system dampens the effect of the ground motion on the structure. In all three analyses, the maximum value of the damage T parameter, the unit value, which physically means a complete loss of stiffness, appears located in really reduced areas such as the end part of the ramp of the spillway that is probably due to a local tensile concentration. In general the reduction of the stiffness of the hydraulic mortar does not exceed 50% and, in every case, such stiffness reduction does not involve fracturing of the material. This means that, also under an SLC seismic event, the more burdensome limit state, the retaining water capacity of the joint elements is ensured, in conformity with the Italian regulation DM 26/06/2014 concerning the planning and construction of retaining structures.

6.2 Conclusions

The uses and potential deployment of the UAV product are various. Some areas of the Ridracoli dam and similar structures, due to their reduced accessibility, would require considerable safety inspections work (involving climbers) and the simultaneous sharing of information among maintenance and management technicians would not always be possible. Therefore, the possibility to have a photographic record of every detail of the structure allows for shared participation and establishes a base level by which to monitor the evolution of the conservation status of the structure so that would be possible to pass from a “run to failure” maintenance management to a predictive and proactive one. The speedy flight and its repeatability give the possibility to forecast rapid ageing in order to prevent a partial loss of safety with sustainable costs.

However, a terrestrial topographic survey by traditional tools such as Total Station, GPS Station and Laser Scanner is required to geo-reference and validate the UAV dense point cloud. Moreover, to reach an high accuracy of the survey, the placement of the markers and the choice of the natural points have to be accurate. They have to be well spaced and uniformly placed on the object of the survey to avoid local distortions and to reduce the global error of the dense point clouds especially close to the boundaries.

In the present study, the main aim of the UAV survey is to provide a validated dense point cloud that can be useful as basis for the development of a three-dimensional model of the dam system for FEM analyses. Moreover, large structure models such as those of dams require a specific study of the Rayleigh damping parameters of the rock mass and of the concrete, since the ranges proposed by literature are rather large. Furthermore, the detailed representation allows for the investigation of the influence of the vertical joint modeling procedures on the dynamic properties of the structure. If the goal is the analysis of the general behaviour of the structure under seismic events, a simplified model such as the monolithic one can be employed without devoting important pre-processing work-time and computational costs to sophisticated models, such as that with solid elements as vertical joints. However, the vertical construction joints are planes of weakness of the structure, being in reality, injected with hydraulic mortar with mechanical properties that are lower than those of the concrete of the blocks. Therefore, they have to be included in FEM model for verifying, under strong seismic events, that the tensile and compressive strengths are not exceeded or, when they are, in which way the damage is distributed throughout these elements. Moreover, the evaluated percentile gaps between the FEM models of the dam body can be meaningful if the intention is to evaluate the state of conservation of the materials: the evolution of the natural frequencies is fundamental in detecting any small change in the behaviour of the structure and the closer the simulated natural frequencies are to the real ones the more an eventual parametric study is performing.

The inclusion of vertical construction joints into finite element models of dams allows us to verify the behaviour of such real discontinuities under MCE – Maximum Credible Earthquake – events and therefore to verify the seismic vulnerability assessment of the whole structure.

In the light of the above considerations, the main results of the present study can be summarized as follows:

- a traditional topographic survey is still necessary to geo-reference and validate the UAV dense point cloud;

- the UAV technique may be employed for the solid three-dimensional reconstruction of large dams reproducing important details such as double-curvature vertical joints, *pulvino* foundation joints, spillways, weight blocks, etc.;

- in literature, a wide range of Rayleigh damping parameters are proposed, however, to achieve a FEM model close to the reality, a specific study on the calibration of Rayleigh damping parameters, based on natural frequencies of the rock mass and the structure representations and on real seismic records of the site, is required;

- the joint modeling procedure does not influence the global dynamic behaviour of the structure, the mode shapes do not change, and simplified model, such as the monolithic one, can be employed for the study of the general behaviour of the structure under seismic event;

- more sophisticated models, such as the solid element joint representation, have to be employed if the goal is the evaluation of the state of conservation of the structure, indeed simulated natural frequencies have to be as close as possible to the real ones to detect any small change in the behaviour of the structure;

- the inclusion of construction joints in FEM model like solid elements allows for the verification also of these discontinuities in case of MCE – Maximum Credible Earthquake –, ensuring the overall seismic vulnerability assessment of the structure.

Concluding, the present work and the achieved results allow us to say that the proposed FEM modelling procedure of masonry dams, including structure-foundation and fluid-structure interactions and the construction joints in the dam body, can be widely employed for a predictive and proactive management of such type of large structures in order to guarantee the safety and the reduction of the related costs.

6.3 Future Developments

Since the multidisciplinary nature of a dam system, future developments concern different aspects of the present study.

The natural frequencies of the dam structure are extracted from acceleration records of the dam crowing due to significant occurred seismic events, as well as from the vibrodyne test; such frequencies and mostly their variation over time can be detected also from ambient vibrations, not acquired by the dynamic monitoring system, related to water level variations, temperature variations or micro-seismic events. This real-time diagnostic could be performed by means of the installation of a vibration-based SHM – Structural Health Monitoring – system on the dam body of the inspected dam. This technique, already tested on cultural heritage constructions, has a fully nondestructive character. Indeed, the analysis of ambient vibrations, provided by high-sensitivity accelerometers placed on the structure, can detect anomalies in the structural behaviour. The sensors should be placed along the longitudinal direction of the structure, i.e. along the inspection galleries and/or along the dam crowing, at different elevations. In this way, as well as the natural frequencies also the mode shapes are identified. The rapid damage detection can be performed analysing the changes in frequencies that clearly appear from the analysis of monitoring data and the evolution of the state of conservation of the materials can be investigated. Moreover, such new values of natural frequencies can be employed for the real-time calibration of the FEM model and the behaviour of the structure with the current mechanical properties can be simulated.

The Italian regulation requires the seismic verification not only of the dam structure but also of the ancillary works such as the dam crowing road, the depletion sluice gate and, in general, of every elements that can compromise the safety during a seismic event. Due to the high detail of the current FEM model, some of the aforementioned ancillary works are already included into the representation (e.g. the dam crowing road, the stilling basin, etc.), others can be added to the model (e.g. the depletion sluice gate). In this way, analyzing the stress concentrations and the potential damage, the seismic verification also of these elements can be performed.

A certain future development of the analysis procedures also for dams is represented by Isogeometric Analysis (IGA). As explained by Hughes at al., 2005, this is an innovative numerical approach that employs as approximation functions those used in computer graphics commonly known as NURBS – Non Uniform Rational B-Splines –. NURBS match the exact CAD geometry, allowing the direct communication between CAD and analysis environments. In this way, problems related to geometric imperfections are eliminated and the mesh refinement is simplified once the initial mesh is constructed. Therefore, compared to FEM procedures, IGA formulation could provide more accurate results and it could reduce computational costs.

Appendix

4.1 – Acceleration time-history records of positions A, D, C (Fig. 5.2) along upstream-downstream direction: 26/01/2003.

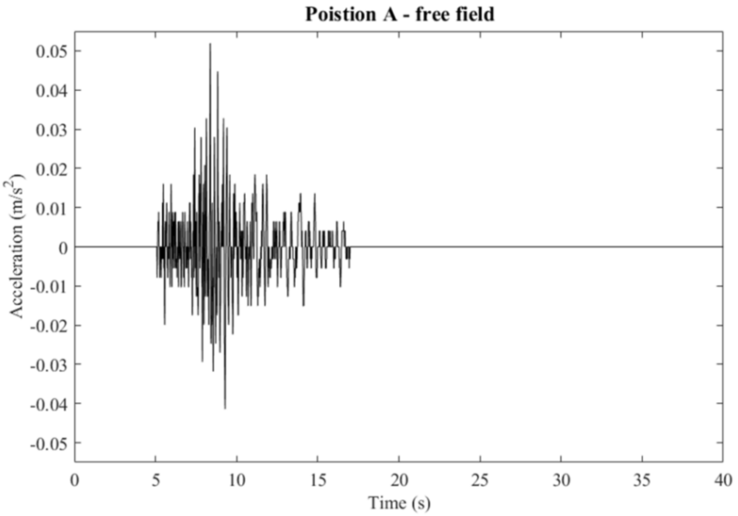

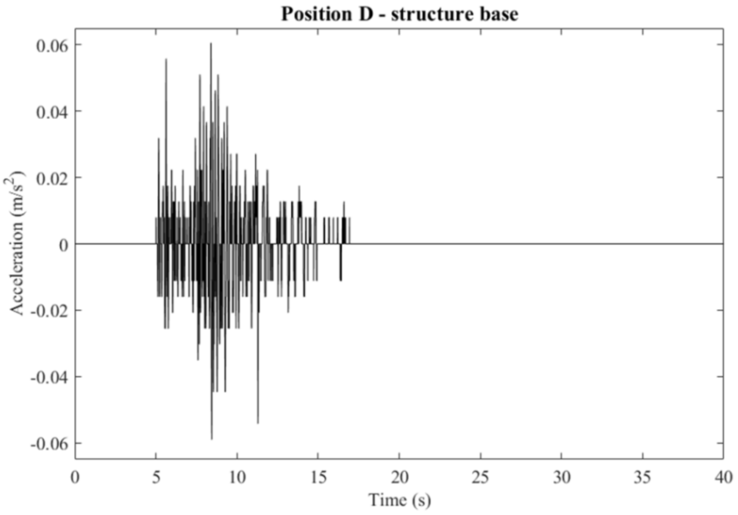

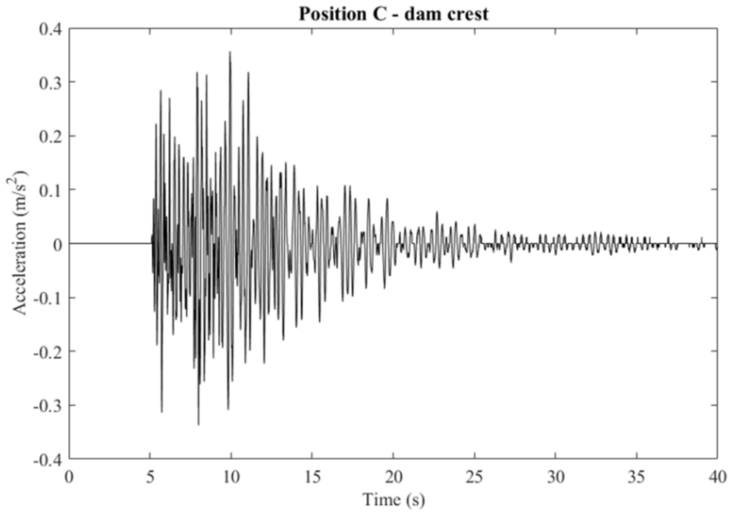

4.2 – Acceleration time-history records of positions A, D, C (Fig. 5.2) along upstream-downstream direction: 04/06/2011.

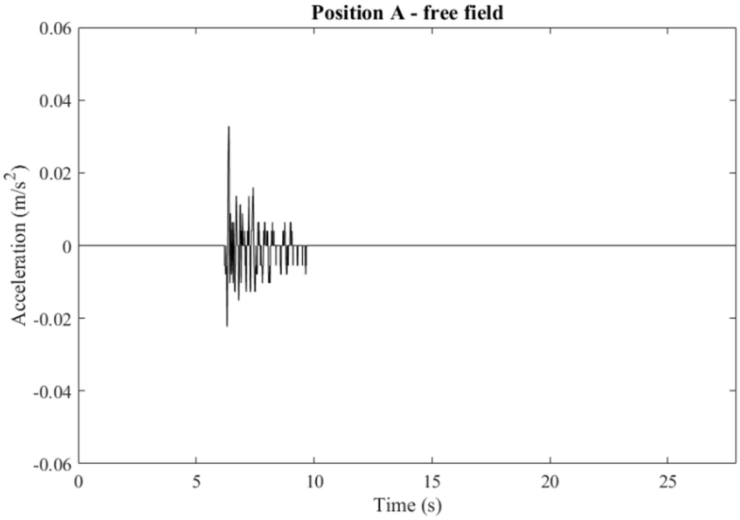

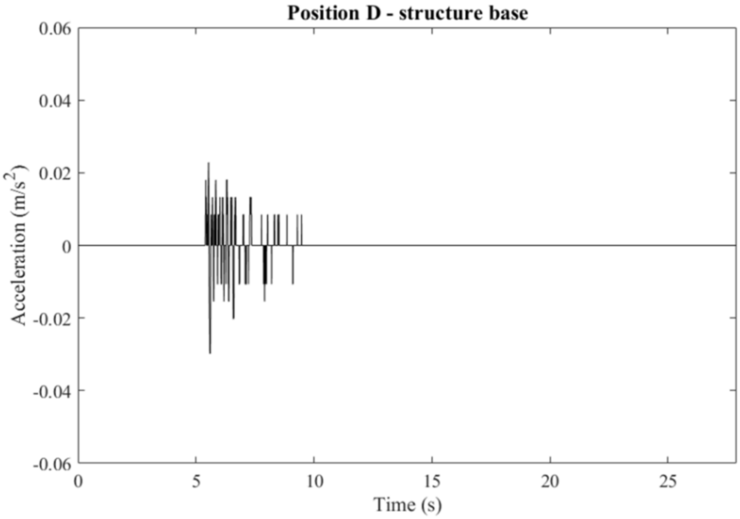

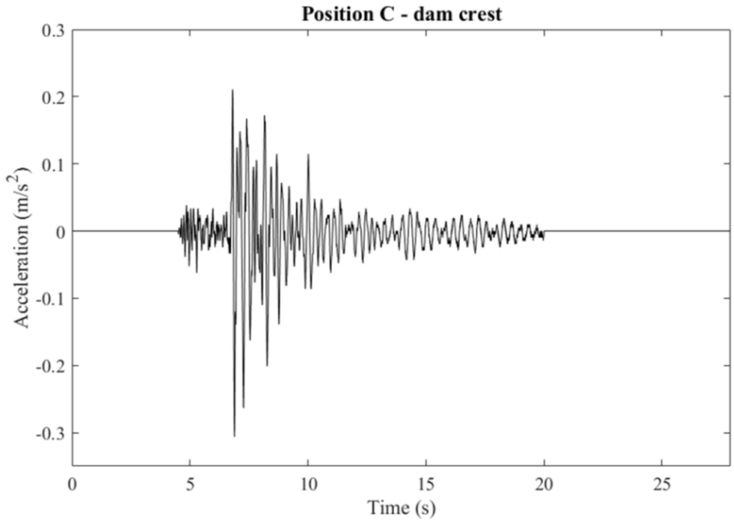

4.3 – Acceleration time-history records of Accumuli (RI), Italy, 30/10/2016, M_L=6.1.

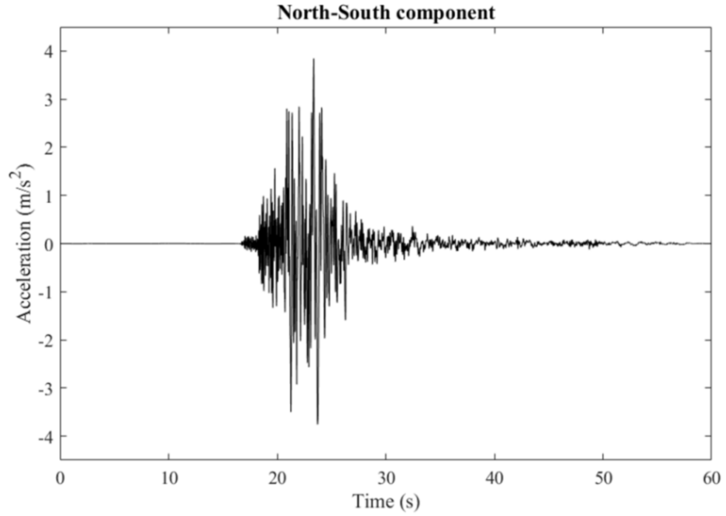

North-South component

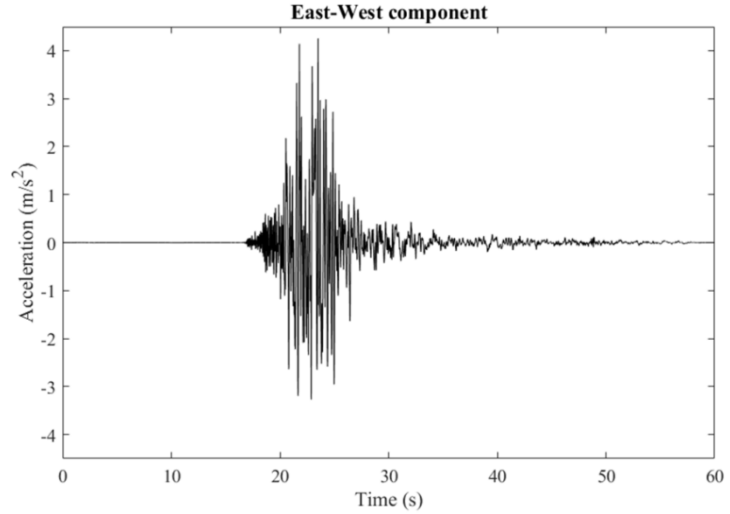

East-West component

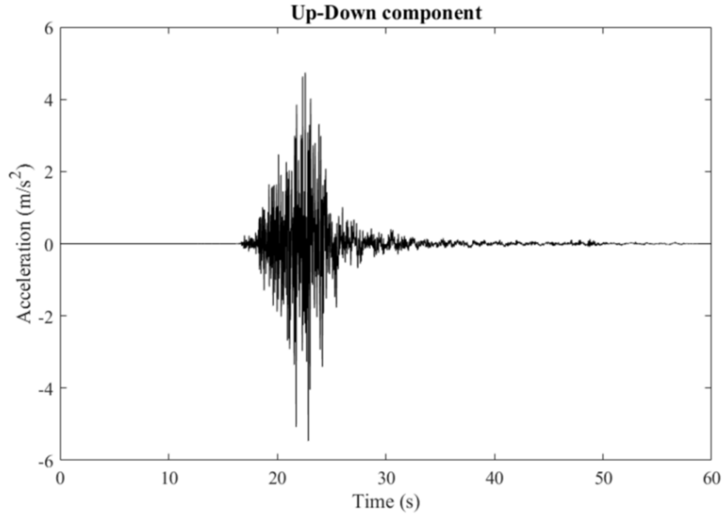

Up-Down component

5.1 – Compressive (C) damage parameter distribution of the vertical joints at the end of the maximum acceleration peaks of the Accumuli (RI) seismic event and with empty reservoir condition. a) upstream face; b) downstream face.

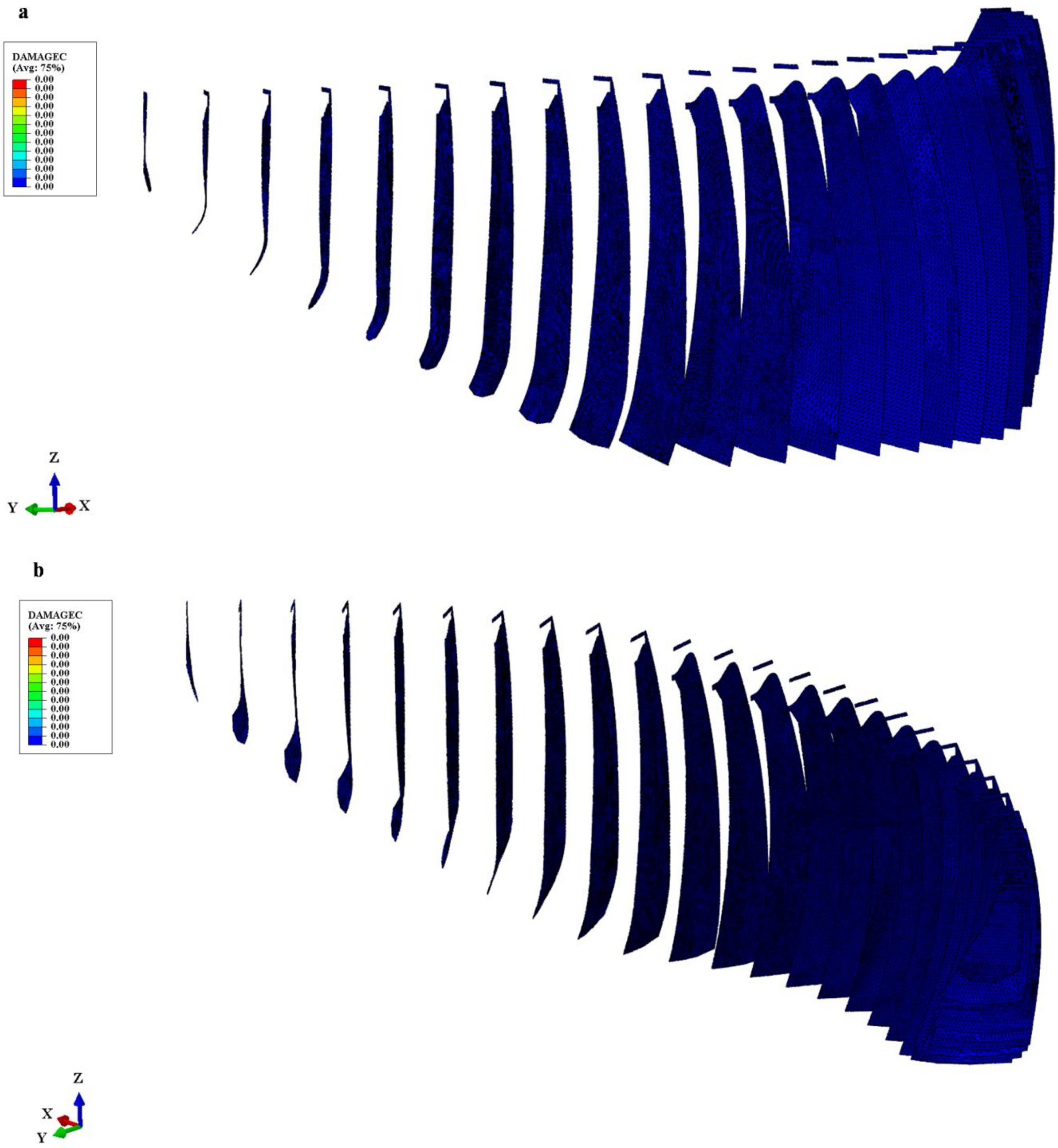

5.2 – Compressive (C) damage parameter distribution of the vertical joints at the end of the maximum acceleration peaks of the Accumuli (RI) seismic event and with minimum operating level (523m a.s.l.). a) upstream face; b) downstream face.

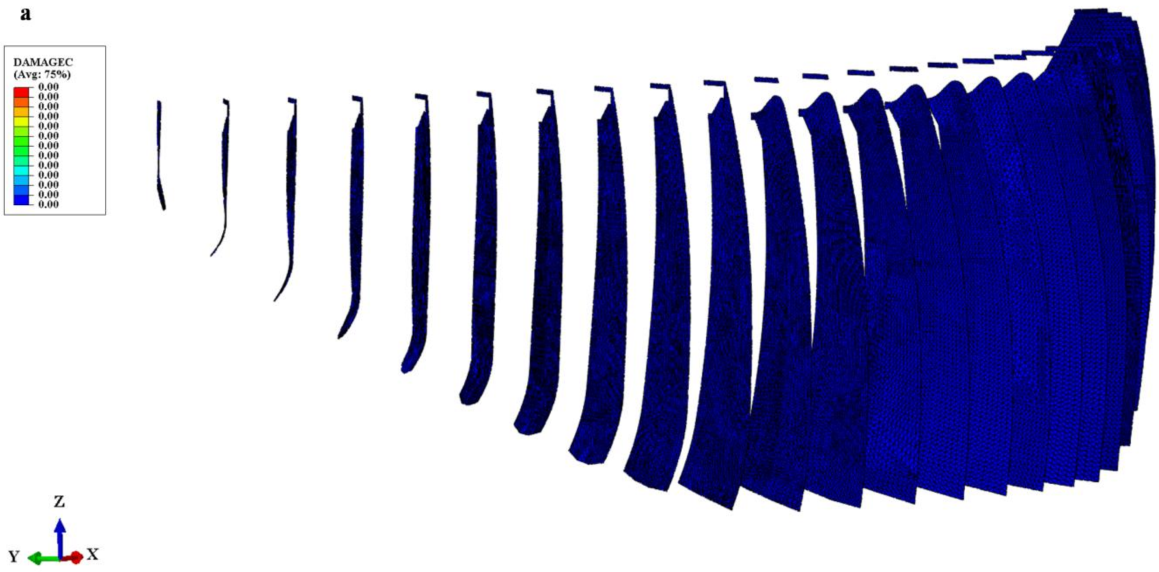

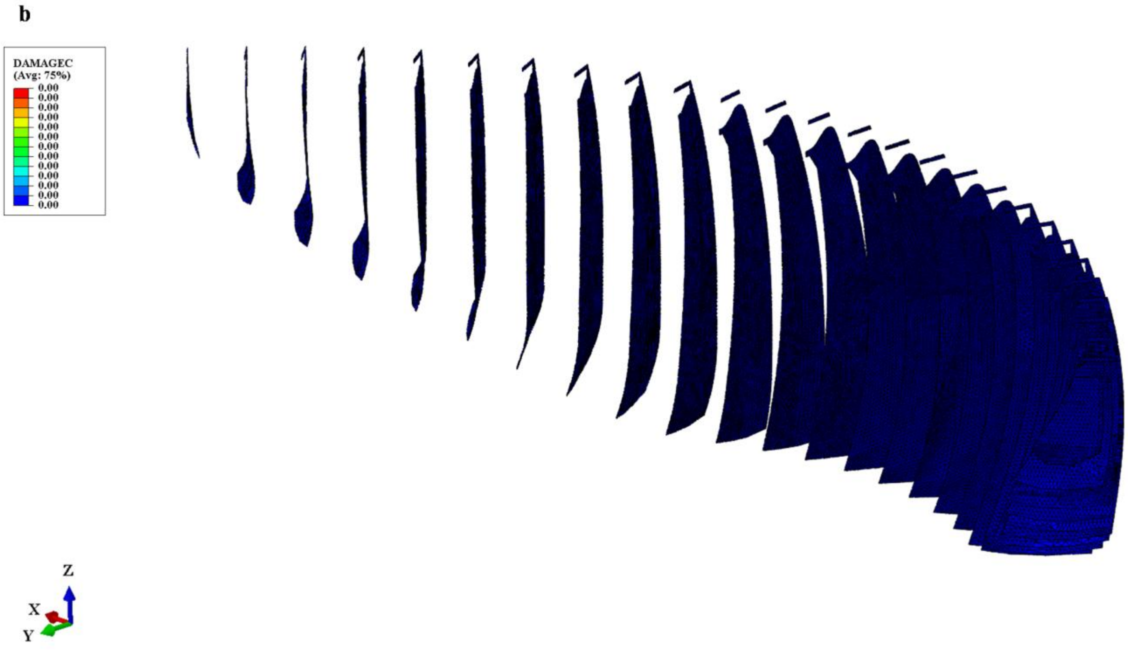

5.3 – Upstream face, compressive (C) damage parameter distribution of the vertical joints at the end of the maximum acceleration peaks of the Accumuli (RI) seismic event and with normal reservoir level (557.3m a.s.l.). a) upstream face; b) downstream face.

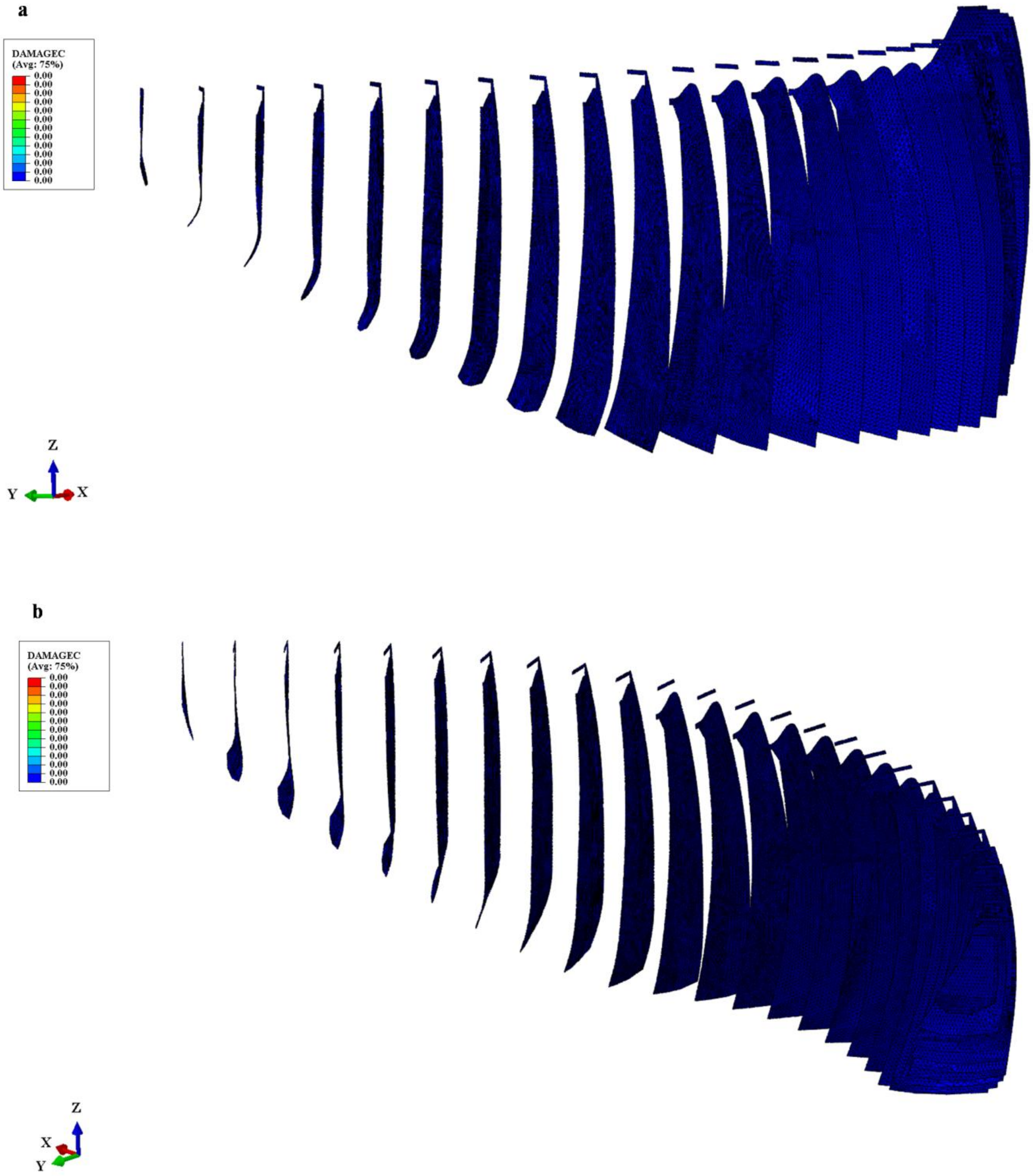

5.4 – Tensile (T) damage parameter distribution of the vertical joints at the end of the maximum acceleration peaks of the Accumuli (RI) seismic event and with empty reservoir condition. a) upstream face; b) downstream face.

a

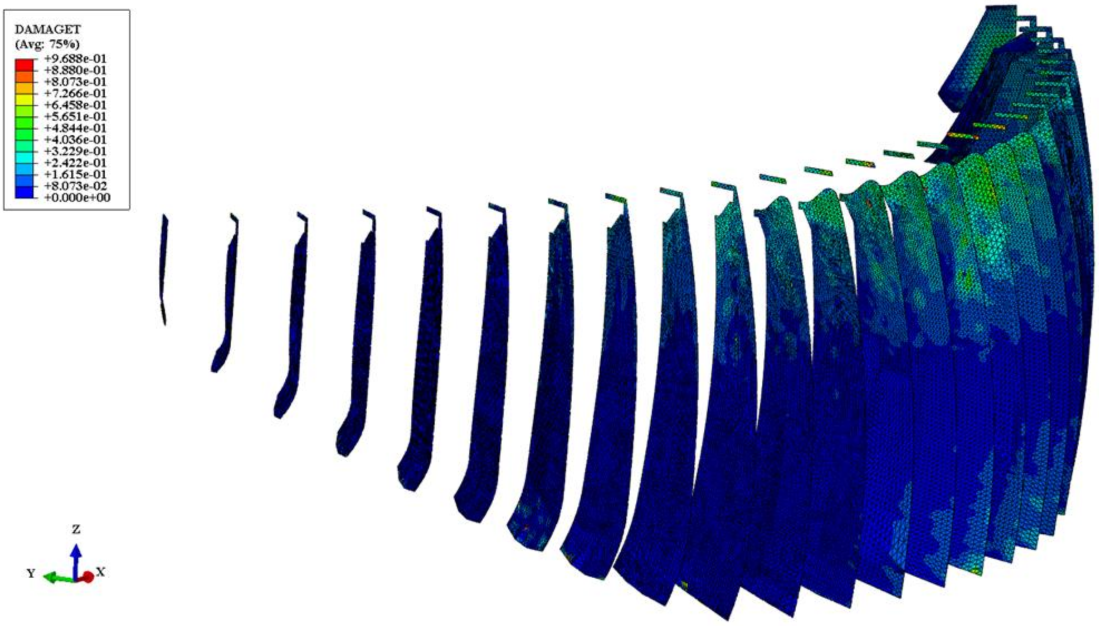

b

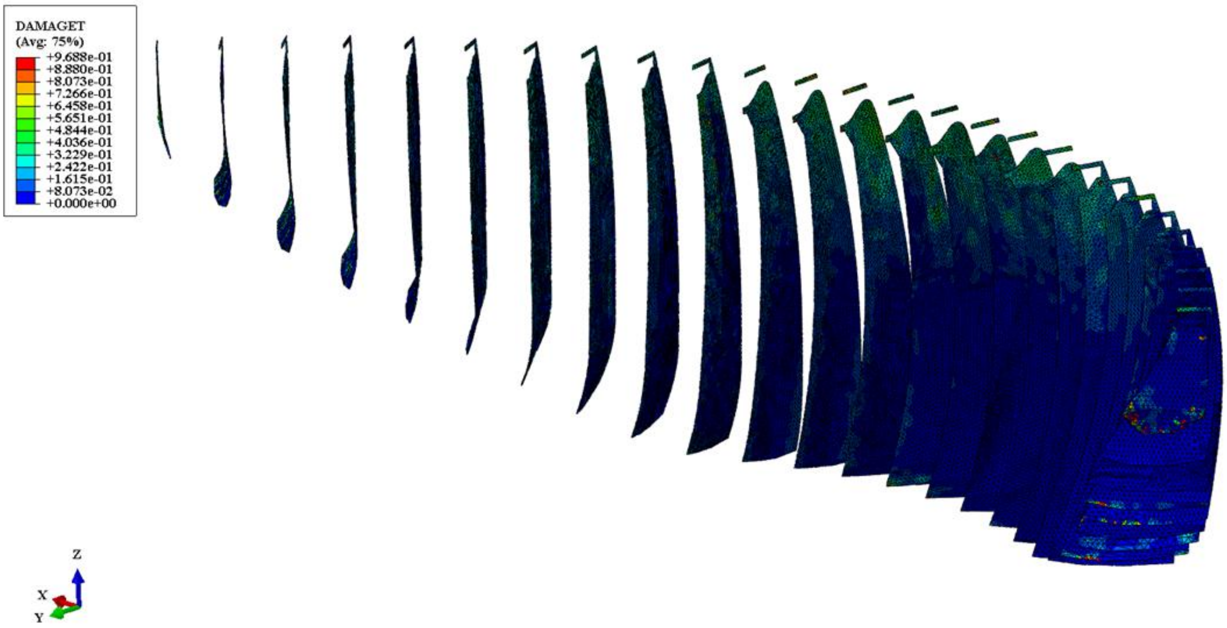

5.5 – Tensile (T) damage parameter distribution of the vertical joints at the end of the maximum acceleration peaks of the Accumuli (RI) seismic event and with minimum operating level (523m a.s.l.). a) upstream face; b) downstream face.

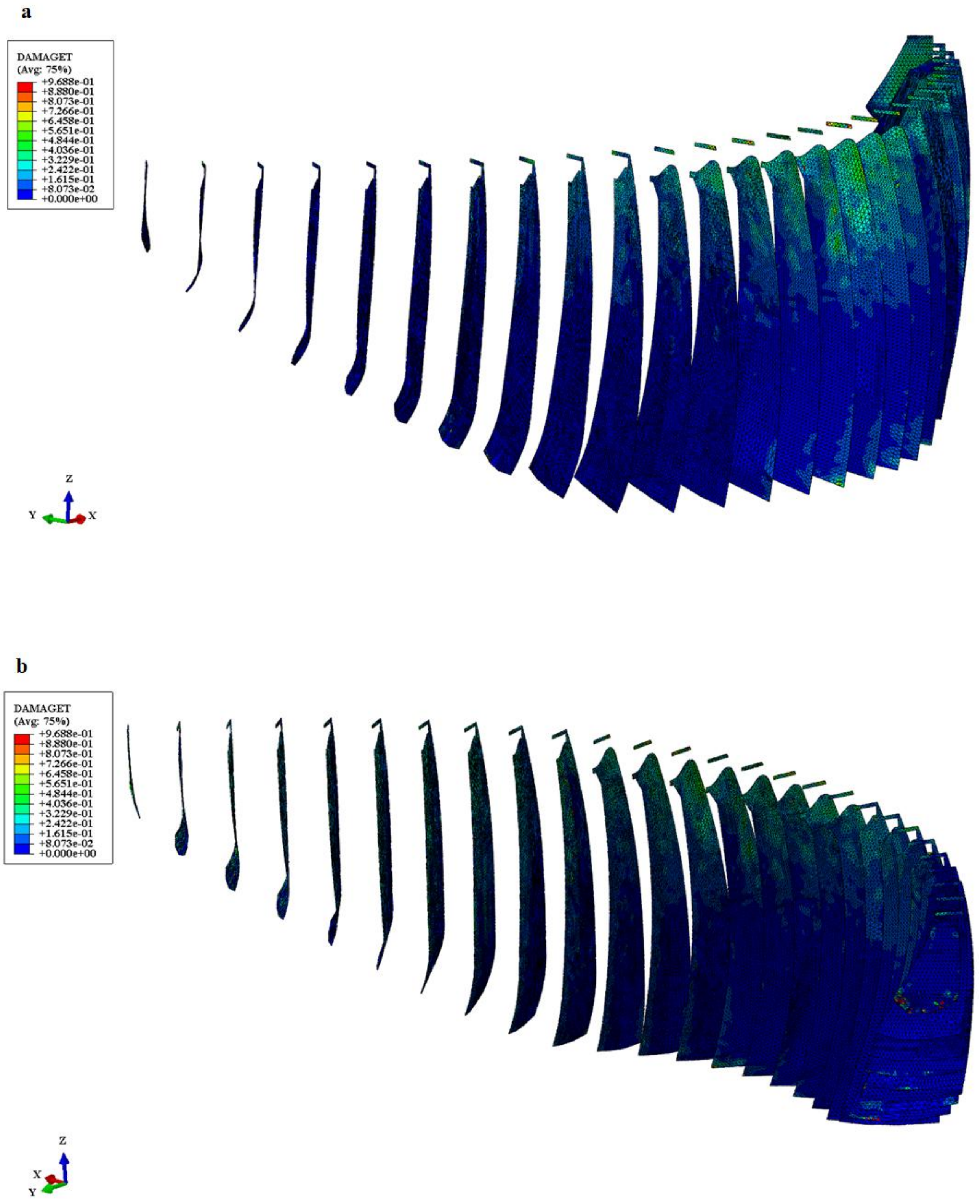

5.6 – Tensile (T) damage parameter distribution of the vertical joints at the end of the maximum acceleration peaks of the Accumuli (RI) seismic event and with normal reservoir level (557.3m a.s.l.). a) upstream face; b) downstream face.